# Laser Frequency Stabilization Using a Slow Light Cavity

Gustavsson, David

2024

Laser Frequency Stabilization Using a Slow Light Cavity

# Laser Frequency Stabilization Using a Slow Light Cavity

by David Gustavsson


LUND
UNIVERSITY

Thesis for the degree of Doctor of Philosophy
Thesis advisors: Dr. Lars Rippe, Dr. Adam Kinos, Prof. Stefan Kröll
Faculty opponent: Dr. Mikael Afzelius

To be presented, with the permission of the Faculty of Engineering of Lund University, for public criticism in the Rydberg lecture hall at the Department of Physics on Friday the 27th of September, 2024, at 1:15pm.

| Organization | Document name |
|---|---|
| **LUND UNIVERSITY**<br>Department of Physics<br>Box 118<br>SE–221 00 LUND<br>Sweden | **DOCTORAL DISSERTATION**<br>Date of disputation<br>2024-09-27<br>Sponsoring organization |
| Author(s)<br>David Gustavsson | |


Title and subtitle

Laser Frequency Stabilization Using a Slow Light Cavity


Abstract

Laser frequency stabilization is a necessary component in many modern technologies and physics experiments, providing spectral resolution for spectroscopic investigations, accurate optical clocks for timekeeping and phase stability for interferometry. The limiting factor to the frequency stability of state-of-the-art laser stabilization is frequency uncertainty as a result from variations in the length of the cavity used as a reference, due to Brownian motion of the atoms forming the mirrors. One way to mitigate this issue is to extend the cavity, thereby reducing the relative length uncertainty. This thesis describes a laser frequency reference which was built out of a plane mirror cavity surrounding a crystal of yttrium orthosilicate doped with rare-earth ions. These ions have narrow optical transitions and long lived hyperfine transitions, which make them ideal for inducing strong dispersion. By optically pumping a frequency region in the absorption profile of europium ions in yttrium orthosilicate, narrow and semi-permanent spectral transparency windows were created. This absorption structure causes a region of strong linear dispersion, where light pulses move at a rate $5 \cdot 10^5$ times slower than in vacuum. Mirrors deposited on the faces of this crystal form a cavity which acts as a highly stable frequency reference, where the dispersion can compensate any variations in length.



Key words

slow light effect, laser frequency stabilization, optical clocks, rare earths

Classification system and/or index terms (if any)

| Supplementary bibliographical information | Language |
|---|---|
| | English |
| ISSN and key title<br>0281-2762, Lund Reports on Atomic Physics, LRAP-602 | ISBN<br>978-91-8104-151-4 (print)<br>978-91-8104-152-1 (pdf) |
| Recipient's notes | Number of pages<br>145 / Price |
| | Security classification |

# Laser Frequency Stabilization Using a Slow Light Cavity

by David Gustavsson


LUND
UNIVERSITY

A doctoral thesis at a university in Sweden takes either the form of a single, cohesive research study (monograph) or a summary of research papers (compilation thesis), which the doctoral student has written alone or together with one or several other author(s).

In the latter case the thesis consists of two parts. An introductory text puts the research work into context and summarizes the main points of the papers. Then, the research publications themselves are reproduced, together with a description of the individual contributions of the authors. The research papers may either have been already published or are manuscripts at various stages (in press, submitted, or in draft).

**Cover illustration:** $Eu^{3+}$:$Y_2SiO_5$ crystal in the dark – Tove Landström, 2024



Faculty of Engineering, Department of Physics

ISBN: 978-91-8104-151-4 (print)
ISBN: 978-91-8104-152-1 (pdf)
ISSN: 0281-2762, Lund Reports on Atomic Physics, LRAP-602

Printed in Sweden by E-Husets Tryckeri, Lund University, Lund 2024

*Till Elsie och Hannes*

# Contents

# Abstract

Laser frequency stabilization is a necessary component in many modern technologies and physics experiments, providing spectral resolution for spectroscopic investigations, accurate optical clocks for timekeeping and phase stability for interferometry. The limiting factor to the frequency stability of state-of-the-art laser stabilization is frequency uncertainty as a result from variations in the length of the cavity used as a reference, due to Brownian motion of the atoms forming the mirrors. One way to mitigate this issue is to extend the cavity, thereby reducing the relative length uncertainty. This thesis describes a laser frequency reference which was built out of a plane mirror cavity surrounding a crystal of yttrium orthosilicate doped with rare-earth ions. These ions have narrow optical transitions and long lived hyperfine transitions, which make them ideal for inducing strong dispersion. By optically pumping a frequency region in the absorption profile of europium ions in yttrium orthosilicate, narrow and semi-permanent spectral transparency windows were created. This absorption structure causes a region of strong linear dispersion, where light pulses move at a rate $5 \cdot 10^5$ times slower than in vacuum. Mirrors deposited on the faces of this crystal form a cavity which acts as a highly stable frequency reference, where the dispersion can compensate any variations in length.

## List of publications

This thesis is based on the following publications, referred to by their Roman numerals:

I **Slow light frequency reference cavities—proof of concept for reducing the frequency sensitivity due to length fluctuations**
S. P. Horvath, C. Shi, D. Gustavsson, A. Walther, A. Kinos, S. Kröll and L. Rippe
*New Journal of Physics*

II **Using slow light to enable laser frequency stabilization to a short, high-Q cavity**
D. Gustavsson, M. Lindén, K. Shortiss, S. Kröll, A. Walther, A. Kinos and L. Rippe
*Manuscript submitted for publication*

III **Highly tuneable in-situ cryogenic switch bank resonator for magnetic field generation at radio-frequencies**
M. Lindén, D. Gustavsson, K. Shortiss and L. Rippe
*Manuscript in preparation*

IV **Resetting spectral hole features in Eu:YSO using a highly tunable radio-frequency resonance circuit**
M. Lindén, D. Gustavsson, A. Walther, A. Kinos and L. Rippe
*Manuscript in preparation*

V **Pushing the limits of negative group velocity**
A. J. Renders, D. Gustavsson, M. Lindén, A. Walther, S. Kröll, A. Kinos and L. Rippe
*Manuscript submitted for publication*

# Acknowledgements

I would like to thank my advisors, Lars, Adam, and Stefan, for their advice, comments and knowledge.

The other people working on the laser stabilization project with me, Marcus, Sebastian, Chunyan, and Kevin. Other colleagues and master's students in the Quantum Information group who contributed suggestions, help and a good atmosphere. Fellow PhD students and researchers at the division of Atomic Physics, whose width and depth of specialization was a great inspiration. Furthermore, I owe much to the supporting, administrative, teaching and technical staff at the division and the department of physics.

Completing a project like this would be very difficult without unwavering support from home, and I am blessed with a very large, very unwavering family. Special among them is Tove, who held the fort during many late nights in the lab, and the lab who held the fort with her, Alice.

The educational and social quality of my time at Lund University, up to and including my research education, has been ensured by the tireless work of volunteers at the Student Union, TLTH.

Some of my most instructive moments in physics have been while teaching it – I would like to extend a thank you to insightful and inquisitive students, who are the best teachers a teacher can hope for.

## Popular scientific summary in English

In 1966, Bob Shaw – prolific writer of science fiction – published a short story titled *Light of Other Days*[6]. A travelling couple drop by a manufacturer of "slow glass", a material where light travels at an extremely low velocity. A pane can be moved from an idyllic lakeside to an office, mine, or flat where the view is less appealing. As the light, which entered on one side when the pane looked over a sunny lake, exits on the other side which now faces the less scenic environment, the inhabitants of the new location get a lake view. Unbeknownst to the visiting couple, the woman who they see through the window of the cottage performing chores is an echo of the salesman's several years deceased wife – a much darker use of the same technology.

At the time when Shaw wrote this, the *slow light effect* had recently been discovered (though it is uncertain whether the discovery inspired the short story). Dispersion – different wavelengths (or colours) of light travelling at different velocities – causes pulses of light to move at much lower velocities than the components from which they are constituted.

Slow light effects of $10^{18}$ (a 1 followed by 18 zeros), as required to have a centimetre thick window pane emit light a year after it enters, are sadly still science fiction. But through careful control of the response of a rare-earth material to different wavelengths of light, the effect can be made to exceed $5 \cdot 10^5$. This is enough to delay light pulses travelling through a two centimetre thick crystal by 30 microseconds, or the same amount as if that crystal was ten kilometres long. In other words, the speed of pulses of light is 550 meters per second, just slower than the 600 meters per second supercruise velocity of a Concorde aircraft. This is not useful for brightening a drab office, but can be extremely useful in a clock:

A light pulse travelling back and forth between two mirrors will return to the same position with high regularity – as long as the distance between the mirrors is constant, each round trip will take the same amount of time, like the pendulum of a grandfather clock. Unfortunately, keeping the distance between the mirrors sufficiently constant for today's scientific state-of-the-art clocks is a technical challenge. The current limit to how repeatably this optical clock ticks is the miniscule motions of the atoms that make up the mirrors, which makes the distance vary slightly over time. This problem gets smaller the further apart the mirrors are because the length changes are a smaller portion of the entire length.

By inserting a slow light crystal between the mirrors, we can effectively make an optical clock with a cavity length of kilometres. In this thesis, I describe a cavity with two mirrors separated by 21 millimetres of a rare-earth ion doped material, which acts as if the mirrors were ten kilometres apart. A reference like this could be used to stabilize a laser for use in metrology, astrophysics, or tasks at the frontiers of modern physics like gravity wave detection.

## Populärvetenskaplig sammanfattning på svenska

1966 skrev Bob Shaw – flitig författare av science fiction – en novell med titeln *Light of Other Days*[6] (*Andra dagars ljus*). Ett par på semester besöker en tillverkare av "långsamt glas", ett material där ljus färdas extremt långsamt. En skiva kan flyttas från en idyllisk strand till ett kontor, en gruva eller en lägenhet där utsikten är mindre bildskön, och efter hand som ljuset, som gick in i glaset när fönstret såg ut över en solig sjö, kommer ut på andra sidan som nu är vänt mot en mindre scenisk omgivning får den nya lokalens invånare plötsligt sjöutsikt. Det besökande paret ser en kvinna genom ett stugfönster, men vad de inte vet är att hon är ekot av försäljarens sedan flera år avlidna hustru – ett mycket mörkare användningsområde för samma teknik.

När Shaw skrev denna novell var *slow light-effekten* nyligen upptäckt (men det är osäkert ifall upptäckten inspirerade novellen). Dispersion – en variation i ljushastighet med våglängd (färg) – gör att ljuspulser färdas mycket långsammare än de ingående vågorna.

Slow light-effekter så höga som de $10^{18}$ (en etta följd av arton nollor), som skulle behövas för att en centimetertjock fönsterruta skulle hålla i solljus i ett år, är tyvärr fortfarande science fiction. Men genom att noggrant styra hur ett material av sällsynta jordartsmetaller reagerar på ljus av olika våglängder kan effekten fås att överstiga $5 \cdot 10^5$, tillräckligt för att försena ljus genom en två centimeter lång kristall med 30 mikrosekunder, lika mycket som om den kristallen var tio kilometer lång. Med andra ord blir ljuspulsernas fart 550 meter per sekund, strax under Concorde-planets supermarschfart, 600 meter per sekund. Det här är så klart inte användbart för att lysa upp ett tråkigt kontor, men det kan vara extremt användbart i en klocka:

En ljuspuls som färdas fram och tillbaka mellan två speglar återvänder till samma punkt ytterst regelbundet – så länge avståndet mellan speglarna hålls konstant tar varje rundtur lika lång tid, likt pendeln i ett golvur. Tyvärr är det tekniskt utmanande att hålla avståndet mellan speglarna tillräckligt konstant för dagens bästa vetenskapliga klockor, och just nu är den begränsande faktorn för hur exakt klockan tickar små rörelser hos atomerna som utgör speglarna, vilket gör att avståndet varierar något över tid. Det här problemet blir mindre ju längre ifrån varandra speglarna placeras eftersom längdförändringarna blir en mindre andel av den totala längden.

Genom att införa en slow light-kristall mellan speglarna kan vi i princip tillverka en optisk klocka med en flera kilometer lång kavitet. I den här avhandlingen beskriver jag en kavitet där två speglar omger 21 millimeter av ett material dopat med sällsynta jordartsmetalljoner, som agerar som om speglarna var tio kilometer ifrån varandra. En sån här frekvensreferens skulle kunna användas för att stabilisera en laser till mätteknik, astrofysik, eller uppgifter vid den moderna fysikens frontgränser, som gravitationsvågsdetektion.

# Laser Frequency Stabilization Using a Slow Light Cavity

*When light encounters a strong magical field it loses all sense of urgency. It slows right down. And on the Discworld the magic was embarrassingly strong, which meant that the soft yellow light of dawn flowed over the sleeping landscape like the caress of a gentle lover or, as some would have it, like golden syrup.*

— Terry Pratchett, *The Light Fantastic*

# Chapter 1

# Introduction

## 1.1 Background

### 1.1.1 History of time keeping

The history of frequency references starts with the planets and the stars – the rotation of Earth around its axis generates a quite stable frequency of $\nu = \frac{1}{\text{day}}$, the revolution of the moon relative to the Sun-Earth axis defines a frequency $\nu = \frac{1}{\text{month}}$, and the revolution of Earth around the Sun, compared to our polar tilt axis, defines $\nu = \frac{1}{\text{year}}$. These would all have been important to early humans to keep track of, especially with the invention of agriculture. Though in daily parlance we often discuss these events in terms of their period, I describe them as frequencies to make clear that these are not *clocks*, but *frequency generating devices*: You cannot look at the moon and tell which month it is, to do so you need to couple it with some time keeping record, like a calendar, and it is this record that turns a frequency reference into a clock. For time periods shorter than a day, and to be able to tell the time even when the sun was out of sight, humanity needed man-made frequency generators. The general trend was to go to faster and faster devices – in the 1700s, hourglasses and candle clocks gave way to pendulum clocks and mechanical spring chronometers, and in the early 1900s quartz watches were invented which could use the $\approx$ kHz oscillation of piezo-electric crystals as a frequency generator [7]. The motivation for moving to higher frequencies is the faster response. Intuitively a clock which ticks once a second is more precise than the movement of the moon for determining a time period of a minute. But even for frequencies below the characteristic frequency of either reference, a reference with larger frequency will give a higher count in the same amount of time, meaning an overall increase in precision. Some frequency references and their characteristic frequencies are shown in fig. 1.1.



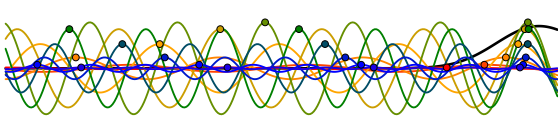

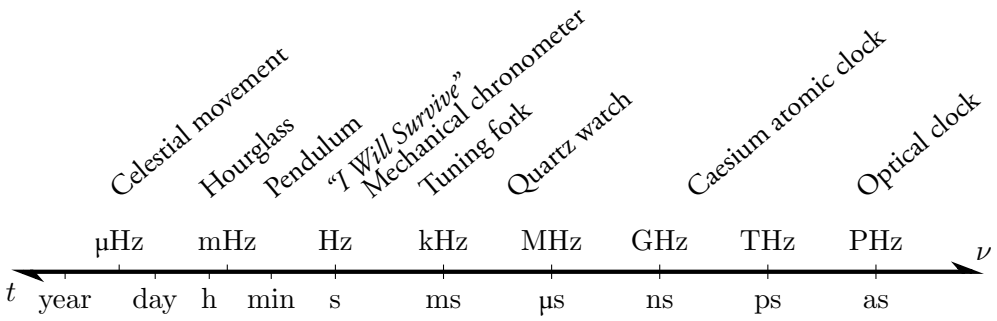


Figure 1.1: Some historic clocks and frequency references roughly arranged by characteristic frequency or period.

### 1.1.2 Tangent: acoustic frequency references

In parallel with these developments in time keeping, stable frequency references were independently invented for another purpose: Music. Many musical instruments will maintain a tuning over the course of a performance, but not necessarily over a span of days. As strings and pipes repeatedly cool down and heat up, their output frequency (or *pitch*) will drift. In order to ensure that ensemble musicians could keep playing together long term, without running into the physical limits of their instruments or voices, notes needed to be standardized, and stable pitch references needed to be established. Two main technologies emerged – tuning forks and organ pipes. In both cases, the resonance frequency is a physical property of a metallic object, which might vary with the conditions, but not plastically so. A tuning fork will repeatably return to the same frequency at the same temperature. This stability did not, however, necessarily translate into absolute standardization.

In 1880, mathematician and musicologist Alexander J. Ellis published the results of an ambitious project, where he carried a box full of slightly detuned tuning forks to various church organs, tuning forks, and other permanent standards throughout Europe and registered the frequencies of their As. I have summarized his findings in fig. 1.2. What he found was that the frequency standards in use up until that point were as far as a fifth apart (meaning a frequency quotient of 1.5), and that frequencies on the whole had been increasing steadily for about a century. A number of absolute standard values for the pitch of A remain to this day, varying between countries and musical genres. However, in large part thanks to the cultural domination of the United States during the 1900s, a majority of musicians follow the American standard of $A = 440\,\mathrm{Hz}$. [8]

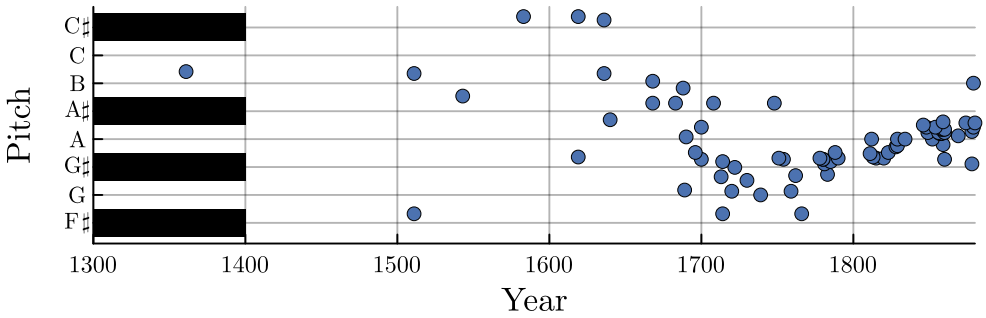


Figure 1.2: Pitches (frequencies) of As of organs, tuning forks, and various other acoustic frequency references reported by A.J. Ellis in 1880 [9]. The year on the horizontal axis is an approximate year the reference was created, and the scale on the vertical axis is modern day 12-tone equal temperament, with A = 440 Hz (logarithmic in frequency).

### 1.1.3 Modern day timekeeping

In the 1950s, Louis Essen and Jack Perry realized a frequency reference based on an RF resonator tuned to the transition between the hyperfine levels of the ground state in caesium 133, which they could show was both more stable and accurate than the accepted definition of a second, at the time still based on Earth's rotation [7, 10, 11]. Following this introduction of atomic clocks, the second gained its current definition as 9 192 531 770 oscillations on that caesium transition in 1967 (making the transition frequency exactly 9.192 531 77 GHz). By 2024, a need for a new definition of the second has been identified, as there are applications that require higher accuracy than that with which the caesium transition can be measured. Ref. [12] identifies three candidates for redefinition:

The first candidate is to simply pick another atomic transition, which can be measured with higher precision than the caesium transition, and define the second as a constant number of oscillations on that transition instead. There is no consensus on which transition to use, but the majority of the suggested transitions are *optical* transitions, taking place at frequencies between 410 THz (red, bordering on infrared) and 1.1 PHz (middle ultraviolet). These frequencies are 4 to 5 orders of magnitude higher than the caesium standard, which as previously discussed, enables higher time precision.

The second option for redefining the second is to pick more than one transition and define the second as a weighted geometric mean of their periods. This offers the advantage of not relying entirely on measuring any one transition, partially avoiding the problem of building consensus around which transition that should be. There is even a suggestion for a dynamic version of this definition, where the weights can be periodically updated to reflect progress in specific experiments. The downside to this is that it becomes less intuitive, requires a



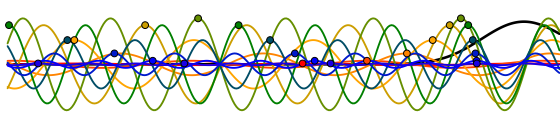

larger set of conversion constants and a more involved experiment to realize.

Thirdly, one could fix the value of some fundamental physical constant, as is currently done with the speed of light in vacuum, the elementary charge, the Planck constant, and the Boltzmann constant to define most of the rest of the base units. This option has the allure of tying another base unit to the core of fundamental constants, leaving only the mole and the candela defined by more arbitrary conversion factors. Unfortunately, none of the proposed constants can be measured with the precision with which we can currently measure the caesium standard, so this definition would represent a step back when it comes to the main motivation for the redefinition.

If an optical atomic frequency standard is adopted, optical transitions will need to be measured using lasers. The stability of these lasers can easily become the limiting factor for the clock's stability, as it determines for how long the atoms can be coherently probed [13]. In order to improve the laser's stability, it can be pre-stabilized to some relative reference, characterized by narrow linewidths and low drift rates. The main text of this thesis concerns the development of a reference where linewidth and drift rate are both reduced by the slow light effect. This reference could be used to pre-stabilize the laser for an optical clock, or for any physics experiment where and ultra-narrow linewidth is required.

## 1.2 Thesis outline

The second half of this thesis consists of five scientific manuscripts – papers I to V. In this first half of the thesis I will go into the background theory required to interpret those papers, as well as expand on the results and conclusions.

In chapter 2 I discuss the purpose and implementation of laser frequency stabilization. I will also describe the state of the art, and the requirements on a system hoping to improve on it.

In chapter 3 I will describe how strong dispersion can help achieve some of these requirements, in what we call slow light laser frequency stabilization. I will further show how this strong dispersion can be induced in an absorbing material using spectral tailoring. There will also be a digression into the *fast* light effect, and a discussion of its implications.

Chapter 4 dives into the materials used in this work, the rare-earth metals. I will describe what makes them appropriate both for quantum information applications and for spectral tailoring techniques like the present stabilization scheme, and how spectral tailoring in these materials is actually performed.

The next chapter, chapter 5, brings all of this together – showing how the properties of rare-earth metals enable large and controllable dispersion, which in turn leads to frequency

stability in a cavity. Here I also discuss some of the practical details that went into implementing this scheme experimentally, including the crystals used.

The final chapter in the main text, chapter 6, is a quick outlook, discussing possible future experiments as well as general conclusions from my studies.

After this the papers begin, starting with a summary of my contributions to each manuscript. The first two articles, papers I and II, concern the laser stabilization scheme, the former is a proof-of-concept implementation using praseodymium, and the latter is a more optimized implementation in europium. The next two, papers III and IV, describe a method to erase spectral structures using radio frequency magnetic fields – the first describes the antenna used as a general instrument, and the second the scheme as it relates to our atomic environment specifically. The final article, paper V, is an implementation of the fast light effect in europium.



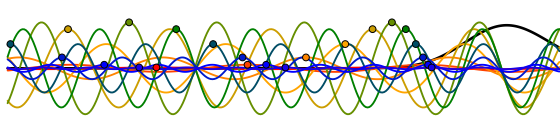

# Chapter 2

# Laser frequency stabilization

In order to measure time or frequency accurately over long times using lasers, one needs to tie the frequency of the laser to some stable physical reference. This is a necessary step in many modern physics experiments where narrow linewidths and low drift rates are required to detect small changes in frequency, enabling tests of relativity [14, 15] and gravity wave detection [16, 17]. As discussed in section 1.1.3, pre-stabilized lasers also constitute the frequency generating elements in optical clocks [18]. This chapter aims to introduce the general technology used in this thesis, and the challenge to be overcome.

## 2.1 State of the art – Fabry-Perót interferometers

One type of physical frequency reference is an interferometer, which uses interference to indirectly measure the phase contribution of a path. The simplest example is the Fabry-Perót interferometer, which consists of two mirrors with non-unity reflectivity, a set distance apart. If the round-trip phase contribution through the cavity is a whole number of turns ($2\pi q$ for an integer $q$), the small field that enters through the first mirror interferes constructively with the light that has travelled through the cavity and builds up, until it leaks out of the far side mirror – you get large transmission. Meanwhile, the light that leaks out of the first mirror is out of phase with the incoming light. As the field in the cavity grows, the leaking field increasingly extinguishes the reflected wave. If the phase contribution is not (close to) a whole number of turns, the cavity simply acts like a mirror. In total, the frequency of light that is transmitted through the interferometer is tied to its cavity length [19, Chapter 7]. The linewidth of a Fabry-Perót cavity, that is the frequency span around the



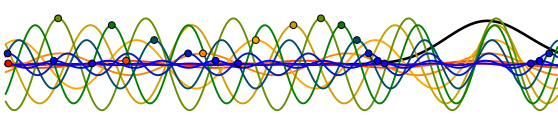

resonance frequency within which more than half of the intensity is transmitted, is

$$\Delta\nu = \frac{-2\ln(R_1 R_2)c_0}{2n\pi L} \tag{2.1}$$

with mirror reflectivities $R_1$, $R_2$, cavity length $L$, the refractive index inside the cavity $n$ [20], and the light speed in vacuum $c_0$.

The state of the art in optical frequency stabilization is Fabry-Perót cavities with spacers made from ultra-low expansion (ULE) glass, which to first order do not vary in length with temperature. It has been shown that these cavities' stability is currently limited by Brownian motion in their mirrors – the miniscule length uncertainty that arises from movement of the atoms in the mirror coating is the largest contributor to frequency uncertainty [21]. Getting around this has hitherto involved a combination of four main strategies: Averaging over more atoms by making a larger area beam, reducing the magnitude of the Brownian motion by lowering the absolute temperature, restricting the movement of the mirror atoms by creating monocrystalline mirrors, and lowering the relative magnitude of this effect by increasing the total cavity length.

The beam area is an important factor, because Brownian motion is random and independent across the mirror face, so the larger the beam, the more atoms are interrogated, and the more the noise is averaged down. The noise scales as the square root of the area, linearly with the beam radius [21]. This factor is largely limited by the manufacturing of optical components.

Brownian motion scales with the square root of the absolute temperature of the atoms [22], so every two orders of magnitude reduction in temperature – like going from room temperature to liquid helium temperatures – causes one order of magnitude decrease in Brownian noise [23]. Another order of magnitude improvement along this avenue would require cooling to the 10 mK level, which imposes heavy requirements on the experimental setup.

The conventional method to create mirrors for optical frequency reference cavities involves a stack of amorphous dielectric layers, often deposited by ion beam sputtering. These layers display large mechanical damping, meaning they are essentially soft. By instead epitaxially growing monocrystalline layers, one can make the mirrors stiffer, reducing the freedom of movement of the atoms. This has shown between one and two orders of magnitude improvement over amorphous mirrors [24, 25].

Finally, the frequency variation scales with the *relative* length variation, so the noise scales with the reciprocal of the total cavity length. By making a 48 cm long cavity, temperature stabilized at room temperature and isolated from mechanical noise, Ref. [26] showed a relative frequency stability below $10^{-16}$ above 1 s. Increasing the size beyond this level is proving very difficult, as it puts tough requirements on the mechanical and thermal stabilization.

## 2.2 Pound-Drever-Hall locking

In order to stay resonant with a cavity mode, transferring the stability of the cavity to the laser, a feedback loop needs to be established. One could measure the transmitted power, and continuously adjust the frequency to keep this power constant. To get an asymmetric error signal, you could do this at the side of a mode, where the intensity is a measure of which direction to shift the frequency. This method does not, however, differentiate between frequency and power fluctuations. If the power varies for another reason, the servo will erroneously vary the frequency as a response.

The Pound-Drever-Hall (PDH) technique, proposed in 1983 by R.W.P. Drever (Ref. [27]), gets around this issue by locking to the reflected power, rather than the transmitted. The immediate advantage is that this power is 0 at resonance, so the measured power around resonance is decoupled from input power fluctuations. The trick to getting an asymmetric error signal is to look not at the absolute value of reflected power, but at its derivative with respect to frequency. To achieve this, the PDH technique adds a relatively slow sinusoidal frequency modulation to the probing beam and measures the phase of the response relative to the phase of the modulation. In fig. 2.1 I have illustrated how the reflected intensity varies with time for a beam modulating around a frequency either below or above the resonance frequency. Considering a point in time when the modulation signal is rising (the phase of the sine signal $\approx 0$), as illustrated by the arrows in the figure, the reflected power will either be decreasing or increasing, depending on which side of the resonance is probed. This means the reflected signal will be out of phase with the modulation signal if the frequency is below resonance, and in phase with it if the frequency is above resonance.

The reflected power is measured by a photodetector, and the DC component of this signal is removed using a high-pass filter. The resulting signal is vaguely sinusoidal with the same frequency as the modulation signal. Multiplying the two together with an electronic mixer gives a slowly varying signal that is positive if they correlate positively, meaning the laser is above resonance, or negative if they correlate negatively, meaning the laser is below resonance. This error signal is used in the feedback loop to steer the laser frequency towards the resonance, as shown in fig. 2.2.

Beyond decoupling power and frequency fluctuations, using the reflected signal has the added benefit of giving a fast response: the transmitted light field reflects the steady-state of the cavity, and requires a build-up for a frequency change to be measurable. In contrast, the reflected signal is a more immediate measurement of the phase difference between the cavity mode and the incident field [27, 28].



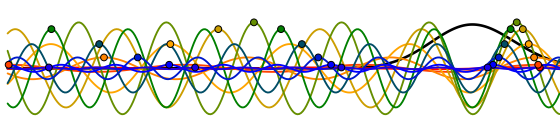

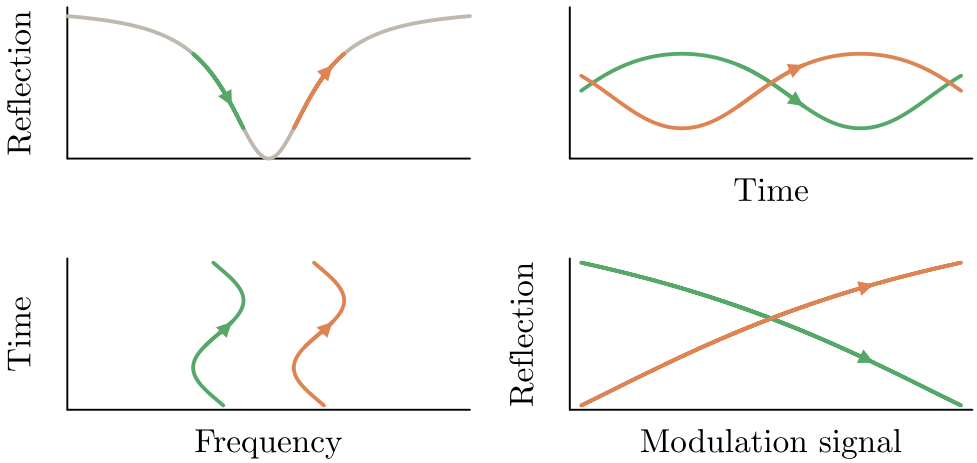


Figure 2.1: The reflectivity of a cavity mode at frequencies around resonance, probed with a laser that is modulated around a centre frequency below (green) or above (orange) resonance. The arrows point in the forward direction of time around the same point in time for each figure. The top two figures share a vertical axis, and the left two share a horizontal axis. The correlation (slope) between the modulation signal and the reflectivity is negative below resonance and positive above resonance.

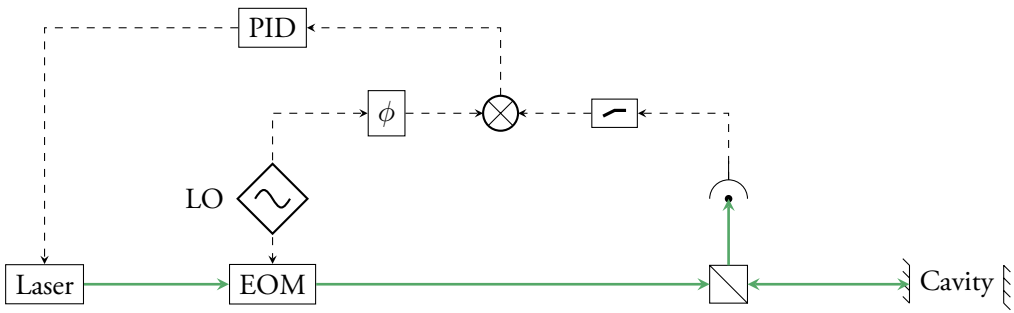


Figure 2.2: Simplified circuit diagram for Pound-Drever-Hall locking. The light from a laser is modulated by an EOM, and then incident on a Fabry-Perót cavity. The reflected light is picked off onto a photodetector. The measured intensity is high-pass filtered to remove the DC component, and this signal is mixed with the local oscillator (LO) signal to yield a DC error signal. A phase shifter ($\phi$) is manually tuned and used to compensate phase delays in the circuit. Finally, the error signal is fed to a PID regulator, which feeds back to the frequency control on the laser – keeping it on resonance with the cavity.

# Chapter 3

# Dispersion

In this chapter, I will introduce the tool we use to increase the stability of our frequency reference: Dispersion, and specifically the slow light effect.

## 3.1 Susceptibility of absorbing media

Real physical systems all display *causality* – they respond to stimuli only after receiving them. Another property of most real world systems is *linear-shift invariance*, or *time invariance*, meaning that if a stimulus is shifted in time, the response is also shifted in time by the same amount but otherwise remains equal. Even systems that change slowly over time can often be modelled as causal and time invariant, and their frequency response then follows a couple of equations known as the *Kramers-Kronig relations* [19, appendix B].

$$\begin{aligned} H'(\nu) &= \frac{2}{\pi}\int_0^\infty \frac{sH''(s)}{s^2-\nu^2}\mathrm{d}s \\ H''(\nu) &= \frac{2}{\pi}\int_0^\infty \frac{\nu H'(s)}{\nu^2-s^2}\mathrm{d}s \end{aligned} \tag{3.1}$$

where $H'$ and $H''$ are the real and imaginary parts, respectively, of the frequency response of a causal, linear-shift invariant system and $\nu$ and $s$ are frequencies. The implication here is that knowing the real part of the frequency response uniquely determines the imaginary part and vice versa.

Especially relevant for this thesis is the special case of absorbing ions. Here, the frequency response corresponds to *electric susceptibility*, in a sense how much the ions' electrons are polarized in response to a light field at the given frequency. The imaginary part of the



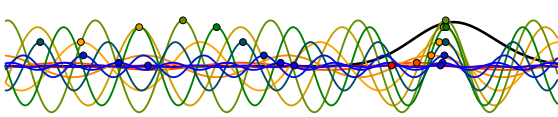

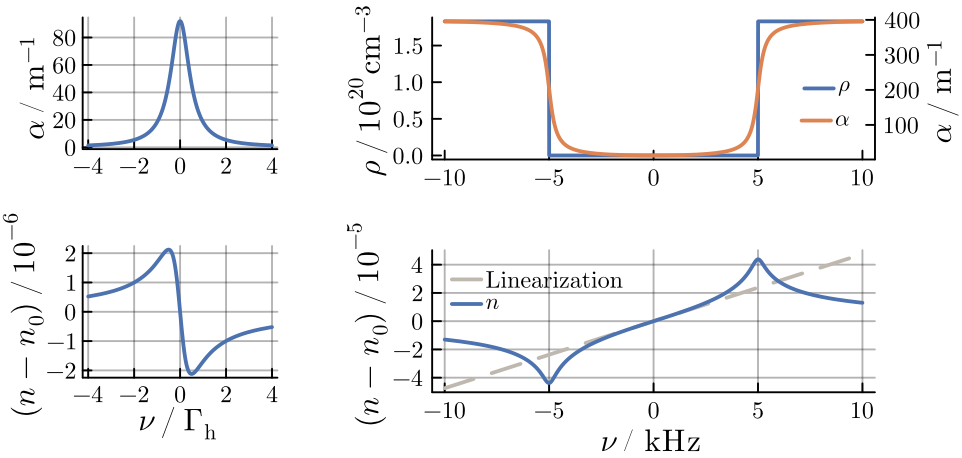


(a) A single Lorentzian absorption line, and the resulting contribution to the refractive index.

(b) A 10 kHz wide window. Ion population and absorption coefficient (top), and refractive index (bottom). The dashed line in the bottom graph is the Taylor expansion of the refractive index around $\nu = 0$.

Figure 3.1: Absorption and refractive index for a single ion and a spectral window.

susceptibility gives the absorption coefficient, and the real part gives the ions' contribution to the refractive index. If an ion has a transition at frequency $\nu = 0$ and a lifetime broadened absorption with linewidth $\Gamma_h$, so that the absorption, $\alpha$, is Lorentzian ($\alpha \propto \left(1 + 4\nu^2/\Gamma_h^2\right)^{-1}$), then assuming causality and linear-shift invariance allows us to decide a corresponding addition to the refractive index. These are shown in fig. 3.1a.

Adding more ions nearby in frequency, the susceptibility becomes a convolution of the population distribution and this homogeneous profile, and the refractive index can be calculated by the same method. Of special interest to this thesis is the case of a spectral window with a square population distribution – where the population $\rho(\nu)$ of ions whose absorption peak frequency is $\nu$ is zero within a frequency region of width $\Gamma_{win}$ around a centre frequency $\nu_{win}$ and some large population $\rho_0$ outside it:

$$\rho(\nu) = \begin{cases} 0 & |\nu - \nu_{win}| < \frac{\Gamma_{win}}{2} \\ \rho_0 & \text{otherwise} \end{cases} \tag{3.2}$$

as shown in fig. 3.1b (top). The resulting absorption profile, $\alpha(\nu)$, given by a convolution of this population distribution and the homogeneous line shape of width $\Gamma_h$ in fig. 3.1a

(top), is

$$\alpha(\nu) = \alpha_0 \left(1 + \frac{1}{\pi}\arctan\left(\frac{2(\nu-\nu_{\text{win}}) - \Gamma_{\text{win}}}{\Gamma_{\text{h}}}\right) - \frac{1}{\pi}\arctan\left(\frac{2(\nu-\nu_{\text{win}}) + \Gamma_{\text{win}}}{\Gamma_{\text{h}}}\right)\right) \tag{3.3}$$

with a maximum absorption $\alpha_0$. With a narrow enough homogeneous linewidth, $\Gamma_{\text{h}}$, relative to the window width, $\Gamma_{\text{win}}$, the absorption will appear like a slightly rounded square function. If the window is too narrow, however, the window edges will be less sharp, relatively, and there will be a substantial off-resonant absorption in the centre of the window from the ions in the edges. The window in fig. 3.1b is intentionally chosen quite narrow, relative to what is used in the rest of this work, to illustrate the difference. The absorption in the absolute centre of the window, $\alpha_{\text{c}}$, is found by inserting $\nu = \nu_{\text{win}}$ into eq. (3.3),

$$\begin{aligned}\alpha_{\text{c}} = \alpha_0 \left(1 + \frac{1}{\pi}\arctan\left(-\frac{\Gamma_{\text{win}}}{\Gamma_{\text{h}}}\right) - \frac{1}{\pi}\arctan\left(\frac{\Gamma_{\text{win}}}{\Gamma_{\text{h}}}\right)\right) = \\ \alpha_0 \left(1 - \frac{2}{\pi}\arctan\left(\frac{\Gamma_{\text{win}}}{\Gamma_{\text{h}}}\right)\right) \approx \\ \frac{2}{\pi}\frac{\Gamma_{\text{h}}}{\Gamma_{\text{win}}}\alpha_0 \,.\end{aligned} \tag{3.4}$$

The last approximation holds when $\Gamma_{\text{h}} \ll \Gamma_{\text{win}}$.

Solving the Kramers-Kronig relations for eq. (3.3), as is done in paper I, gives a refractive index, $n(\nu)$, that varies around the host refractive index, $n_0$, like

$$n(\nu) = n_0 + \frac{c_0\alpha_0}{4\pi^2\nu_0}\ln\left(\frac{\Gamma_{\text{h}}^2 + (\Gamma_{\text{win}} + 2(\nu-\nu_{\text{win}}))^2}{\Gamma_{\text{h}}^2 + (\Gamma_{\text{win}} - 2(\nu-\nu_{\text{win}}))^2}\right) \tag{3.5}$$

shown in fig. 3.1b (bottom). This was derived from an ideal square window, but holds approximately for similar, less perfect structures. An intuitive view of this is to consider the contribution illustrated in fig. 3.1a of each of the ions near the edges. At a frequency just above a sharp drop in population (right of the left edge), there will be a negative contribution to the refractive index from the ions absorbing at lower frequencies, and at a frequency just below a sharp rise in population (left of the right edge), each of the ions absorbing at higher frequencies will contribute a positive shift.

In an absorbing medium with a sharp transparent region like this, there will be a region of nearly linear dispersion, and the slope increases with increasing window "depth" (absorption outside the window) and decreasing window width. Linearizing eq. (3.5) around $\nu = 0$ gives

$$n(\nu) \approx n_0 + \frac{2c_0\alpha_0}{\Gamma_{\text{win}}\pi^2\nu_0}\nu \tag{3.6}$$

.



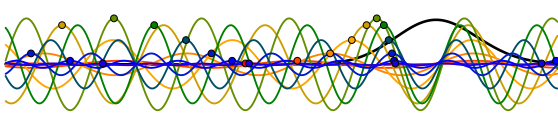

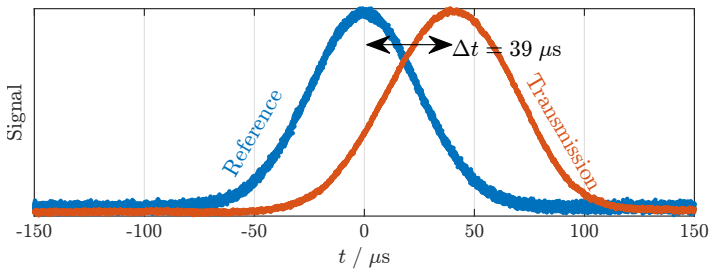


(a) A gaussian pulse recorded on a reference detector (blue), and 39 µs delayed on a transmission detector – having travelled through 21 mm of a slow light-enabled crystal at a speed of 540 $\mathrm{m\,s^{-1}}$.

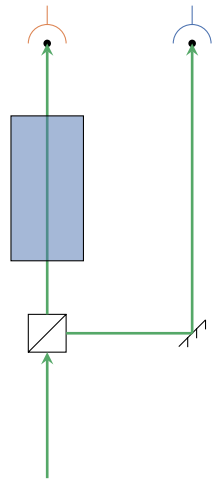

(b) Schematic setup to measure pulse delay.

Figure 3.2: Direct measurement of a pulse delayed by the slow light effect.

## 3.2 Slow light effect

Dispersion like in eq. (3.6) causes an effect known as the slow light effect, where pulses of light travel at the group velocity, $v_g$, which can be far below the vacuum light speed, $c_0$. The group velocity in a region around a frequency $\nu_0$ with linear dispersion $\mathrm{d}n/\mathrm{d}\nu$ is

$$v_g = \frac{c_0}{n_0 + \frac{\mathrm{d}n}{\mathrm{d}\nu}\nu_0} \,. \tag{3.7}$$

A mathematical derivation is available, for example, in Ref. [19] (chapter 5.6) but an intuitive understanding can be gleaned from the animation in the bottom right corner of this thesis. Detailed usage instructions in section 3.2.1.

The simplest way to display the slow light effect in a material is to simply send a light pulse through it and time its arrival. Section 3.2 shows a pulse that has passed through 21 mm of our material but is delayed by 39 µs. In this time, light would have travelled 12 km in vacuum. In chapter 5 I will discuss how this affects cavities, but this picture of extending the path length for light pulses is accurate in many respects.

Table 3.1: Parameters for the slow light animation in the bottom right corner of this thesis. These are arbitrarily chosen to illustrate the effect.

| Parameter | |
|---|---|
| Pulse length | 9.7 fs |
| Wavelength range | 460 nm – 790 nm |
| Dispersion coefficient | $1.0 \cdot 10^{-14}\,\mathrm{Hz}^{-1}$ |
| Refractive index | 1.8 |
| Group refractive index | 7.2 |
| Time step between pages | 1.5 fs |

### 3.2.1 Animation

In the bottom right corner of this thesis, there is a simplified animated illustration of the slow light effect. By quickly flicking through these pages, you should experience the illusion that this graph is moving. The horizontal axis is space, and the vertical axis is the electric field. Time increases with *decreasing* page numbers (for the flip-book functionality). In rainbow colours are drawn the real electric field components for a few light waves of different wavelengths. Some peaks are marked with dots, to make following the waves easier. Between these are a continuum of wavelengths, which are not visualized as it would clutter the image. In black is shown the square sum of these light waves – a Gaussian pulse. What should be visible here is that as the individual light waves move to the right, the longer waves catch up with the shorter, and the region where they are in phase moves with a much lower speed. This region of constructive interference is where the pulse will have its maximum, so the pulse moves at a much slower speed than the constituent waves.

The parameters of this simulation (table 3.1) are arbitrarily chosen to illustrate the effect, so that the group velocity is one fourth of the phase velocity, and the length of the pulse is similar to the wavelengths. The rainbow colours illustrate the spectral order of the wavelengths correctly – shorter waves are blue, longer waves are red – but do not correspond to the actual colour of the waves.

## 3.3 Fast light effect

One might notice that there is nothing special about the positive sign of the dispersion coefficient in eq. (3.7). In fact, it is entirely feasible, albeit more practically difficult, to create a spectral structure that causes negative slopes, leading to an *increase* in group velocity relative to the phase velocity. With careful control of the dispersion coefficient, the group velocity can even be made infinite or negative.



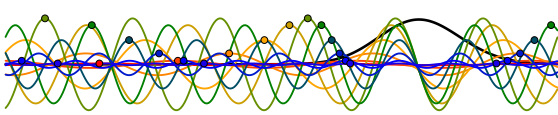

In paper V, a structure was created where the dispersion ($\mathrm{d}n/\mathrm{d}\nu$ in eq. (3.7)) is large and negative, leading to a negative group velocity. Intuitively this corresponds to light pulses propagating backwards through the material, and exiting the far face before arriving at the near face. As the backwards-propagating pulse reaches the near face, it interferes destructively with the incoming pulse, causing both to cancel out. This is also the result demonstrated in this paper. To do this, we prepared a spectral window like in fig. 3.1b, but inverted the population outside the window, leading to a region of zero absorption between regions of negative absorption.

How does this not break causality? Just like with other faster-than-light results, the important question is not how fast an entity *moves*, but how fast it can transfer information. In the case of light pulses, no information can be encoded in whether or not a pulse is present, as its spectral composition is constant with time – one could measure the spectrum of the first light waves to arrive and predict the pulse peak, so that information arrives with the phase velocity of the constituent waves. We might then expect the phase velocity to be the true information velocity, but in lower-than-unity refractive index materials this also breaks causality. In fact, a third velocity, the *information velocity*, or *discontinuity velocity*, arises. This is the velocity at which discontinuities in some time derivative of the light field propagate through the material, and such discontinuities is the only way to truly encode information in light. [29]

If we create a Gaussian pulse with a discontinuity and send it through an extreme anomalous dispersion material, the pulse exits early as a whole Gaussian, just like if there was no cut. Then as the discontinuity arrives with the information that the Gaussian was interrupted, the output light responds with a strong oscillation. If the information to be transmitted was at which point the Gaussian pulse was cut, this information can in theory be recreated from the response, but not until after the arrival of the discontinuity, which gives a total information velocity lower than the speed of light in vacuum.

Some suggestions have been made for practical uses of this effect, but it is not a settled matter whether it actually provides an experimental benefit. Instead, we chose to treat it as a showcase of spectral control – the rare-earth platform introduced in chapter 4 lends itself well to this kind of tailoring of absorption and dispersion. We demonstrated almost an order of magnitude improvement over previous attempts at fast light by using well-developed and generally useful tailoring techniques.

# Chapter 4

# Rare-earth metals

## 4.1 Properties of rare earths

Starting at the end of the 1700s, a number of elements were discovered in minerals from a mine in Ytterby, Sweden. Like all things upon first discovery, these earths (as scientific parlance called them at the time) had never been seen before, and they were therefore termed "rare". These Ytterby elements, together with a few of their neighbours in the periodic table, now constitute a set called the *rare earths*: Scandium (element 21), Yttrium (39), and the Lanthanides (57 to 71), marked red in fig. 4.1. About half of them were named for their connection with Ytterby, Stockholm, Sweden, Scandinavia or the original discoverer, Johan Gadolin. Contrary to what their name would suggest, they are fairly abundant, though extracting them is quite expensive. Just last year, for instance, a large deposit of rare-earth metals was discovered in Kiruna, Sweden [30].

What connects the rare earths, and what makes them useful to information and quantum technology, is a quirk of atomic physics: For most other elements in the periodic table, the highest energy orbital also has the largest mean radius. This is not the case for the rare earths, whose valence electrons in the 4f shell are shielded by higher radius, but lower energy, filled 5p and 5s shells. This makes them chemically similar, and gives them uniquely stable excited states, less affected by disturbances in their spatial environment.

For quantum information applications, the long lifetimes and narrow homogeneous linewidths make rare earths promising candidates for quantum memories and repeaters for long range quantum communication [31]. If the ions are embedded into a crystalline material, their valence electrons are shielded from the surroundings, turning the system into a natural ion trap.



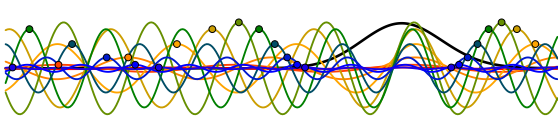

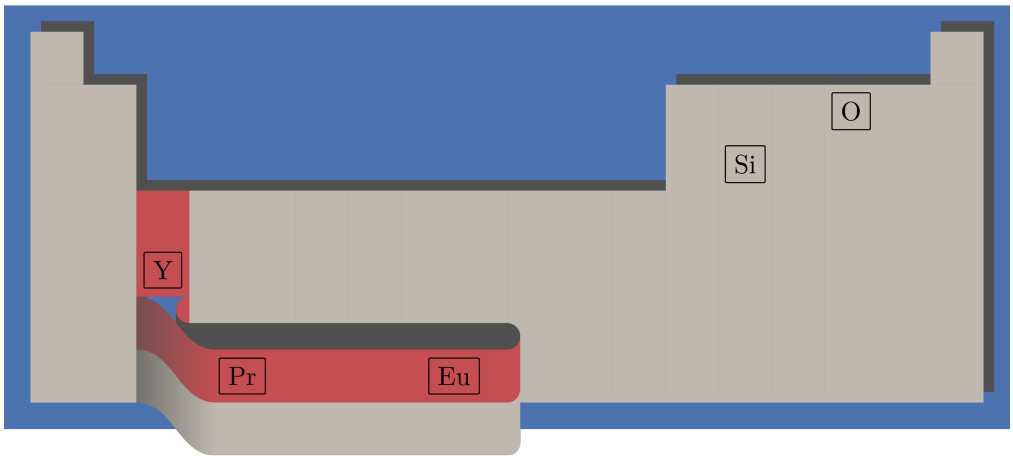


Figure 4.1: The periodic table with relevant elements labelled. The outcrop from the main table are the lanthanides and actinides. The rare earths are marked in red.

In this thesis, the long lifetimes and narrow linewidths are used to control the refractive index of the material through *spectral tailoring*, wherein narrow optical absorption structures are constructed by frequency-selective excitation of certain groups of rare-earth ions.

### 4.1.1 $Y_2SiO_5$ as a host

The host material used in this work is yttrium orthosilicate, $Y_2SiO_5$, often abbreviated YSO. The molecule and the unit cell – formed out of eight molecules – are illustrated in fig. 4.2a. Each Y atom is placed in one of two distinct sites in the unit cell, labelled site I and II. It is not settled which of the two sites corresponds to which specific position in the molecule, though Ref. [32] (Appendix F) makes a good case for the way they are labeled in fig. 4.2a. It makes little difference to this application, however, the sites are optically distinguishable, giving rise to separated absorption profiles.

There are two commonly used coordinate systems, one being the unit cell axes $a$, $b$, $c$, and the other being the orthogonal principal symmetry axes $D_1$, $D_2$, $C_2$. As shown in fig. 4.2b, $C_2$ and $b$ coincide, and are therefore both labelled $b$. For the optical properties, it is the latter coordinate system that matters. $Y_2SiO_5$ is biaxially birefringent, showing a refractive index 1.782, 1.806 and 1.785 with polarization parallel to $D_1$, $D_2$, and $b$ respectively at 633 nm [33].

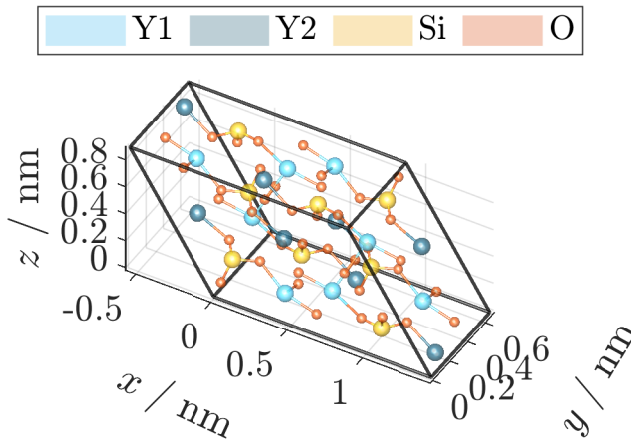


(a) Unit cell of the yttrium orthosilicate crystal. The two distinct sites for yttrium are marked `Y1` and `Y2` respectively. The assignment of the sites is a best guess based on crystal field splittings, but sources disagree. Ions are connected by lines to distinguish the eight molecules in the unit cell, these lines hold no other significance. Figure generated using coordinates from Ref. [34].

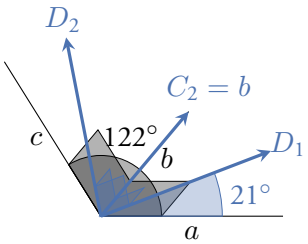


(b) Unit cell axes $a$, $b$, $c$ and symmetry axes $D_1$, $D_2$, $C_2$. $a$ and $c$ are orthogonal to $b$, and are separated by an angle 122°. $D_1$, $D_2$ and $C_2$ are orthogonal to each other. $C_2$ is parallel to $b$. $D_1$ lies 21° from $a$ in the $ac$ plane.

Figure 4.2: The host material, $Y_2SiO_5$.

### 4.1.2 Praseodymium

One promising dopant candidate for quantum information applications is praseodymium, $Pr^{3+}$. Thanks to a long coherence time and narrow homogeneous linewidth, as well as a large oscillator strength leading to large absorption, this ion is interesting as a platform for quantum information storage [35, 36]. For this reason, the community including the quantum information group in Lund has been working with this material for decades. When slow light frequency stabilization was proposed, it was therefore natural for us to begin our investigations in this material. The methods for spectral tailoring in praseodymium had already been developed, and the group possessed some expertise in working with it. Not to mention already owning a crystal of appropriate composition and dimensions.



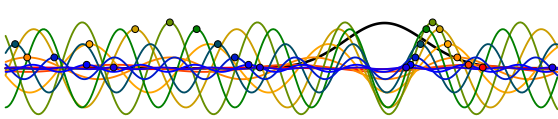

### 4.1.3 Europium

The dopant primarily used for this thesis is europium, $Eu^{3+}$. It is better for the slow light stabilization scheme for a couple of reasons. One advantage is the narrow homogeneous linewidth, measured to be $\Gamma_h \approx 400\,\mathrm{Hz}$ in our crystal, which allows for narrower and sharper spectral features than can be created in praseodymium. Another advantage is the long hyperfine lifetimes, where spectral holes have been observed to remain for up to 50 days [37]. This long lifetime means the same spectral structure can be studied in a longer experiment without deteriorating, and more importantly that the slow light frequency stabilization scheme is not limited by passive drift, as will be discussed in chapter 5. The main drawback of europium compared to praseodymium is a much smaller electric dipole moment, leading to lower absorption. Europium naturally occurs in two isotopes, $^{151}$Eu and $^{153}$Eu, which are roughly equally abundant.

## 4.2 Spectral tailoring

Our primary tool for manipulating these ions is spectral tailoring. To demonstrate how this works, I first propose the simpler case of an ion with two hyperfine ground states, $|1\rangle$ and $|2\rangle$, and a single excited state $|e\rangle$, illustrated in fig. 4.3. If the ion is in $|1\rangle$, and the $|1\rangle \rightarrow |e\rangle$ transition is driven optically, it is excited to $|e\rangle$. The ion now has a probability to relax to either of the ground states. If it returns to $|1\rangle$, it can once again be excited by a pulse at the same frequency. If it ends up in $|2\rangle$, it is no longer available to absorb at that frequency. In this process of *optical pumping* or *optical hole burning*, the population in either state can be depleted over time through repeated excitation.

Because of inhomogeneous broadening, different ions can be resonant with different transitions at the same frequency. We call these overlapping groups of ions *ion classes*, and fig. 4.4 illustrates how an ion system with two ground states and two excited states can have $2 \times 2 = 4$ classes. This added complexity does not affect the core idea of optical pumping, however. As a frequency region is continuously illuminated, any ions which previously absorbed at that frequency is moved out to absorb somewhere else, and a spectral window is opened where nothing absorbs.

Spectral tailoring is a selective application of optical pumping to control the absorption profile over a frequency range. It is complicated by the fact that real ions have more than two or four ion classes – europium with no external magnetic field, for instance, has three ground states ($|\pm\frac{1}{2}g\rangle$, $|\pm\frac{3}{2}g\rangle$, $|\pm\frac{5}{2}g\rangle$) and three excited states ($|\pm\frac{1}{2}e\rangle$, $|\pm\frac{3}{2}e\rangle$, $|\pm\frac{5}{2}e\rangle$), and the splittings vary between the two isotopes as shown in fig. 4.5, leading to $3 \times 3 \times 2 = 18$ ion classes. In practice, it is necessary to computer simulate the resulting spectrum from any hole burning operation beforehand to identify and mitigate unintended side effects.

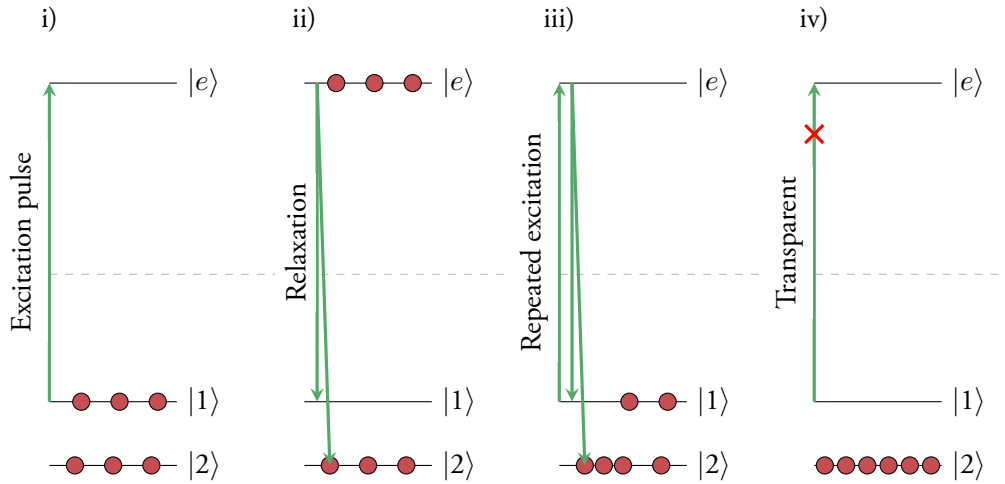


Figure 4.3: Optical pumping in a simplified three-level model. i) Ions are excited from $|1\rangle$ to $|e\rangle$ by an excitation pulse. ii) Ions in $|e\rangle$ rapidly relax into either $|1\rangle$ or $|2\rangle$ with some probability distribution. iii) Ions in $|1\rangle$ are continuously pumped into $|e\rangle$, until … iv) only $|2\rangle$ has any remaining population. The material is now transparent on the $|1\rangle \rightarrow |e\rangle$ transition energy.

A simple method to create a spectral window is to repeatedly scan across the frequency region with a chirped square pulse. The problem with this is twofold: Firstly, a pulse that is square in time has a sinc part to its shape in frequency, in practice widening the pulse and therefore the burned window. The burn pulse will need to be made very long to get the sharp edges we want for strong dispersion. Secondly, the transfer efficiency near the edges of the window will be sensitive to the absolute intensity of the pumping beam. A solution to both these issues comes in the form of *sechyp* and *sechscan* pulses.

### 4.2.1 Sechyp pulses

The complex hyperbolic secant pulse, or *sechyp*, developed originally for nuclear magnetic resonance experiments [40], and later used for quantum information applications [41–43], provides a way to coherently drive a population to full inversion, which is insensitive to absolute intensity. This insensitivity technically requires an ideal implementation, but materializes approximately even in experimental conditions.

The pulse combines a hyperbolic tangent frequency chirp

$$\nu = \nu_c + \mu\beta \tanh(\beta(t - t_0)) \tag{4.1}$$



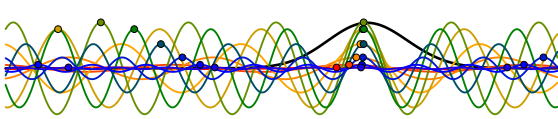

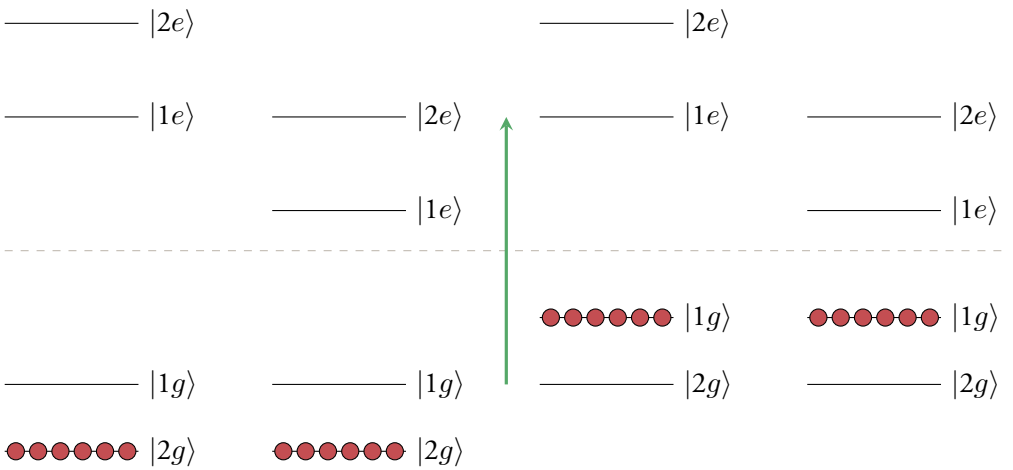


Figure 4.4: All four ion classes of a simple four-level model, pumped until transparent at the marked transition energy.

with a hyperbolic secant intensity envelope

$$\Omega = \Omega_0 \operatorname{sech}(\beta(t - t_0)) \; . \tag{4.2}$$

Here $\beta$ and $\mu$ are pulse parameters related to the desired duration and frequency width of the pulse respectively, $\nu_c$ is the centre frequency of the pulse and $\Omega_0$ is a peak Rabi frequency. The Rabi frequency $\Omega$, proportional to the square root of the intensity, must be above a certain threshold to invert the structure, but beyond this threshold changes in intensity will have no measurable effect on transfer efficiency.

### 4.2.2 Sechscan pulses

A development of the sechyp pulse is the *sechscan* pulse, introduced as *Hyperbolic, Square, Hyperbolic* (HSH) by Ref. [44]. The idea is to extend the effective frequency width of a sechyp pulse while keeping the required bandwidth low. This is accomplished by inserting a linear-chirp square pulse of duration $T$ between the halves of the sechyp pulse,

$$\nu = \begin{cases} \nu_c - \mu\beta^2 \frac{T}{2} + \mu\beta \tanh(\beta t) & t \leq 0 \\ \nu_c + \mu\beta^2 \left(t - \frac{T}{2}\right) & 0 < t \leq T \\ \nu_c + \mu\beta^2 \frac{T}{2} + \mu\beta \tanh(\beta(t - T)) & T < t \end{cases} \tag{4.3}$$

$$\Omega = \begin{cases} \Omega_0 \operatorname{sech}(\beta t) & t \leq 0 \\ \Omega_0 & 0 < t \leq T \\ \Omega_0 \operatorname{sech}(\beta(t - T)) & T < t \end{cases} \tag{4.4}$$

A certain amount of fine-tuning comes into deciding which parameters, how many pulses and what repetition rate should be used to get optimal tailoring. Especially for large crystals, where the absorption from ions in their initial state means that very little power reaches all the way to the end, it can take many pulses to burn all the way through the crystal.



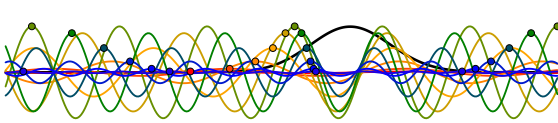

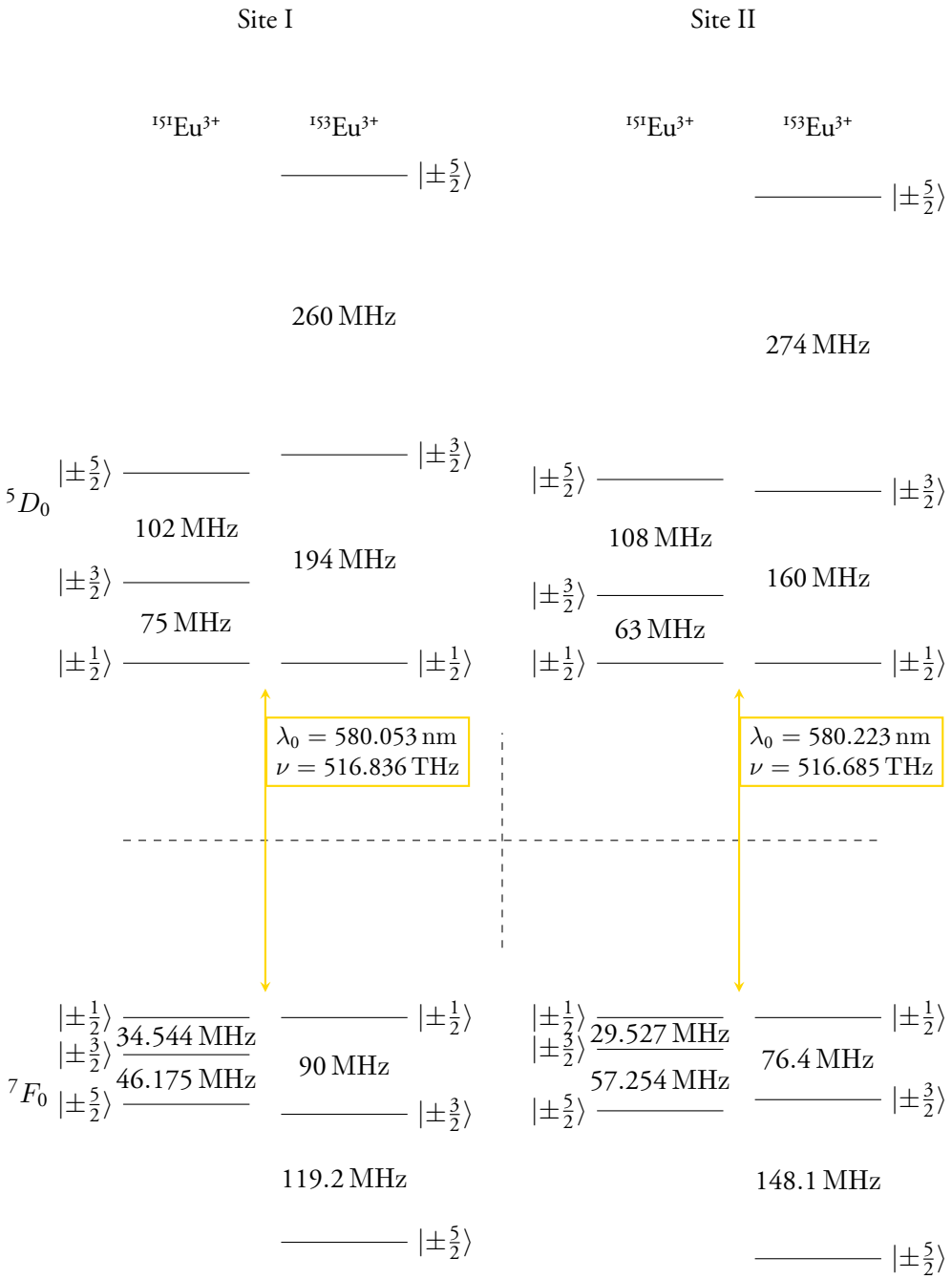


Figure 4.5: Optical and hyperfine energy transitions in both isotopes and both sites of Eu:YSO. Numbers from Ref. [38, 39]. The vertical scale has been truncated, as the optical transition frequency is much larger than the hyperfine splittings.

# Chapter 5

# Slow light frequency stabilization

We arrive, finally, at the heart of the thesis. In this chapter I will discuss the experiments that went into (mainly) papers I and II, the equipment and techniques we developed for these experiments, and some of the results.

## 5.1 Our crystals

Our experiments were primarily performed in two slow light enabled cavities, one doped with praseodymium and one doped with europium. In this section they will be described in greater detail.

### 5.1.1 Praseodymium crystal

The exploratory experiments (paper I) were performed in a cylindrical $6\,\mathrm{mm} \times 12\,\mathrm{mm}\oslash$ YSO crystal, shown in fig. 5.1, doped to $0.05\,\mathrm{at.}\%$ with praseodymium. The front face of the crystal is split by a chord into a clear disk segment and a region with a $95\,\%$ reflective coating. The back face is split into three regions, an uncoated disk segment opposite that on the front face, one half of the remainder coated $95\,\%$ and the other half coated $99.7\,\%$ reflective. The crystal was polished so the faces were close to parallel, leaving a wedge angle of $41\,\mu\mathrm{rad}$ between the front and back face at the position where these experiments were performed.

In order to facilitate side-burning (section 5.3.4), we cut off a small part of the crystal along a chord using a rock saw, and hand-polished the resulting face until acceptably transparent.



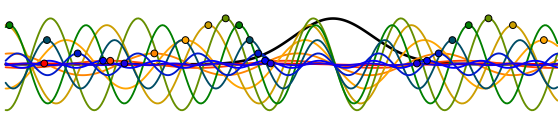

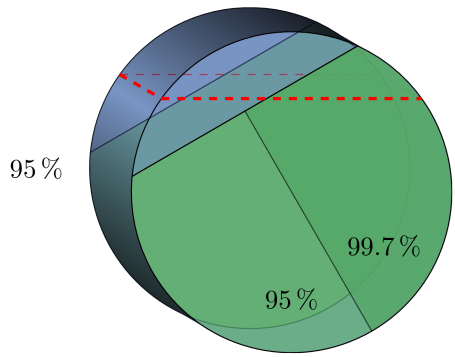


(a) A sketch of the crystal, viewed from the back face. Reflective coated faces marked green, and transparent regions blue. The back face is split into a high reflectivity and a lower reflectivity region. For side burning, the crystal was sawed off along the red dashed line, leaving some of each region intact.

(b) A photograph of the crystal in its final shape, viewed from the front face.

Figure 5.1: The $Pr^{3+}$:$Y_2SiO_5$ crystal used in paper I.

### 5.1.2 Europium crystal

In 2019, work began on growing a crystal boule of YSO doped with 1 at.% europium ions in natural abundance – about 50 % each of $^{151}$Eu and $^{153}$Eu. The crystal for this project cut from this boule is quite large for this type of sample, at 14 mm by 15 mm by 21 mm, aligned with $b \times D_1 \times D_2$, shown in fig. 5.2. The crystal was grown by Scientific Materials in the US, using the Czochralski method.

Once grown, the crystal was mechanically polished by Edmund Optics in the US which achieved a 7.9 µrad parallelism (large-scale length variation), followed by ion beam forming to reduce surface roughness and further increase parallelism to 1.37 µrad by Neue Technologien in Germany. Finally, the front face of the crystal was coated by ion beam sputtering to 90 % reflectivity and the back to 99 % by Optoman in Lithuania.

The choice of these properties – the dopant concentration, the axis alignment, the physical dimensions, the parallelism and surface roughness, and the reflectivity – was a multidimensional and iterative problem which took us a long time and hard work to figure out. Follows a breakdown of this process.

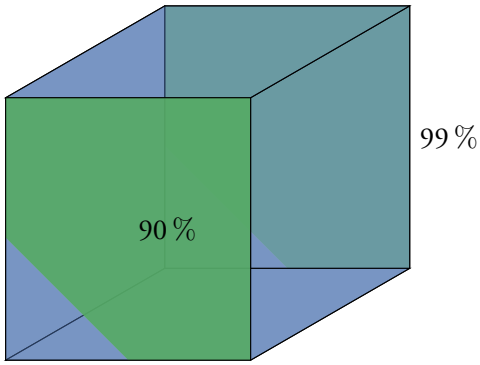


(a) Sketch of the crystal.

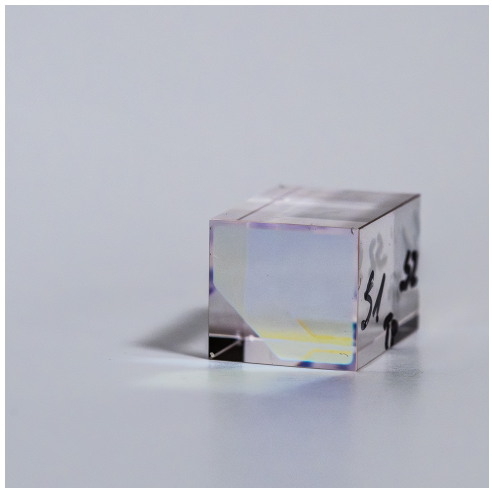

(b) Photograph of the crystal.

Figure 5.2: The $Eu^{3+}$:$Y_2SiO_5$ crystal used in papers II, IV, and V.

When choosing a dopant concentration, our main concern was inhomogeneous linewidth, $\Gamma_i$, which scales linearly with dopant concentration [45]. I will discuss in section 5.2.5 the necessity to have a cavity mode near the peak of the inhomogeneous profile, but the worst case scenario is that the distance from the peak is half a free spectral range, or about 2 GHz. Given the 22 GHz wide Lorentzian profile reported in Ref. [45] for 1 at.% concentration, this means a drop in absorption of about 3 %, which we deemed acceptable. In hindsight, the increased hyperfine linewidth resulting from a large dopant concentration caused some trouble when developing our RF erasure method (section 5.3.5), and it might have been worth the trade-off to pick a lower concentration and risk a lower absorption.

For slow light frequency stabilization we want to maximize the dispersion, and therefore the absorption outside the spectral window. For site I in 1 at.% $Eu^{3+}$:$Y_2SiO_5$, Ref. [45] cites the maximum absorption coefficient as $\alpha_{D_1} = 390\,\mathrm{m}^{-1}$ with the polarization along $D_1$, $\alpha_{D_2} = 80\,\mathrm{m}^{-1}$ along $D_2$ and $\alpha_b = 0\,\mathrm{m}^{-1}$ along $b$. We therefore knew we needed the $D_1$ axis parallel to the mirror faces to maximize absorption. This still leaves one degree of freedom, which we could use to reduce the frequency noise due to variation in polarization: If the absorption in the orthogonal polarization direction was comparable to the absorption in the one we intended to use for locking, it would also experience the slow light effect. This would in turn reduce the linewidth and free spectral range of the modes along this direction, and any uncertainty or variation in polarization could then cause noise from light coupling to modes in both polarizations. Choosing to turn $b$ parallel to the mirror face, the linewidth and free spectral range of the orthogonal polarization are maximized, minimizing this frequency-polarization noise coupling. Additionally, as will be discussed



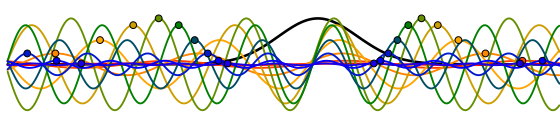

in section 5.3.4 the spectral tailoring light we illuminated the crystal with from the side would be unpolarized, and so by having two absorbing polarization axes parallel to the burner face, the burning efficiency is somewhat increased.

A long cavity length is generally good for frequency reference cavities, as discussed in chapter 2. In the slow light stabilization scheme it also increases the interaction volume, which reduces intensity dependent drift. We also wanted a large crystal face because we wanted to be able to lock using a large area beam in order to reduce the locking beam intensity, and have the option to use more than one beam at the same time.

What we ended up with for the physical dimensions was limited by two things primarily: The size of the sample chamber of our new cryostat, which had at that point not yet arrived, and the size the growers could realistically extract from a boule without including imperfections. The asymmetry in the front face dimensions was just a way to easily orient the crystal with respect to its optical axes.

In order to minimize intensity-induced drift (expanded on in section 5.2.3), we want to probe as many of our ions as possible at once, which means using a large mode volume. For this purpose, we wanted flat, parallel mirrors, so that we could couple a wide beam with flat wavefronts to it. Apart from the reduced intensity from an increased beam radius, an additional benefit is that the Brownian length uncertainty is averaged down, scaling with the beam radius [21].

Parallelism and surface roughness refer to large and small scale variations in cavity length respectively. Parallelism means the path length through one side of the crystal is longer than through the other side, and that the path length varies across the width of the probing beam. The main effect of an error in parallelism is to widen the cavity mode, so we wanted a degree of parallelism where the resulting widening was small relative to the expected cavity width.

Surface roughness means variations in length on a small scale, where the main effect is losses through scattering rather than length uncertainty. Roughness is quoted as a length, the root-mean-square deviation, $\sigma_r$, from a flat plane within the area of a probing beam. Surface roughness causes a round-trip scattering loss $\beta$, so that the intensity of light is multiplied by a factor $\exp(-\beta)$ every round trip through the crystal, given by

$$\beta = 2\left(\frac{4\pi\sigma_r}{\lambda}\right)^2 \tag{5.1}$$

with RMS surface roughness $\sigma_r$ and wavelength $\lambda$ [46]. Again, we wanted this factor to not be limiting, meaning it should be small relative to the centre-of-window residual absorption $2\alpha_c L$. Once more, these requirements were on the edge of what processing companies were prepared to quote us for, especially since to many of them $Y_2SiO_5$ was an unfamiliar material.

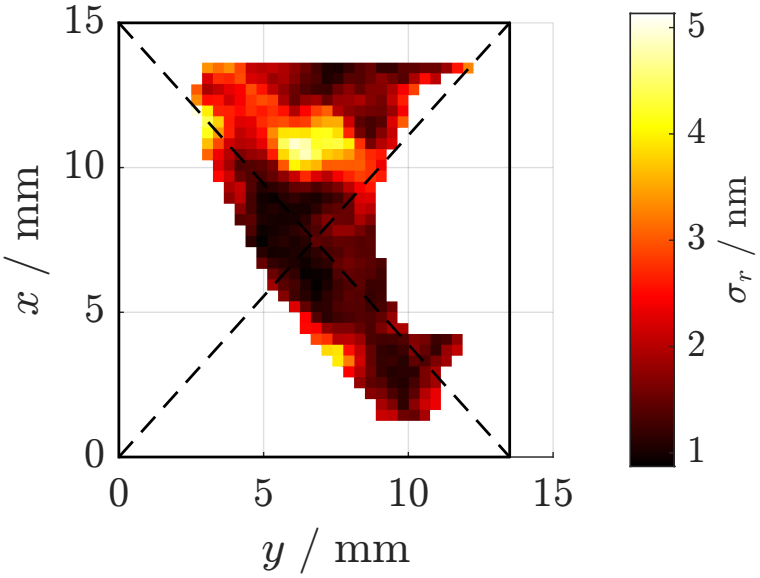


Figure 5.3: Approximate surface roughness over 1.5 mm circular regions on the face of the europium crystal. Lower is better. The black rectangle is an approximate outline of the entire crystal face, and the dashed lines are guides to find one's position relative to the centre. The white regions lie beyond discontinuities or missing data.

In order to measure the parallelism and surface roughness, the ion beam forming company performed white-light interferometry. The distance from a known flat reference surface to the surface under investigation was measured using interference fringes from a white light source. In this process, they discovered that the result was different depending on whether the surfaces were measured in direct reflectivity or through the crystal. The conclusion was that there was some refractive index inhomogeneity in the crystal, which meant there was a conflict between making the cavity *optically* flat, versus making each mirror separately flat. Because we primarily intend this crystal to be probed as a cavity, we made the decision to make what would become the high-reflectivity face absolutely flat, and then form the low-reflectivity face so that the cavity was optically flat. Figure 5.3 shows the root-mean-square length variation within a 1.5 mm disk around coordinates on the crystal. From this figure, we conclude that there are certain spots where the total surface roughness across such a beam is around 1 nm. This corresponds to a loss factor $\beta = 13 \cdot 10^{-3}$ (eq. (5.1)), two orders of magnitude lower than the expected round-trip centre-of-window absorption for our typical window widths. This means mirror scattering is unlikely to have an impact on locking performance in those spots. To judge the impact of the parallelism, we can consider two small spots on each side of a 1.5 mm diameter beam. 1.37 µrad means that the length of the cavity varies by $\Delta L = 1.37\,\mu\text{rad} \cdot 1.5\,\text{mm} = 0.2\,\text{nm}$ over the beam. The resonance frequency at each spot will differ by $\nu_0 \Delta L/L = 49\,\text{MHz}$ (without dispersion). This can



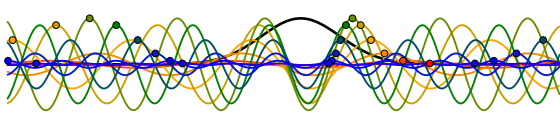

be considered an estimate of wedge angle mode widening, and should ideally be a small portion of the total cavity linewidth.

With these parameters nailed down there was one main choice left to be made for the design of the cavity itself: Mirror reflectivities. For this choice, there is a bit of a trade-off between long- and short-term stability of the lock. Higher reflectivity leads to narrower cavity modes which means better short-term stability, but higher intra-cavity power which increases power-induced drift (section 5.2.3). The back mirror reflectivity in principle determines the cavity linewidth (eq. (2.1)), but because the total cavity losses were likely to be dominated by absorption, we determined that there was no reason to make this value extreme, so we chose 99 %. As discussed in section 5.3.1, the impedance matching criterion links the front mirror reflectivity to the window width, in that the absorption in the middle of the window times the back mirror transmission should equal the front mirror transmission, leading to minimum reflectivity and maximum transmission at resonance.

In order to finally make a choice of front mirror reflectivity, I calculated the group refractive index and estimated a locking time for a number of window widths, using the method in paper I, Appendix E, and chose a pair that represented a good compromise between long- and short-term stability. If we pick a large window width, the off-resonant excitation is decreased which lowers the rate by which we expect the window to degrade. This maximizes the long term stability. But a wider window also leads to a lesser slow light effect, which decreases the short-term stability. In the end, we elected to pick a reflectivity of 90 %, which corresponds to a window width of 40 kHz. This is the region where the previously discussed wedge angle mode widening starts to become a substantial part of the cavity linewidth, impacting short-term stability.

## 5.2 Properties of the slow light stabilization scheme

Having introduced the crystals used for the slow light stabilization scheme, in this section I will discuss the properties of the scheme, theoretically derived as well as measured experimentally. I will discuss and derive the sensitivity of the cavity mode frequency to variations in cavity length and angle of incidence. Then I will walk through the main sources of long term drift and the frequency stability of the locking scheme.

### 5.2.1 Length insensitivity

The limiting factor to state-of-the-art laser frequency stabilization is cavity length uncertainty due to Brownian motion in the cavity mirrors. The overarching idea of slow light stabilization is to use strong dispersion to reduce the length sensitivity of the resonance

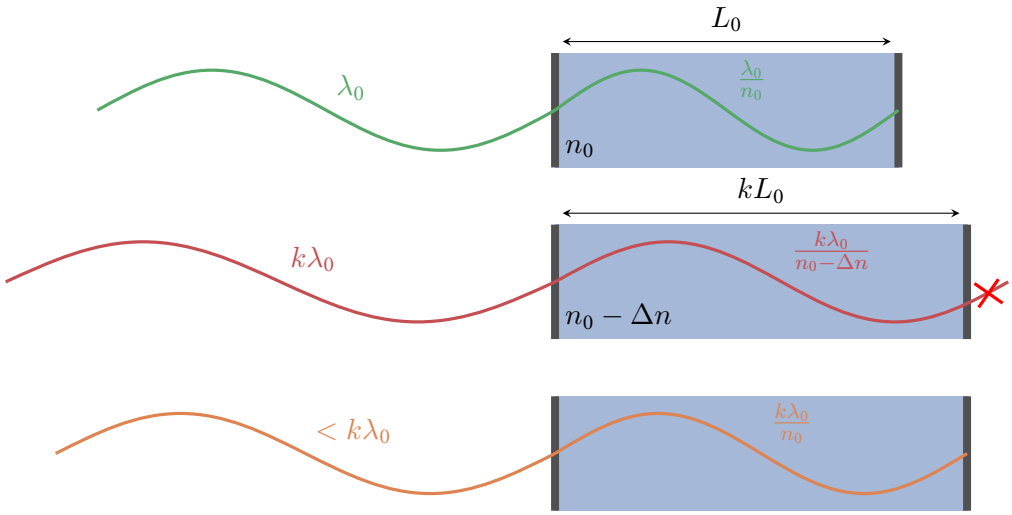


Figure 5.4: Wave stretching heuristic of slow light length insensitivity. A wave on resonance with a cavity of length $L_0$ (top) fits a whole number of wavelengths between the mirrors. If the cavity gets a factor $k$ longer, the wavelength could stretch by the same factor (middle). Because of dispersion, the wavelength inside the cavity is extended *more* than a factor $k$, and the light is no longer on resonance. Somewhere in-between these two wavelengths (bottom), there is one where the dispersion and length change cancel out – meaning that the necessary wavelength response to stay on resonance is reduced by dispersion. Length and colour changes exaggerated for illustration purposes.

frequency – the amount the resonance frequency changes for a given change in length. Heuristically, the insensitivity can be thought of as an artificial increase of the cavity length. Pulses travel through the cavity with a group velocity $v_g = c_0/n_g$, so each trip through the cavity takes a factor $n_g/n_0$ longer time, just as if the cavity was that much longer. This explanation is intuitive but somewhat unsatisfying, given that frequency stabilization is implemented using continuous-wave light, not pulsed. Another heuristic is to consider the wavelength of light on resonance with the cavity, as the cavity length varies, as illustrated in fig. 5.4. If the cavity becomes a factor $k$ longer, the wavelength could "stretch" by $k$ to maintain the same number of wavelengths in the cavity. But thanks to dispersion, the refractive index at this new wavelength is lower, meaning that the in-material wavelength stretches by *more* than $k$, and we overshoot the target. The required change in vacuum wavelength is that much smaller than the relative length change. This second heuristic is closer to the way the effect is utilized, but requires us to imbue the light wave with an unfortunate amount of agency and intention.

The effect of dispersion on frequency changes due to length changes is derived more stringently below, but it predicts the same behaviour as each of these pictures, namely that



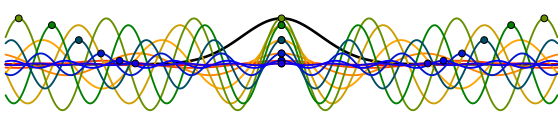

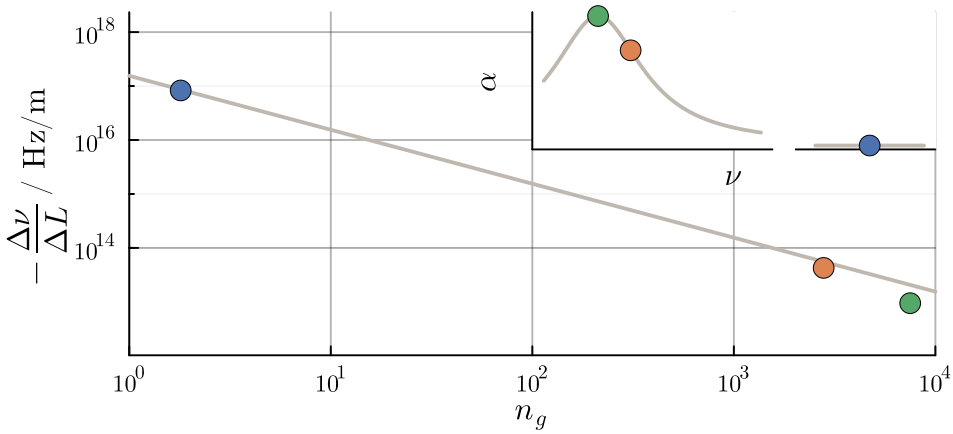


Figure 5.5: Length sensitivity of a praseodymium cavity, adapted from data reported in paper I. The straight line is the predicted sensitivity in eq. (5.2). Inset: The inhomogeneous profile of praseodymium, and the points along it where the data was taken. The break in the horizontal axis signifies a large frequency shift, as this data was captured far off the absorption line, with no spectral window.

changes in length by a factor $\Delta L/L_0$ translate into frequency changes

$$\Delta\nu = -\frac{n_0}{n_g}\frac{\Delta L}{L_0}\nu_0 \,, \tag{5.2}$$

where $\nu_0$ is the original frequency, $n_0$ is the host refractive index and $n_g$ is the group refractive index.

In paper I, we confirmed this length insensitivity by translating the probing beam across the face of our praseodymium crystal and measuring the resonance frequency. Because the crystal has a 40 µrad wedge angle, a translation corresponds to a predictable change in cavity length. This experiment was performed at two different points on the inhomogeneous profile, as well as one far off the profile, giving three different values of the dispersion coefficient. The results of this experiment are illustrated in fig. 5.5, and the data matches eq. (5.2) well. If anything, the sensitivity was reduced more than expected, a discrepancy we attributed to potentially imperfectly tailored windows.

**Derivation**

To derive the length sensitivity mathematically, I consider the phase addition $\phi$ of a wave with frequency $\nu$ travelling a distance $z$ through a crystal with refractive index $n$:

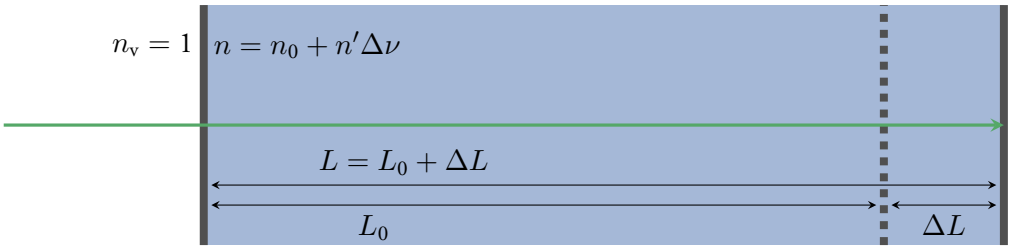


Figure 5.6: Geometric definitions for the derivation of length sensitivity.

$$\phi(z,\, n,\, \nu) = \frac{2\pi}{c_0} n\nu z \tag{5.3}$$

Assuming normal incidence ($z = L$), illustrated in fig. 5.6, I search for frequencies $\nu$ such that the phase remains constant with changing cavity length, that is

$$\phi(L_0,\, n_0,\, \nu_0) = \phi(L,\, n,\, \nu) \Longrightarrow \frac{2\pi}{c_0} n_0\nu_0 L_0 = \frac{2\pi}{c_0} n\nu L \,. \tag{5.4}$$

I introduce a (small) length change $\Delta L$:

$$L = L_0 + \Delta L \,, \tag{5.5}$$

a corresponding frequency change

$$\nu = \nu_0 + \Delta\nu \,, \tag{5.6}$$

and linear dispersion, with a dispersion coefficient $n'$:

$$n = n_0 + \frac{\mathrm{d}n}{\mathrm{d}\nu}(\nu - \nu_0) = n_0 + n'\Delta\nu \,. \tag{5.7}$$

Combining eqs. (5.4) to (5.7) gives

$$\frac{\nu_0 + \Delta\nu}{\nu_0} \frac{n_0 + n'\Delta\nu}{n_0} \frac{L_0 + \Delta L}{L_0} = 1 \,, \tag{5.8}$$

which can be simplified to

$$\left(1 + \frac{\Delta\nu}{\nu_0}\right)\left(1 + \frac{\Delta L}{L_0}\right)\left(1 + \frac{n'\Delta\nu}{n_0}\right) = 1 \,. \tag{5.9}$$

Expanding the product and collecting $\Delta\nu$,

$$\left(1 + \frac{\Delta\nu}{\nu_0} + \frac{n'\Delta\nu}{n_0} + \frac{n'\Delta\nu^2}{n_0\nu_0}\right) = \left(1 + \frac{\Delta L}{L_0}\right)^{-1} \tag{5.10}$$



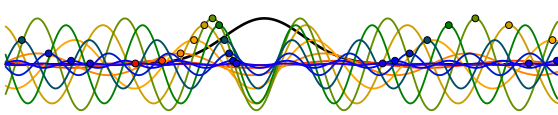

If $\Delta\nu/\nu_0$, $n'\Delta\nu/n_0$, and $\Delta L/L_0$ are all $\ll 1$, the second degree term is negligible and I can use the first degree Taylor expansion $(1+x)^{-1} \approx 1 - x$ to get

$$\frac{\Delta\nu}{\nu_0}\left(1 + \frac{n'\nu_0}{n_0}\right) \approx -\frac{\Delta L}{L_0} \,. \tag{5.11}$$

Therefore,

$$\frac{\Delta\nu}{\nu_0} \approx -\frac{n_0}{n_0 + n'\nu_0}\frac{\Delta L}{L_0} = -\frac{n_0}{n_g}\frac{\Delta L}{L_0} \,, \tag{5.12}$$

with group refractive index $n_g = n_0 + n'\nu_0$, which is the expression I was looking for.

As a sanity check, I test the case of zero dispersion. If $n' = 0$,

$$\frac{\Delta\nu}{\nu_0} = -\frac{\Delta L}{L_0} \,, \tag{5.13}$$

which is unsurprisingly the normal response to cavity length changes. This is equivalent to the wavelength stretching by the same proportion as the cavity length.

### 5.2.2 Angle insensitivity

As previously described, we want a large beam with flat wavefronts for locking, in order to reduce the intensity induced drift, and this means that our cavity needs flat mirrors. Flat mirror cavities are not normally used for laser frequency stabilization, as they have degenerate transversal modes. This means the mode frequency $\nu$ will vary continuously with incidence angle $\theta$ as

$$\nu = \nu_0 \left(\sqrt{1 - \frac{\sin^2\theta}{n^2}}\right)^{-1} \,. \tag{5.14}$$

Here I have adjusted the usual expression for off-axis transmission for a Fabry-Perót cavity [19, eq. 10.1-37] to include a cavity refractive index $n$ via Snell's law and the Pythagorean identity. For comparison, from the testing data of Thorlabs' Polaris mounts [47], I estimate that their pointing angle varies on the order of $5\,\mu\mathrm{rad}$ as the temperature varies by $1\,^\circ\mathrm{C}$ around room temperature. This tiny fluctuation alone, inserted into eq. (5.14), would translate into a frequency shift of 2 kHz, not to mention other angle fluctuations like those from mechanical vibrations.

In order for this scheme to be feasible, we need to show that the slow light effect helps in this regard, that the angle sensitivity is reduced with large dispersion. As derived below, the frequency shift $\Delta\nu$ for a given incidence angle $\theta$ indeed comes out to

$$\Delta\nu = \frac{n_0}{n_g}\frac{\sin^2\theta}{2n_0^2}\nu_0 \tag{5.15}$$

with host refractive index $n_0$ and group refractive index $n_g$. To compare to the case with no dispersion, eq. (5.14) can be rewritten for small $\theta$, with $\nu = \nu_0 + \Delta\nu$ and $n = n_0$, and using the taylor expansion $\left(\sqrt{1-x}\right)^{-1} \approx 1 + x/2$

$$\Delta\nu = \nu_0 \left(1 + \frac{\sin^2\theta}{2n_0^2}\right) - \nu_0 = \frac{\sin^2\theta}{2n_0^2}\nu_0 \ . \tag{5.16}$$

Just like with length changes, the addition of dispersion causes the sensitivity to reduce by a factor $n_0/n_g$! This is why locking to a flat cavity is feasible using the slow light effect, while it is impractical without it.

As a verification of this result, I used a wave propagation simulator developed by Adam Kinos (described in Ref. [48]) to calculate the transmission through a slab at various frequencies and various angles numerically. The simulator is given only the absorption profile of the crystal, that is either complete transmission or a square spectral transparency window as shown in fig. 3.1b, a cavity length and a pair of mirror reflectivities. It then simulates plane waves in a range of frequencies propagating through this structure at angles between 0 µrad and 200 µrad, and registers the total reflected intensity. The result of the simulations is shown in fig. 5.7, together with the theoretical predictions in eq. (5.14) and eq. (5.15). It is clear that, for these angles, the numerical result of adding up complex valued waves matches the theoretical prediction. An experimental verification was planned, but never came to fruition because of practical issues.

### Derivation

In analogy with the derivation for length insensitivity, I use the expression for the phase addition through the cavity in eq. (5.3), but this time with constant length $L$, an incident angle $\theta$, and an angle of refraction $\beta$, as illustrated in fig. 5.8.

I introduce a small $\theta$, and through Snell's law, $n_v \sin(\theta) = n \sin\beta$, and the Pythagorean identity, $\sin^2\beta + \cos^2\beta = 1$,

$$z = L\cos\beta = L\sqrt{1 - \frac{\sin^2\theta}{n^2}} \ . \tag{5.17}$$

Like before, I use the corresponding frequency change

$$\nu = \nu_0 + \Delta\nu \ , \tag{5.18}$$

and linear dispersion

$$n = n_0 + n'\Delta\nu \ . \tag{5.19}$$



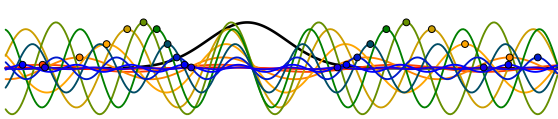

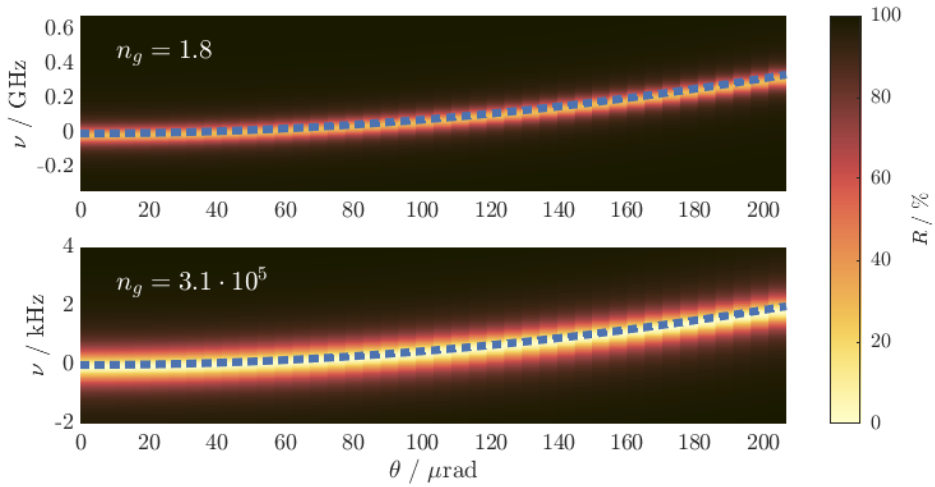


Figure 5.7: Numerical simulation of cavity reflection at various angles of incidence, in a cavity without slow light effect (top) and with slow light effect (below). Note the difference in scale between the vertical axes: The sensitivity to angle changes is reduced by more than five orders of magnitude in the lower plot.

To have no change in phase, I set

$$\phi(L) = \phi(L\cos\beta)\ , \tag{5.20}$$

and combining eqs. (5.17) to (5.20) gives

$$\frac{2\pi}{c_0} n_0 \nu_0 L = \frac{2\pi}{c_0}(n_0 + n'\Delta\nu)(\nu_0 + \Delta\nu)\left(L\sqrt{1 - \frac{1}{(n_0 + n'\Delta\nu)^2}\sin^2\theta}\right)\ . \tag{5.21}$$

I divide both sides by the left-hand side,

$$\left(1 + \frac{n'\Delta\nu}{n_0}\right)\left(1 + \frac{\Delta\nu}{\nu_0}\right)\sqrt{1 - \frac{\sin^2\theta}{(n_0 + n'\Delta\nu)^2}} = 1\ . \tag{5.22}$$

For small $\theta$ and $n \geq 1$, the Taylor expansion $\sqrt{1-x} \approx 1 - \frac{x}{2}$ gives

$$\left(1 + \frac{n'\Delta\nu}{n_0}\right)\left(1 + \frac{\Delta\nu}{\nu_0}\right)\left(1 - \frac{\sin^2\theta}{2\,(n_0 + n'\Delta\nu)^2}\right) = 1\ . \tag{5.23}$$

Ignoring the higher order terms like before,

$$\left(\frac{n'\nu_0}{n_0} + 1\right)\frac{\Delta\nu}{\nu_0} = \frac{\sin^2\theta}{2n_0^2}\ , \tag{5.24}$$

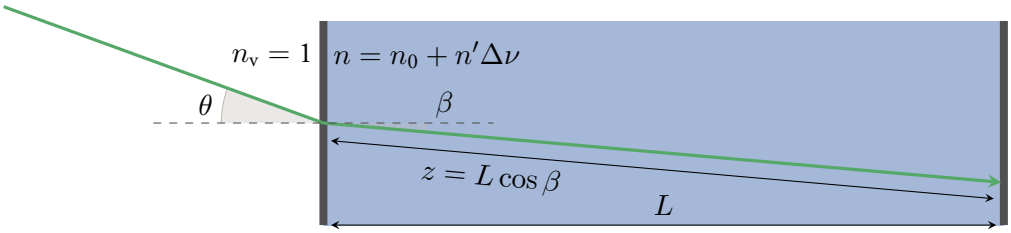


Figure 5.8: Geometric definitions for the derivation of angle sensitivity.

and finally

$$\frac{\Delta\nu}{\nu_0} = \frac{n_0}{(n_0 + n'\nu_0)}\frac{\sin^2\theta}{2n_0^2} = \frac{n_0}{n_g}\frac{\sin^2\theta}{2n_0^2} \tag{5.25}$$

with group refractive index $n_g = n_0 + n'\nu_0$, just as expected.

### 5.2.3 Drift

In paper I, we demonstrated two main sources of long-term drift in praseodymium slow light-enhanced cavities, both causing deterioration of the spectral structure: A constant drift rate due to asymmetric hyperfine cross-relaxation, and a power and locking-frequency-dependent drift due to off-resonant excitation of ions outside the window.

#### Hyperfine cross-relaxation

In rare-earth metal ions, the lifetime of the hyperfine transitions in the ground state are comparatively long, but they are not infinite. After a spectral transparency window has been prepared, the ions that were pumped away have a finite probability per unit time to relax into their original state, figuratively filling up the window. Because the composition of ion classes can vary over the window, this process may be asymmetric. The total effect is a constant deterioration, and potentially a constant frequency drift.

Changing material from praseodymium to europium was largely motivated by this effect, as the lifetime of spectral structures are on the order of minutes in praseodymium [49], but weeks in europium [37]. This factor 20 000 increase practically eliminates hyperfine cross-relaxation as a concern.



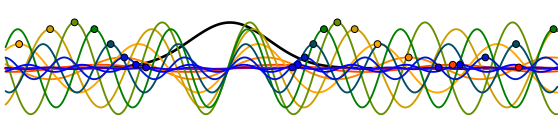

**Off-resonant excitation**

The homogeneous profile of individual ions is Lorentzian [50, Chapter 3], and as illustrated in fig. 3.1, this means the ions near the edges of a spectral transparency window are weakly absorbing inside the window. As we lock a laser to a cavity mode inside the window, it will cause a certain rate of excitation in the ions that make up the edges, effectively pumping those ions away. The effect is a gradual widening of the window, reducing the slow light effect. The closer the mode we lock to is to a window edge, the faster this deterioration happens. In addition, a mode closer to one edge than the other will cause a first-order drift in that direction, while off-resonant excitation from a perfectly centred mode-lock widens the window symmetrically. For these reasons, it would be advantageous to be able to control the mode frequencies relative to the centre frequency of the window. Section 5.2.5 dives into the method by which we do this.

The other contributing factor to the off-resonant excitation drift rate is, of course, locking intensity. In paper I, we demonstrated a linear relation between locking intensity and drift rate, up to a limit. The off-resonant excitation drift rate can therefore be reduced by increasing the beam area, as discussed in section 5.1.2, and by using the minimum necessary locking power.

In paper II, the total drift for a lock onto a mode 2 kHz from the centre of a 40 kHz wide window in europium was $3.66\,\mathrm{Hz\,s^{-1}}$, compared to the $550\,\mathrm{Hz\,s^{-1}}$ minimum measured in praseodymium in paper I. We expect to be able to achieve much lower drift than this, by centring the modes better.

The best centred mode we managed to get a good lock to in our first experimental run was 2 kHz from the centre of the window. The reason we could not get closer to 0 kHz was lack of time – this was the last lock established during the last hours of a long lab run. With some experimental tweaks, we should be able to move the window to any frequency on the inhomogeneous line with kHz precision. As discussed in section 5.2.5 this in principle allows us to place the cavity mode with a few mHz relative precision, in theory reducing the drift from off-resonant excitation by up to six orders of magnitude.

### 5.2.4 Short-term stability

The locking stability can be measured using the Allan deviation. In short, it is a measurement of how much the frequency of your system varies when averaged into bins of some averaging time $\tau$. The Allan deviation is typically reported as a graph and shown for a number of $\tau$'s. The most commonly used variant of the Allan deviation is *overlapping Allan deviation*, where the bins are not disjoint partitions of the dataset, but every data point counts towards several bins. This increases the statistical confidence at the cost of

some computing power. Linear frequency drift is often subtracted before calculating the deviation [51, 52].

Figure 5.9 shows the overlapping Allan deviation with drift subtracted for our locking scheme, both in praseodymium and europium. The goal is to push this curve as low as possible. The record in the literature is $\sigma_y = 8 \cdot 10^{-17}$, realized in a 48 cm long ULE cavity with highly optimized suspension and thermal control [26]. More typical high-performance cavities are around $\sigma_y = 1 \cdot 10^{-15}$. In this context, the number we measured in paper II, $\sigma_y = 6 \cdot 10^{-14}$, is not all that impressive, but it is important to keep in mind that stability will always be measured against some other reference. In order to measure the true stability of a system you will need to know that the instability of your reference is negligible compared to that of your system, or that they are equal.

We believe that in this experiment, the frequency instability of our reference laser, including fibre phase noise, is considerably larger than the actual instability of the slow light cavity, and that we are rather measuring the Allan deviation of the laser-fibre combination. In order to get a more accurate assessment of the slow light cavity's frequency stability, one could either cancel out the fibre noise through active feedback, or compare the frequency of two copies of the same setup. In active fibre noise cancellation, a small portion of the light that passes through the fibre is reflected back and the reflected light's phase is compared to the incident. An acousto-optic modulator can then adjust the phase accordingly, to cancel out any phase addition from the fibre [53–57].

An alternative approach to assess the stability of a frequency reference is to compare the frequency of two separate but similar references, which eliminates common noise sources like reference laser noise. In this project, the plan for the future is to do a variation of this idea, where two separate laser beams will be individually locked to separate spots on the same crystal. With this method several noise sources might be correlated, like vibrations and pressure, but the Brownian noise from the mirrors will be uncorrelated. This will let us assess the stability, without requiring full environmental shielding. We have not yet tried either of these methods, but there are plans for both, and the cavity was specifically designed to allow the two-beam locking setup.

Of note in fig. 5.9 is that the europium experiment displayed an order of magnitude lower deviation than praseodymium in a directly comparable measurement. This improvement can be attributed to the narrower homogeneous linewidth and the longer hyperfine lifetimes in europium.

Between $\tau = 10^{-2}$ s and $10^{-1}$ s, there is some periodic structure. This is indicative of an oscillating frequency, and the oscillation here appears to be around 55 Hz – potentially acoustic noise in the setup, as we have previously seen nearby mechanical oscillations, as discussed in section 5.3.3.



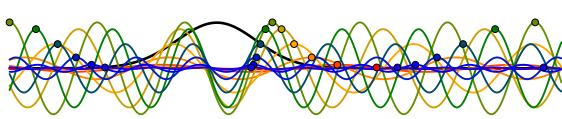

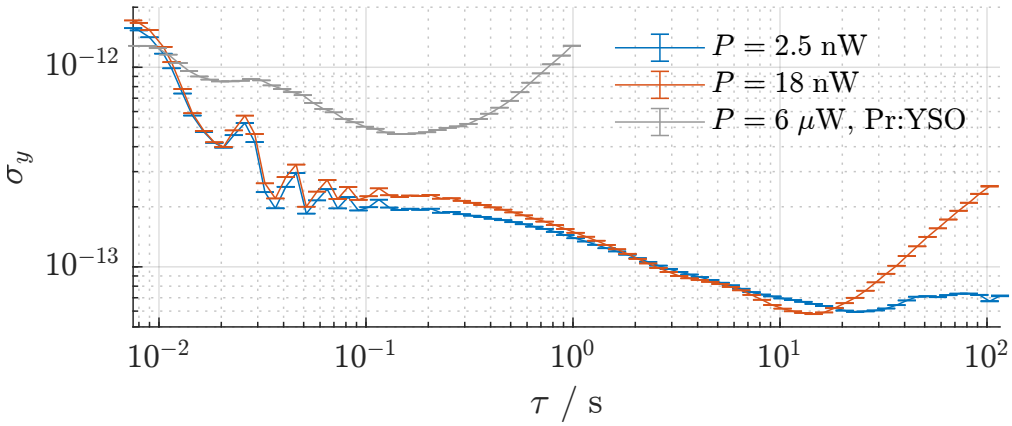


Figure 5.9: The overlapped Allan deviation reported in paper II.

### 5.2.5 Mode frequency control

As discussed in section 5.2.3, an important step to reduce the drift of the slow light cavity is to position the mode near the centre of the window, minimizing off-resonant excitation from ions in either edge.

In paper I, mode positioning was achieved using the wedge angle between the mirror faces of the crystal. By translating the beam on the face of the crystal, the cavity length could be controlled, and with it the mode frequencies. The other side of this coin is, unfortunately, that a wedge angle this large also makes the locking scheme sensitive to variation in locking beam position. For the europium crystal we decided on a much more parallel cavity, and so we required a new method of mode positioning.

The frequency of the cavity modes, $\nu_{\text{mode}}$, relative to the centre frequency of the window, can be controlled by changing the frequency where the window is burned, $\nu_{\text{win}}$, relative to the peak of the inhomogeneous profile (fig. 5.10 shows these definitions visually). The exact relation is derived in paper II, but as a quick rule of thumb, if you have a window with centre frequency $\nu_{\text{win},1}$, and it has a mode at frequency $\nu_{\text{mode},1}$, then erasing the window and burning a new one at $\nu_{\text{win},2} = \nu_{\text{win},1} + \Delta\nu_{\text{win}}$ will give you a mode at $\nu_{\text{mode},2} = \nu_{\text{mode},1} - (n_0/n_g)\Delta\nu_{\text{win}}$. Because of the susceptibility contribution from the inhomogeneous line itself, this approximation is about 10 % off, but it is good enough for iterating in small steps. Importantly for the stabilization scheme, if you can change the frequency one or more free spectral ranges in steps of $\Delta\nu$, then you will be able to place a mode within $n_0\Delta\nu/n_g$ of the zero-drift frequency in the middle of the window.

To verify this method, we burned windows at numerous frequencies $\nu_{\text{win}}$ along the inhomogeneous profile, and measured the mode frequency $\nu_{\text{mode}}$, as shown in fig. 5.11.

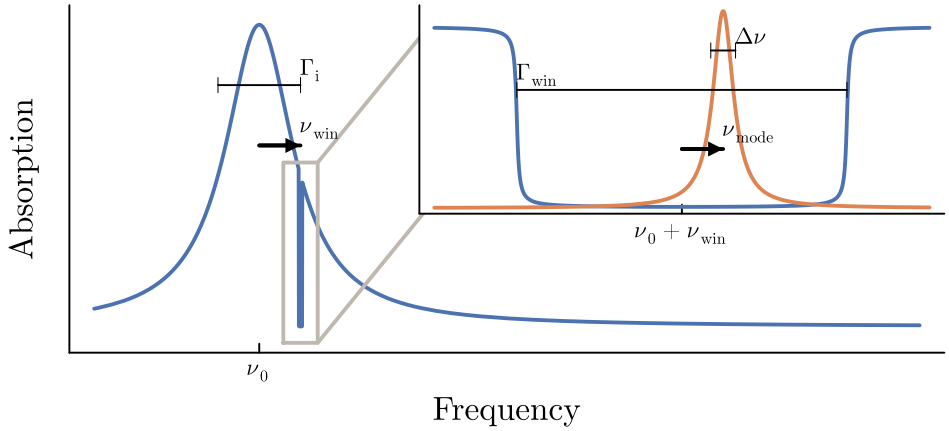


Figure 5.10: A spectral window burned at a frequency $\nu_{win}$ from the centre frequency $\nu_0$ of the inhomogeneous absorption profile. In the inset, the cavity transmission is marked in orange. Not to scale.

## 5.3 Experimental details

In order for this scheme to work, a number of requirements on the cavity and the equipment needed to be fulfilled. In this section, I will go into some of these practical considerations.

### 5.3.1 Impedance matching

As described in section 2.2, in Pound-Drever-Hall stabilization a locking beam is reflected off a cavity and the reflectivity measured. On resonance the cavity reflectivity will be minimal, so any increase in reflectivity is interpreted as a shift in frequency. For optimal locking, it is important to maximize the contrast between signal on resonance with the cavity mode and non-resonance. The maximum contrast for this is when the immediately reflected electric field amplitude from the front mirror is approximately equal to that of the light leaking out of the cavity. That way they can cancel out perfectly upon destructive interference, leading to no total reflected field. In analogy with electrical resonance circuits, this condition of optimal interference is called *impedance matched*.

For a normal cavity with no losses beyond the transmission through the mirrors, the impedance matching criterion simply means that both mirrors should have equal reflectivity. In reality, the intracavity field suffers losses from absorption in the medium and, to some degree, scattering at the surfaces, in addition to the transmission through the mirrors. The

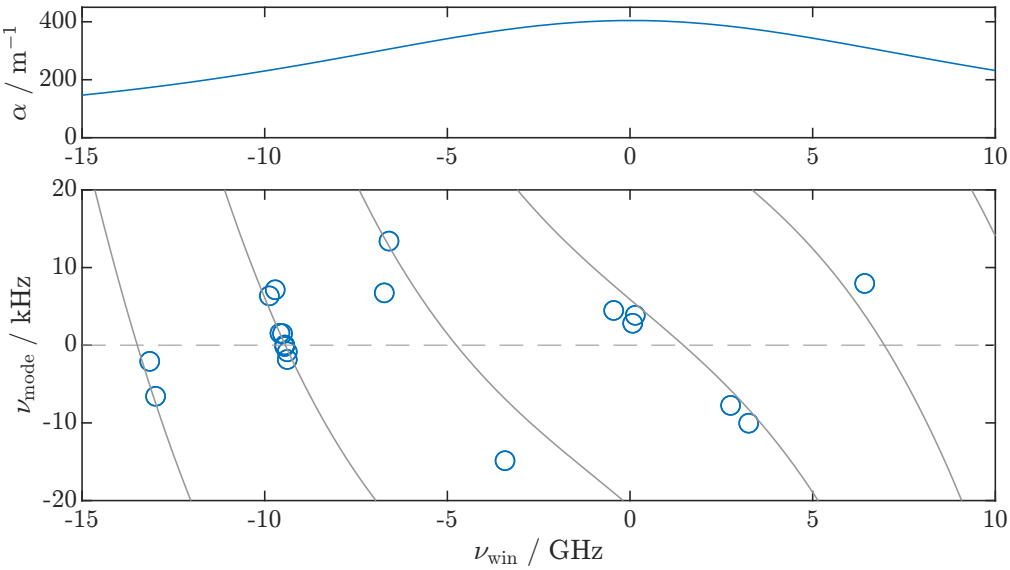


Figure 5.11: Top: Inhomogeneous profile of europium. Bottom: The mode frequency $\nu_{\text{mode}}$ as a function of window centre frequency $\nu_{\text{win}}$. Best fit of the theoretical model in grey lines. The dashed grey line is the centre of the window, where the drift is theoretically zero, to first order.

front mirror transmittivity should then be chosen to equal the total loss through absorption, scattering and transmission through the back mirror. If the back mirror has (near) unity reflectivity, the total absorbed power will then be (nearly) equal to the incoming power at resonance [58].

To calculate the effective reflectivity of the cavity, I will use the electric-field transmittivity and reflectivity $\mathbf{t}, \mathbf{r}$. For the mirrors, these are the square root of the intensity values, $\mathbf{r}_i = \sqrt{R_i}$, $\mathbf{t}_i = \sqrt{1 - R_i}$, and the round-trip absorption can be baked into a gain $g_{\text{RT}} = \exp(-\alpha L)$. Note that the electric field absorption is $\alpha/2$, but that the round-trip length is $2L$, so the 2's cancel out. To get the complete reflectivity of the cavity, $R_{\text{cav}}$, I look at the electric field reflected immediately off the first mirror ($E \propto \mathbf{r}_1$). Then I add the light which has passed through the first mirror once, reflected off the second mirror once and then passed through the first mirror again ($E \propto (i\mathbf{t}_1)^2 \mathbf{r}_2 g_{\text{RT}}$, with a phase shift $\pi/2$ for every mirror transmission [50, Chapter 11]). I keep going with light going $k$ round-trips through the cavity, squaring the final sum to get intensity reflectivity from the cavity.

$$R_{\text{cav}} = \left| \mathbf{r}_1 - \mathbf{t}_1^2 \sum_{k=1}^{\infty} \mathbf{r}_1^{k-1} g_{\text{RT}}^k \mathbf{r}_2^k \right|^2 = \mathbf{r}_1^2 \left| 1 - \mathbf{t}_1^2 g_{\text{RT}} \frac{\mathbf{r}_2}{\mathbf{r}_1} \sum_{k=0}^{\infty} \mathbf{r}_1^k g_{\text{RT}}^k \mathbf{r}_2^k \right|^2 \tag{5.26}$$

The summation is a geometric sum, with a closed-form simplification (provided an absolute value $< 1$)

$$R_{\text{cav}} = \mathbf{r}_1^2 \left| 1 - \mathbf{t}_1^2 g_{\text{RT}} \frac{\mathbf{r}_2}{\mathbf{r}_1} \frac{1}{1 - \mathbf{r}_1 g_{\text{RT}} \mathbf{r}_2} \right|^2 = \mathbf{r}_1^2 \left| 1 - \frac{1 - \mathbf{r}_1^2}{\frac{\mathbf{r}_1}{\mathbf{r}_2 g_{\text{RT}}} - \mathbf{r}_1^2} \right|^2 \tag{5.27}$$

Expressing this in the more intuitive intensity variables

$$R_{\text{cav}} = R_1 \left| 1 - \frac{1 - R_1}{\sqrt{\frac{R_1}{R_2}} \exp(\alpha L) - R_1} \right|^2 \tag{5.28}$$

Impedance matching occurs when this reflectivity is 0, and this occurs when the numerator of the fraction equals the denominator, meaning

$$\alpha L = \frac{1}{2} \ln \frac{R_2}{R_1} \tag{5.29}$$

Even if all ions within the spectral window are removed through optical pumping, there will be some residual absorption in the centre of a window, just from off resonant absorption of ions at the edge. This absorption is roughly $\alpha_c = \frac{2\alpha_0}{\pi} \arctan\left(\frac{\Gamma_h}{\Gamma_{\text{win}}}\right)$ (derived in section 3.1). For a 40 kHz wide window, given 99 % back reflectivity and assuming no other losses, this calculation told us we wanted the front mirror to be 90 % reflective.

### 5.3.2 Cooling and temperature stabilization

In 2020, we installed a pulse tube cryostat from MyCryoFirm, with an additional closed-cycle Joule-Thomson helium loop to cool samples down to below 2 K. A unique feature of this specific cryostat is an inner gas cell, into which a small amount of helium can be inserted as a transfer gas. Using this transfer gas, the entire crystal can be thermalized to the cell, without specially designed heat transfer components.

The inner cell can be cooled to 1.5 K, and has a cooling power at that temperature of 4.5 mW and an RMS temperature stability of 50 µK without and 3 µK with heating temperature regulation. Surrounding the inner cell is an optical plate and thermal shield kept at 4 K, with 289 mW of cooling power. It has an RMS temperature stability of 0.9 mK without and 50 µK with temperature regulation. Outside the 4 K shield is another thermal shield, at 50 K, before the outer shell of the cryostat. Everything between the outer shell and the inner cell is connected in a common vacuum, cryopumped to below $1 \cdot 10^{-6}$ mbar. [59]

The complete cooldown process takes roughly 30 hours, though we have at times seen slower cooldowns, especially when there is a large amount of cabling connecting the stages.



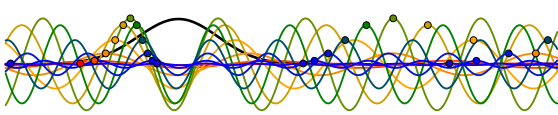

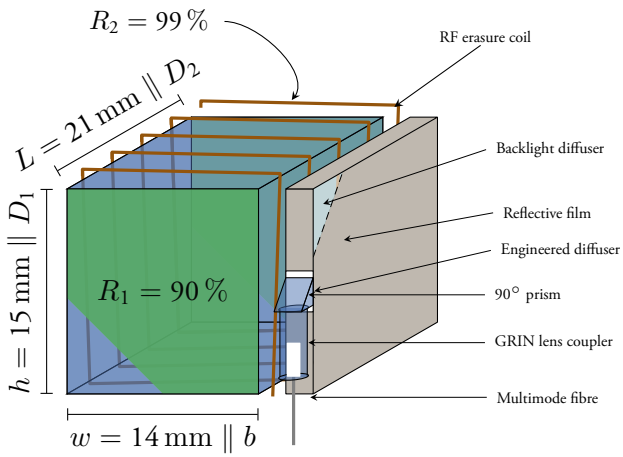


(a) Sketch of europium crystal mounted with RF erasure coil and side burner.

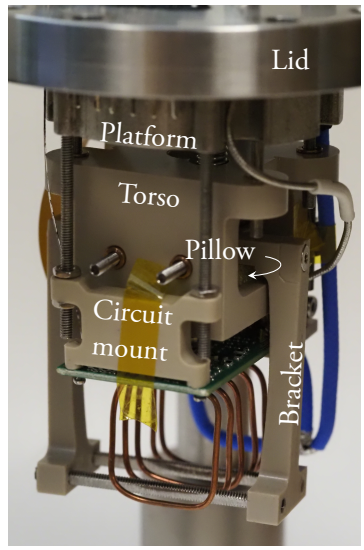


(b) Crystal holder.

Figure 5.12: Crystal assembly for experiments in europium cavity.

### 5.3.3 Mechanical isolation

The crystal was suspended in a custom-made cradle, pictured in fig. 5.12b, where it was mechanically isolated from the rest of the setup. It was designed in a way that allowed us to fine adjust its position and angle, without placing the crystal in rigid mechanical contact with the rest of the cryostat. A stainless steel platform was screwed to the bottom of the cryostat cell lid. To the platform, a polyether ether ketone (PEEK) part, which I will be referring to as the assembly's *torso*, was attached via a spring. The spring was kept in tension by three set screws, which formed a kinematic base: One screw indexed against an indentation in the platform, and another against a groove, completely restricting sliding and rotation between the two parts. This way, the three screws could be individually turned to control the precise angle and height of the torso.

In a central cavity in the torso lay a dampening pillow, and on top of that pillow rested a PEEK bracket, which extended down below the torso. Between the ends of this bracket, a pair of filed down set screws formed a shelf, where the crystal was placed for experiments. In this way, the crystal was only in mechanical contact with the cryostat and the rest of the environment through the dampening pillow. Two pairs of set screws were fixed in the torso, and one pair that could be affixed in the transverse direction. These screws could be used to minutely nudge the top of the bracket and then retracting to stay out of contact, allowing fine control of its position relative to the torso. In hindsight, most of the built-in

positioning mechanics were over-engineered. Especially the position of the bracket relative to the torso was mostly done by hand and by eye, and in the end the precision mostly seemed down to how carefully one could lower the entire assembly into the cryostat cell.

Separate to the torso, the circuit board used for RF erasure was mounted to a pair of PEEK mounts, in turn hanging off nuts, fixed to bolts screwed directly to the platform. The height of the circuit board could be adjusted by turning the nuts. This separation was necessary as the RF coil needed to surround the crystal, while maintaining as small an area as possible to maximize the magnetic field output. In order to position the crystal inside the coil and out of mechanical contact with it, we needed them to be positioned separately.

During exploratory experiments, an issue was discovered wherein the crystal was rocking back and forth on a 47 Hz frequency. The source of this noise was never conclusively identified, though it could be measured in the lab with a microphone. It appeared as if this fed some resonance in the holder causing quite large ($\approx$ 100 µrad) horizontal gyrations. This rotation caused issues both for alignment of the reflected beam and for measurements of the cavity modes. Since the resulting frequency shifts were on the order of 10 kHz, long and repeatable stabilization experiments would have been difficult. Our hypothesis is that the ball of thin copper wire we had until then used as a dampening pillow either did not sufficiently dampen acoustic vibrations, or even introduced a pivot around which the bracket could rotate, creating a new mode of vibration. In order to combat this, the copper pillow was replaced by a 3 mm thick square of dampening open-cell ("high temperature") polyimide foam from McMaster-Carr. After this replacement, the magnitude of this vibration was much lower, though some mechanical noise could still be identified in the feedback signal when locked.

### 5.3.4 Spectral tailoring

In previous experiments using spectral tailoring for quantum information purposes, the same beam could often be used for both creating the spectral structures by hole burning and experimenting on those structures. When introducing the reflective cavity, however, burning along the optical axis turned out to be ineffective. Not only was much of the intensity lost in reflection off the first mirror but, more importantly, the cavity modes caused spectral and spatial high and low intensity spots due to standing waves in the cavity. Together with slow light-induced non-linearities, this led to a highly unrepeatable experiment: a recipe that lead to good hole burning one day might, due to miniscule changes in position, angle and focus, be completely unusable the next.

Instead, the experiment geometry was updated to allow an orthogonal beam to irradiate the entire crystal. This *side burning* made it possible to repeatably tailor the whole crystal, without cavity effects. Initial experiments with this geometry discovered that simply



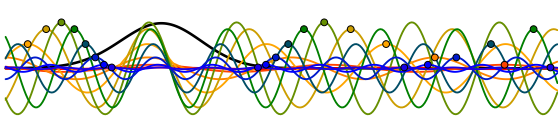

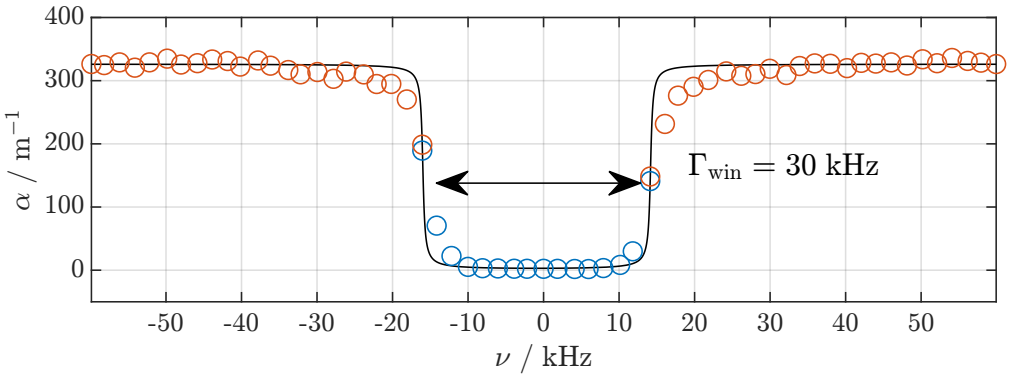


Figure 5.13: A 30 kHz wide spectral window burned in europium, using the fibre coupled side burner. The two colours correspond to measurements taken using two different detector gain settings, to capture the large dynamic range. The black line is the theoretical absorption profile for a perfect square population window.

expanding a burning beam and illuminating the entire crystal did not quite lead to perfect removal of the ions throughout. We hypothesized that the cause of this residual population was interference effects near the mirrors. Coherent light at grazing incidence will cause a band of low intensity near the mirror, where the ions will simply never be excited. We discovered that the residual population could be removed to a large degree if the side burning beam was diffused and spatially modulated – in the praseodymium experiment this was realized by inserting a piece of lens tissue in the beam path and dithering the beam angle.

In the new cryostat, described in section 5.3.2, only one optical axis was available, making an open air beam geometry impossible. Even if such a geometry could be used, the europium crystal is prohibitively large, and it would be difficult to effectively burn it in its entirety. In order to still utilize the side burning geometry, a fibre-coupled burner was designed, shown in fig. 5.12a. Light is coupled into a multimode fibre, which is threaded through fibre throughputs on the cryostat. On the output, the light is collimated by a GRIN lens, reflected by a prism and directed onto an engineered diffuser. This engineered diffuser spreads the light into a sheet (in the plane orthogonal to the burning direction). Finally, a rectangular piece of diffusive plastic, part of a commercially available LED backlight module, scatters the light diffusely, some of it into the crystal, and some of it towards the back and sides. Surrounding the diffusive plastic is a sheet of reflective material, to give this lost light more chances to help the burning process. What comes out is a physically wide, diffusive light. This geometry worked well, allowing us to burn structures like fig. 5.13.

In order to ensure that no speckles remained over time we also designed and built a fibre mode scrambler, inspired by Ref. [60]: A brushless motor with an offset weight load was tied up in a web of elastic cords, such that it would shake when the motor spun. Wiring the

fibre between the elastic cords would cause a fluctuation in which fibre modes are excited, which would hopefully over time average out the speckle effects on the output of the side burner, like the dithering did for the praseodymium experiment. Unfortunately, this mode scrambler could never quite be shown to work – it always left worse windows rather than better. Our leading hypothesis is that the scrambler vibrated at too high a frequency and amplitude, even when the motor was running on the lowest speed, widening the spectrum of the burning laser and attenuating the transmitted light. The measurement of the mode matching criterion in paper II, performed without the mode scrambler, gave an estimate of remaining absorption in the middle of the window. The results indicate that a very small portion, probably less than 0.02 %, of the ions remained unburned anyway, so we left further experiments with mode scrambling to the future.

### 5.3.5 Erasure

After a successful lock, or any other probing of the spectral structure, it will be perturbed by resonant and off-resonant excitation, and with time the structure also degrades by hyperfine relaxation – though this effect will be very small in europium thanks to its long hyperfine lifetimes [37]. This degradation is the source of the first order drift as discussed in section 5.2.3. In order to achieve repeatable experiments, and in the end a sustainable stabilization scheme, it is important that the spectral structure can be reset. Simply burning at the same frequencies again is not sufficient, as it will not affect ions which have relaxed to other frequencies.

#### Time erasure

The simplest way to reset the structure is to just wait for hyperfine relaxation to bring the ions back into their natural distribution. In many atomic species there is no choice, as this will inevitably happen over the course of an experiment. But the property that makes our specific materials, praseodymium and europium, especially useful for laser stabilization – their long hyperfine lifetimes – is a problem for this idea.

The natural lifetime of structures in $Pr^{3+}$:$Y_2SiO_5$ is a few minutes [49], though this was in our experiments intentionally increased by applying a magnetic field. Waiting that long between runs in an experiment is an inconvenience. In $Eu^{3+}$:$Y_2SiO_5$, the corresponding lifetime has been measured to be on the order of weeks [37]. Anecdotally, it was not unusual during our lab runs to return to the lab after a good night's sleep, or to a specific frequency days after it was last used, to find a spectral window already in place. Clearly, time erasure is not a viable method for this application.



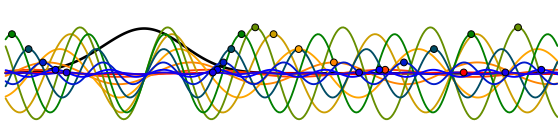

### Thermal erasure

The lifetime is heavily temperature dependant, and above 20 K, the lifetime in europium is less than a second [45]. This is of course short enough that one could realistically thermocycle the crystal to erase all structure in the absorption profile.

Unfortunately, this kind of short term changes in temperature still takes some time to perform in a cryostat like ours, on the order of half an hour both ways. Additionally, there is always a risk that thermal cycling incurs some thermal or mechanical hysteresis, reducing the repeatability of experiments.

### Optical erasure

One possible solution is to use a laser that is tunable over a wide enough portion of the inhomogeneous profile and iteratively exciting all the ions, allowing them to settle in their natural distribution. A version of this optical erasure scheme has been used in previous spectral tailoring experiments. Unfortunately, as discussed in section 5.3.4, there is functionally no optical access for this kind of operation along the locking axis because of the mirror coating. Instead, this erasure scheme would need to be carried out in the orthogonal direction, and over the entire crystal.

$Y_2SiO_5$has a unit cell with volume $V_c = 0.8805\,\mathrm{nm}^3$, in which resides sixteen $Y^{3+}$ atoms, eight in each of two optically distinguishable sites (as discussed in section 4.1.1). Of these $Y^{3+}$ ions, our crystal has 1 % replaced with $Eu^{3+}$, which across the entire crystal means $N = 1\,\% \cdot 8 \frac{21\times14\times15\,\mathrm{mm}^3}{0.8805\,\mathrm{nm}^3} = 4\cdot10^{20}$ $Eu^{3+}$ ions in each site. For simplicity, let's say about 10 % of those ions lie within the frequency region where they would need to be excited at least once to erase the structure. The total energy absorbed would be $E_{\mathrm{abs}} = N \cdot 10\,\% \cdot h\nu = 14\,\mathrm{J}$ for each excitation pulse, of which we would need several. To put this in context, the total available cooling power of the cryostat's inner cell is $4.5\,\mathrm{mW}$, and it would therefore take an hour just to dissipate the heat of one of the erasure pulses. Even in the best case, erasing like this would take several hours of continuous irradiation. With an inhomogeneous profile as wide as that in our europium crystal comes the additional issue that the erasure laser would need an extremely wide sweep range. While we can tune our laser over tens of nanometres, we can not seamlessly tune it this far, without manual intervention and a certain amount of hysteresis.

### RF erasure

To get around these problems, we opted for an erasure scheme as described in paper IV, where a field is directly coupled to the ground state hyperfine transitions, rather than indir-

ectly across the optical transition. The field is generated by a coil surrounding the crystal, which is driven by an electronic oscillator. In the praseodymium crystal, this was tested in a broadband configuration, where all transitions were driven in tandem by a broadband RF field – really a sample QPSK communication signal, but effectively a pseudorandom phase modulated signal. This RF signal was amplified and fed through a coaxial cable into the cryostat where the cable was separated out into two leads, coiled one turn each around the crystal. We made sure that the coiling direction for each of the leads was correct, so that the generated magnetic field would add constructively. A coaxial cable then carried the signal out of the cryostat and into a 20 dB RF attenuator and a 50 Ω terminator, to ensure a potential difference between the two leads. We determined experimentally that 20 ms of this treatment was sufficient to satisfactorily reset our structures.

For the europium experiments, this broadband scheme became less viable for a number of reasons: Europium has larger hyperfine splittings and smaller magnetic dipole moments, and the crystal is larger. This means the antenna needs to cover a larger frequency range and output more power. Instead of the simple broadband antenna, a tunable antenna was created, described in paper III. The resonance frequency of this antenna could be successively tuned using switched capacitor banks to in turn be resonant with each of four transitions – two per isotope – and was therefore capable of generating a larger magnetic field without dumping that much more power as heat in the cryostat. Simultaneously, the impedance of the circuit was tuned to be impedance matched with the signal generating circuit outside the cryostat, avoiding losses in the cables.

Paper III concerns the electronic device in itself, and we evaluate the operating frequency range, quality factor and magnetic field at room temperature and 1.5 K. In paper IV we studied the effect this erasure had on our ions. By burning spectral windows in europium and burning back specific ion classes, we measured the linewidth for each of the four ground state hyperfine transitions. We could then calibrate RF pulses to perform $\pi/2$-transfers between the ground state hyperfine levels, erasing the majority of a structure with a handful of pulses. The remaining structure, unfortunately, took many pulses to erase. This is likely due to the $|\pm\frac{3}{2}g\rangle \rightarrow |\pm\frac{5}{2}g\rangle$ transition in $^{153}$Eu, which was so broad and had such low absorption that it was difficult to detect and calibrate. The pulse area for this transition appears to have not been very close to $\frac{\pi}{2}$, and if we underestimated the spin broadening our sweep range may have been a bit too small. On top of this, the quality factor and efficiency of the antenna decreases at large frequencies, meaning that the magnetic field strength was lower at this transition frequency, where we would have needed it more. Running many shots of erasure was nevertheless a practical, if somewhat slower than hoped, solution to the problem.



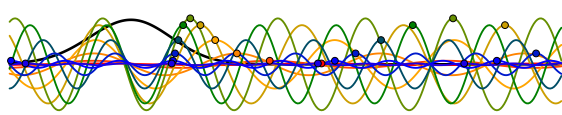

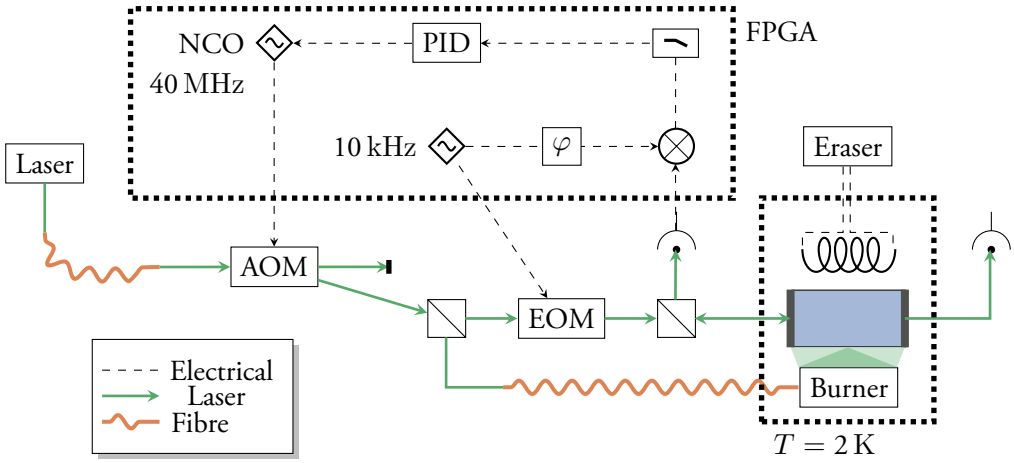


Figure 5.14: Schematic sketch of the optical and electrical setup for the laser locking experiments in europium.

### 5.3.6 Servo

In the praseodymium experiment, PDH locking was performed using an analogue laser servo (Vescent D2-125) driving a voltage controlled oscillator for the feedback. For the europium experiment, we realized it would be more flexible and future-proof to use a Field-programmable gate array (FPGA). Since we would be locking to such narrow and stable modes, we could accept the downside of lower bandwidth for a digital solution. A mostly ready-made solution for this had already been designed at NIST [61], using an FPGA from Koheron.

Figure 5.14 shows the general setup for these experiments, including a rough schematic of the optics. An acousto-optic modulator (AOM) shifted the frequency of the incoming laser light by 40 MHz. Part of the light was split off for the locking loop, while the majority was fed to the side burner assembly (section 5.3.4) for spectral tailoring. A 10 kHz modulation signal from the FPGA drove an electro-optic modulator (EOM), which applied sidebands to the locking laser before it was reflected off the cavity. The reflected light was captured by a photodetector and digitized, and a Pound-Drever-Hall error signal generated as described in section 2.2, mixing the reflection signal with a phase-shifted copy of the modulation signal to create a slowly varying variable representing the phase difference between the two signals. After low-pass filtering, this error signal was fed to a digital PID controller, the output of which controlled the output frequency of a numerically controlled oscillator (NCO), which in turn drove the frequency-shifting AOM, closing the feedback loop.

### 5.3.7 Laser source

These experiments were all performed using a Coherent 699-21 ring laser with a 6 W diode pump laser and rhodamine 6G as the gain medium. This laser was locked to a ULE cavity and stabilized to a linewidth believed to be on the order of 10 Hz, using an intracavity EOM, a piezo tweeter mirror and a galvo controlled interferometer (in order of decreasing frequency bandwidth).

### 5.3.8 Locking power

Minimizing drift includes minimizing the locking power used, as this causes off-resonant excitation (section 5.2.3). At the same time, there is a minimum power necessary to stabilize a laser to a specific level, given by noise sources in the setup.

Appendix C of paper I uses Ref. [28] to derive an expression for the shot-noise limited Allan deviation $\sigma_y$ (note that paper I uses a convention with a non-normalized Allan deviation, I am correcting by a factor $\nu$ here to be consistent with Ref. [52]):

$$\sigma_y(\tau) = \frac{1}{\sqrt{2\tau}} \frac{1}{4} \sqrt{\frac{h\nu}{P_c}} \frac{\Delta\nu_{\text{cav}}}{\nu} , \tag{5.30}$$

where $\tau$ is the averaging time, $h$ is Planck's constant, $\nu$ is the laser frequency, $P_c$ is the carrier power of the locking beam and $\Delta\nu_{\text{cav}}$ is the cavity linewidth. Isolating $P_c$ gives

$$P_c = \frac{1}{2\tau} \frac{1}{16} \frac{h\Delta\nu_{\text{cav}}^2}{\nu\sigma_y(\tau)^2} . \tag{5.31}$$

Setting a target Allan deviation of $\sigma_y(1\,\text{s}) = 1 \cdot 10^{-17}$ allows me to calculate a necessary carrier power given a linewidth $\Delta\nu_{\text{cav}} = 3\,\text{kHz}$, $P_c = 1.2\,\text{nW}$.

This power should be raised to compensate for detector noise, which is quoted for our detector as $\mu = 15\,\text{fA}/\sqrt{\text{Hz}}$ at our modulation frequency $\nu_{\text{mod}} = 10\,\text{kHz}$. The modulation depth is set to the optimum derived in Ref. [28], so the power in each of the sidebands $P_s = 0.42P_c$. This gives rise to a signal current

$$i_s = \frac{2P_s q}{h\nu} = 0.47\,\text{nA} \tag{5.32}$$

with elementary charge $q$, assuming unity quantum efficiency. To get the same signal-to-noise ratio including the amplifier noise, the detector current must increase to

$$i_{\text{comp}} = \frac{i_s}{2} + \sqrt{\frac{i_s^2}{4} + \frac{i_s}{2q}\mu^2} = 0.86\,\text{nA} . \tag{5.33}$$



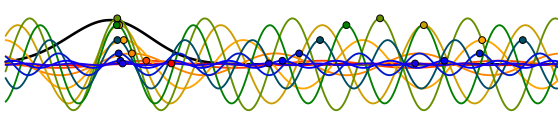

Using the quoted diode responsivity for our diode $\rho = 0.35\,\mathrm{A\,W^{-1}}$, the sideband power required to achieve this current is $P_{s,\mathrm{comp}} = i_{\mathrm{comp}}/(2\rho)$, and the total locking power becomes

$$P_{\mathrm{comp}} = \left(2 + \frac{1}{0.42}\right) P_{s,\mathrm{comp}} = 5.4\,\mathrm{nW}\ . \tag{5.34}$$

In experiments, we predicted narrower cavity modes than this, and therefore used less locking power (approximately 2.5 nW). Together with poor cavity coupling, this means the stability of the lock could likely be improved with increased locking power.

# Chapter 6

# Conclusions and outlook

*Wer viel misst, misst viel Mist*
*(*English: *Whoever measures much, measures much manure)*
*(*Scanian: *Mäter man möed, mäter man möed mög)*

— German proverb

## 6.1 Conclusion

The goal of this project was to establish, improve and evaluate slow light laser frequency stabilization, locking the frequency of a laser to the modes of a slow light-enabled cavity. By spectral tailoring, we established semi-permanent spectral transparency windows in a rare-earth ion doped crystal, causing large dispersion. In a cavity constructed by depositing mirrors onto the faces of this crystal, the cavity mode widths were narrowed by this dispersion, to the point where they were comparable with those of a thousands or hundreds of thousands times longer cavity.

I have shown that this method reduces sensitivity to length changes, which suggests that it may help combat the limiting factor to state-of-the-art laser frequency stabilization, Brownian length uncertainty. The slow light stabilization scheme introduces new sources of frequency drift, primarily a power-independent drift from hyperfine cross-relaxation deteriorating the transparency windows, and a drift caused by off-resonant excitation in the window edges by the locking beam, but I have demonstrated methods by which these drift sources can be minimized.

An important step on the way to perfecting this scheme was the creation of a cavity with a spacer made from $Eu^{3+}$:$Y_2SiO_5$, a material where the hyperfine cross-relaxation is essentially



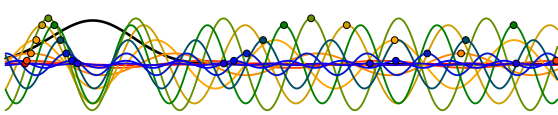

negligible due to its long hyperfine lifetimes. Additionally, the ions' narrow homogeneous linewidth means spectral windows can be made very narrow and with steep edges, increasing the slow light effect. In creating this cavity, we decided a number of design parameters through iterative calculations and measurements.

In order to use this cavity we developed a side-burning geometry, and built a fibre coupled burner which allowed us to efficiently create spectral structures throughout the entire crystal. We also designed and evaluated an RF erasure circuit to quickly reset these structures for repeated experiments.

The resulting cavity modes display a $Q$ factor in excess of $10^{11}$. When stabilizing a laser to these modes using Pound-Drever-Hall locking, we measured a drift rate at the $\mathrm{Hz\,s^{-1}}$ level, and the currently limiting source of drift can potentially be reduced by five orders of magnitude with appropriate experimental means.

## 6.2 Delays and complications

I started this programme in April 2019, with an initial plan to finish in 4.5 years (4 years of studies and research, plus 10 % teaching). As evident from the fact that I'm writing this document 5.5 years later, complications appeared along the way.

One of those complications was the fact that I enjoy teaching. This is a dangerous thing to admit in a department that desperately needs lab and exercise supervisors.

The second, more serious, complication appeared in 2020 with the COVID-19 pandemic. This caused slow-downs in every part of the project: Lab work was cancelled or slowed down to accommodate social distancing rules. Teaching was forced to take on new shapes, which increased the time requirements. Deliveries from and communications with international suppliers and collaborators were delayed – Sweden's famously lax position does not help, when your cryostat is being manufactured by a company in locked-down France. I count myself among the lucky ones who did not catch the disease itself until after vaccines became available, but my productivity was certainly hampered by slowdowns in communication within the group, as we all needed to work from home for months.

Finally, this is a complicated experiment, with many interlocking parts. Many times we found ourselves locked behind one broken piece of equipment or another. It was only when the laser, cryostat, crystal mount, optics, and electronics were simultaneously available and operational that we could take any measurements.

For these reasons, and because of a few experimental missteps which do not need to be recounted, many of them mine, my involvement in this project ends short of the initial goal: To truly demonstrate a record-breaking laser stabilization scheme. The data we did

collect (presented in papers II to IV), all came in at the last hour – literally, for some of it. As disappointing as it is to be this close to the finish line, believing without conclusive evidence to have already crossed it, at least I know there are people continuing the research.

## 6.3 Outlook

A true evaluation of the slow light laser frequency stabilization scheme would require a more stable reference than the laser used in our experiments. Every measurement of frequency is really only stable relative to a reference, and the limiting factor in our case has mainly been the fact that the input laser passes through a long optical fibre. This broadens the linewidth to the point where our experiment mostly measured the laser's stability. One way around this problem is fibre noise cancellation [57], in which the noise induced by the fibre is compensated using an AOM. Another possibility, which we have planned for from the start, is to not compare your sample to a better reference, but to another identical sample. In our scheme, this would take the shape of placing one locking beam on each of two distinct spots on the crystal face, and doing separate PDH locking on each of them. Then their drift and variation could be measured relative to each other. This will cancel out all common error sources such as input laser linewidth and slow mechanical noise, but allows us to measure the Allan deviation resulting from Brownian frequency noise, as this will be completely uncorrelated between the two spots on the crystal.

In future experiments, it will be crucial to get the mode better centred in the window. The best centred mode we managed to lock to was 2 kHz from the middle of the window, but it should in principle be possible to get it under 1 Hz. This would only require more lab time, a commodity we sadly ran out of.

An experiment which we prepared for several times but which never came to fruition for practical reasons is an experimental verification of the slow light reduction of angle sensitivity. The setup to measure this would consist of two flat mirrors and two identical lenses arranged as mirror, lens, mirror, lens, crystal, such that the distance between each pair of components is the same, equal to the focal length of the lenses, $f$. Because the total distance covered is $4f$, this device is called a $4f$-setup. The purpose is to uncouple the angle and position of the probing beam – adjusting the angle of the first mirror will only affect the angle at the crystal face, and adjusting the angle of the second will only affect its position. To measure the angle sensitivity, we can put the first mirror in a motorized mirror mount, and measure the PDH feedback signal for a locked beam while varying the mirror angle. The difficulty in this experiment comes down to guaranteeing that the frequency shifts result from angle changes, which requires a carefully assembled and calibrated $4f$ setup. For this reason this experiment was often scrapped for time.



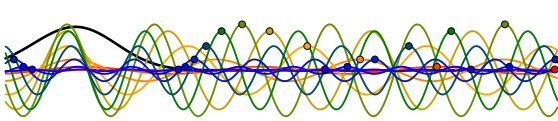

We mostly treated the fast light effect as an opportunity to develop our spectral control, and did not spend too much energy evaluating potential practical uses. From the success of this experiment, it seems $Eu^{3+}$:$Y_2SiO_5$ is a good candidate for implementing any such uses that arise. Investigating a fast light cavity as a white-light interferometer with increased, rather than reduced, sensitivity to length changes could be an interesting future project.

It is worth noting that the slow light stabilization scheme is not in direct conflict with the other strategies to decrease frequency noise under investigation, discussed in section 2.1. Slow light frequency stabilization could, for instance, very well be performed in a longer cavity with crystalline mirrors, and both colder temperatures and larger beam areas are beneficial rather than detrimental to the technique.

# References


[1] S. P. Horvath *et al.*, 'Slow light frequency reference cavities—proof of concept for reducing the frequency sensitivity due to length fluctuations', *New Journal of Physics*, vol. 24, no. 3, p. 033 034, Mar. 2022. DOI: 10.1088/1367-2630/ac5932.

[2] D. Gustavsson *et al.*, 'Using slow light to enable laser frequency stabilization to a short, high-Q cavity', Manuscript submitted for publication, 2024. arXiv: 2408.11703 [physics.optics].

[3] M. Lindén, D. Gustavsson, K. Shortiss and L. Rippe, 'Highly tuneable in-situ cryogenic switch bank resonator for magnetic field generation at radio-frequencies', Manuscript in preparation, 2024.

[4] M. Lindén, D. Gustavsson, A. Walther, A. Kinos and L. Rippe, 'Resetting spectral hole features in Eu:YSO using a highly tunable radio-frequency resonance circuit', Manuscript in preparation, 2024.

[5] A. J. Renders *et al.*, 'Pushing the limits of negative group velocity', Manuscript submitted for publication, 2024. arXiv: 2404.04771 [physics.atom-ph].

[6] B. Shaw, 'Light of other days', *Analog*, Aug. 1966.

[7] H. Margolis, 'A brief history of timekeeping', en, *Physics World*, vol. 31, no. 11, p. 27, Nov. 2018, ISSN: 2058-7058. DOI: 10.1088/2058-7058/31/11/36.

[8] F. Gribenski, 'Tuning forks as time travel machines: Pitch standardisation and historicism', English, *Sound Studies*, vol. 6, no. 2, pp. 153–173, Jul. 2020, ISSN: 2055-1940, 2055-1959. DOI: 10.1080/20551940.2020.1794628.

[9] A. J. Ellis, 'The history of musical pitch', en, *Nature*, vol. 21, no. 545, pp. 550–554, Apr. 1880, ISSN: 1476-4687. DOI: 10.1038/021550a0.

[10] L. Essen and J. V. L. Parry, 'The caesium resonator as a standard of frequency and time', *Philosophical Transactions of the Royal Society of London. Series A, Mathematical and Physical Sciences*, vol. 250, no. 973, pp. 45–69, 1957, ISSN: 0080-4614.




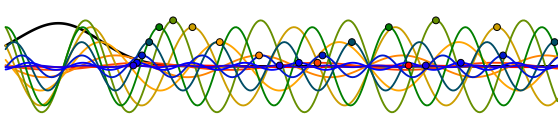

[11] L. Essen, J. V. L. Parry, W. Markowitz and R. G. Hall, 'Variation in the speed of rotation of the earth since june 1955', en, *Nature*, vol. 181, no. 4615, pp. 1054–1054, Apr. 1958, ISSN: 1476-4687. DOI: 10.1038/1811054a0.

[12] N. Dimarcq *et al.*, 'Roadmap towards the redefinition of the second', English, *Metrologia*, vol. 61, no. 1, p. 012001, Feb. 2024, ISSN: 0026-1394, 1681-7575. DOI: 10.1088/1681-7575/ad17d2.

[13] Y. Y. Jiang *et al.*, 'Making optical atomic clocks more stable with $10^{-16}$ level laser stabilization', *Nature Photonics*, vol. 5, no. 3, pp. 158–161, Mar. 2011, arXiv:1101.1351 [physics], ISSN: 1749-4885, 1749-4893. DOI: 10.1038/nphoton.2010.313.

[14] C. W. Chou, D. B. Hume, T. Rosenband and D. J. Wineland, 'Optical clocks and relativity', *Science*, vol. 329, no. 5999, pp. 1630–1633, Sep. 2010. DOI: 10.1126/science.1192720.

[15] C. Eisele, A. Y. Nevsky and S. Schiller, 'Laboratory test of the isotropy of light propagation at the $10^{-17}$ level', *Physical Review Letters*, vol. 103, no. 9, p. 090401, Aug. 2009. DOI: 10.1103/PhysRevLett.103.090401.

[16] B. P. Abbott *et al.*, 'Ligo: The laser interferometer gravitational-wave observatory', en, *Reports on Progress in Physics*, vol. 72, no. 7, p. 076901, Jun. 2009, ISSN: 0034-4885. DOI: 10.1088/0034-4885/72/7/076901.

[17] L. S. Collaboration and V. Collaboration, 'Observation of gravitational waves from a binary black hole merger', *Physical Review Letters*, vol. 116, no. 6, p. 061102, Feb. 2016. DOI: 10.1103/PhysRevLett.116.061102.

[18] N. Hinkley *et al.*, 'An atomic clock with $10^{-18}$ instability', *Science*, vol. 341, no. 6151, pp. 1215–1218, Sep. 2013. DOI: 10.1126/science.1240420.

[19] B. E. A. Saleh and M. C. Teich, *Fundamentals of photonics.* (Wiley series in pure and applied optics). Wiley Interscience, 2007, ISBN: 9780471358329.

[20] N. Ismail, C. C. Kores, D. Geskus and M. Pollnau, 'Fabry-pérot resonator: Spectral line shapes, generic and related airy distributions, linewidths, finesses, and performance at low or frequency-dependent reflectivity', EN, *Optics Express*, vol. 24, no. 15, pp. 16366–16389, Jul. 2016, ISSN: 1094-4087. DOI: 10.1364/OE.24.016366.

[21] K. Numata, A. Kemery and J. Camp, 'Thermal-noise limit in the frequency stabilization of lasers with rigid cavities', English, *Physical Review Letters*, vol. 93, no. 25, p. 250602, Dec. 2004, ISSN: 0031-9007. DOI: 10.1103/PhysRevLett.93.250602.

[22] A. Einstein, 'Zur elektrodynamik bewegter körper', *Annalen der Physik*, vol. 17, pp. 891–, Jun. 1905.

[23] E. Wiens *et al.*, 'Silicon single-crystal cryogenic optical resonator', English, *OPTICS LETTERS*, vol. 39, no. 11, pp. 3242–3245, Jun. 2014, Web of Science ID: WOS:000337107100041, ISSN: 0146-9592, 1539-4794. DOI: 10.1364/OL.39.003242.

[24] G. D. Cole, W. Zhang, M. J. Martin, J. Ye and M. Aspelmeyer, 'Tenfold reduction of brownian noise in high-reflectivity optical coatings', en, *Nature Photonics*, vol. 7, no. 8, pp. 644–650, Aug. 2013, ISSN: 1749-4893. DOI: 10.1038/nphoton.2013.174.

[25] D. Kedar *et al.*, 'Frequency stability of cryogenic silicon cavities with semiconductor crystalline coatings', English, *OPTICA*, vol. 10, no. 4, pp. 464–470, Apr. 2023, Web of Science ID: WOS:000982885600006, ISSN: 2334-2536. DOI: 10.1364/OPTICA.479462.

[26] S. Häfner *et al.*, '$8 \times 10^{-17}$ fractional laser frequency instability with a long room-temperature cavity', EN, *Optics Letters*, vol. 40, no. 9, pp. 2112–2115, May 2015, ISSN: 1539-4794. DOI: 10.1364/OL.40.002112.

[27] R. Drever *et al.*, 'Laser phase and frequency stabilization using an optical-resonator', English, *Applied Physics B – Photophysics and Laser Chemistry*, vol. 31, no. 2, pp. 97–105, 1983, ISSN: 0721-7269. DOI: 10.1007/BF00702605.

[28] E. D. Black, 'An introduction to pound-drever-hall laser frequency stabilization', English, *American Journal of Physics*, vol. 69, no. 1, pp. 79–87, Jan. 2001, ISSN: 0002-9505, 1943-2909. DOI: 10.1119/1.1286663.

[29] G. Diener, 'Superluminal group velocities and information transfer', English, *Physics Letters A*, vol. 223, no. 5, pp. 327–331, Dec. 1996, ISSN: 0375-9601. DOI: 10.1016/S0375-9601(96)00767-0.

[30] J. Ahlander, N. Pollard and M. Mannes, *Sweden's LKAB finds europes biggest deposit of rare earth metals*, 13th Jan. 2023. [Online]. Available: https://www.reuters.com/markets/commodities/swedens-lkab-finds-europes-biggest-deposit-rare-earth-metals-2023-01-12/.

[31] M. Nilsson and S. Kröll, 'Solid state quantum memory using complete absorption and re-emission of photons by tailored and externally controlled inhomogeneous absorption profiles', English, *Optics Communications*, vol. 247, no. 4–6, pp. 393–403, Mar. 2005, ISSN: 0030-4018, 1873-0310. DOI: 10.1016/j.optcom.2004.11.077.

[32] A. Kinos, L. Rippe, A. Walther and S. Kröll, 'Microscopic treatment of instantaneous spectral diffusion and its effect on quantum gate fidelities in rare-earth-ion-doped crystals', English, *Physical Review A*, vol. 105, no. 3, p. 032 608, Mar. 2022, ISSN: 2469-9926, 2469-9934. DOI: 10.1103/PhysRevA.105.032608.



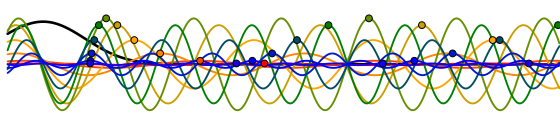

[33] *Yttrium orthosilicate - Y2SiO5 | scientific materials | YSO laser materials*. [Online]. Available: https://www.scientificmaterials.com/products/yso_Y2SiO5_yttrium-orthosilicate.php.

[34] P. Villars and K. Cenzual, Eds., *Y2SiO5 (Y2[SiO4]O ht) crystal structure: Datasheet from "pauling file multinaries edition – 2022"*, accessed 2024-06-13. [Online]. Available: https://materials.springer.com/isp/crystallographic/docs/sd_0309362.

[35] R. W. Equall, R. L. Cone and R. M. Macfarlane, 'Homogeneous broadening and hyperfine structure of optical transitions in Pr3+:Y2SiO5', *Phys. Rev. B*, vol. 52, pp. 3963–3969, 1995, ISSN: 6.

[36] M. Afzelius *et al.*, 'Demonstration of atomic frequency comb memory for light with spin-wave storage', *Physical Review Letters*, vol. 104, no. 4, p. 040 503, Jan. 2010.

[37] R. Oswald, M. G. Hansen, E. Wiens, A. Y. Nevsky and S. Schiller, 'Characteristics of long-lived persistent spectral holes in $Eu^{3+}$:$Y_2SiO_5$ at 1.2 k', *Physical Review A*, vol. 98, no. 6, p. 062 516, Dec. 2018. DOI: 10.1103/PhysRevA.98.062516.

[38] R. Yano, M. Mitsunaga and N. Uesugi, 'Ultralong optical dephasing time in Eu3:Y2SiO5', en, *Optics Letters*, vol. 16, no. 23, p. 1884, Dec. 1991, ISSN: 0146-9592, 1539-4794. DOI: 10.1364/OL.16.001884.

[39] R. Yano, M. Mitsunaga and N. Uesugi, 'Nonlinear laser spectroscopy of Eu3+:Y2SiO5 and its application to time-domain optical memory', en, *Journal of the Optical Society of America B*, vol. 9, no. 6, p. 992, Jun. 1992, ISSN: 0740-3224, 1520-8540. DOI: 10.1364/JOSAB.9.000992.

[40] M. Silver, R. Joseph and D. Hoult, 'Selective spin inversion in nuclear magnetic-resonance and coherent optics through an exact solution of the bloch-riccati equation', English, *Physical Review A*, vol. 31, no. 4, pp. 2753–2755, 1985, ISSN: 1050-2947. DOI: 10.1103/PhysRevA.31.2753.

[41] I. Roos and K. Mølmer, 'Quantum computing with an inhomogeneously broadened ensemble of ions: Suppression of errors from detuning variations by specially adapted pulses and coherent population trapping', *Physical Review A*, vol. 69, no. 2, p. 022 321, Feb. 2004. DOI: 10.1103/PhysRevA.69.022321.

[42] L. Rippe, M. Nilsson, S. Kröll, R. Klieber and D. Suter, 'Experimental demonstration of efficient and selective population transfer and qubit distillation in a rare-earth-metal-ion-doped crystal -: Art. no. 062328', English, *Physical Review A*, vol. 71, no. 6, p. 062 328, Jun. 2005, ISSN: 1050-2947, 1094-1622. DOI: 10.1103/PhysRevA.71.062328.

[43] L. Rippe, B. Julsgaard, A. Walther, Y. Ying and S. Kröll, 'Experimental quantum-state tomography of a solid-state qubit', English, *Physical Review A*, vol. 77, no. 2, p. 022 307, Feb. 2008, ISSN: 1050-2947, 1094-1622. DOI: 10.1103/PhysRevA.77.022307.

[44] M. Tian, T. Chang, K. D. Merkel and W. R. Babbitt, 'Reconfiguration of spectral absorption features using a frequency-chirped laser pulse', English, *Applied Optics*, vol. 50, no. 36, pp. 6548–6554, Dec. 2011, ISSN: 1559-128X, 2155-3165. DOI: 10.1364/AO.50.006548.

[45] F. Könz *et al.*, 'Temperature and concentration dependence of optical dephasing, spectral-hole lifetime, and anisotropic absorption in Eu3+:Y2SiO5', en, *Physical Review B*, vol. 68, no. 8, p. 085 109, Aug. 2003, ISSN: 0163-1829, 1095-3795. DOI: 10.1103/PhysRevB.68.085109.

[46] J. M. Elson, J. P. Rahn and J. M. Bennett, 'Relationship of the total integrated scattering from multilayer-coated optics to angle of incidence, polarization, correlation length, and roughness cross-correlation properties', EN, *Applied Optics*, vol. 22, no. 20, pp. 3207–3219, Oct. 1983, ISSN: 2155-3165. DOI: 10.1364/AO.22.003207.

[47] *Polaris-k15 thermal repeatability*, 14th Jul. 2024. [Online]. Available: https://www.thorlabs.com/newgrouppage9.cfm?objectgroup_id=3912.

[48] A. Kinos, Q. Li, L. Rippe and S. Kröll, 'Development and characterization of high suppression and high étendue narrowband spectral filters', *Applied Optics*, vol. 55, no. 36, pp. 10 442–10 448, Dec. 2016, ISSN: 1559-128X. DOI: 10.1364/AO.55.010442.

[49] K. Holliday, M. Croci, E. Vauthey and U. P. Wild, 'Spectral hole burning and holography in an Y2SiO5:Pr3+ crystal', *Physical Review B*, vol. 47, no. 22, pp. 14 741–14 752, Jun. 1993. DOI: 10.1103/PhysRevB.47.14741.

[50] A. E. Siegman, *Lasers*. Mill Valley, California: University science books, 1986.

[51] D. Allan, 'Statistics of atomic frequency standards', en, *Proceedings of the IEEE*, vol. 54, no. 2, pp. 221–230, 1966, ISSN: 0018-9219. DOI: 10.1109/PROC.1966.4634.

[52] W. Riley and D. A. Howe, 'Handbook of frequency stability analysis', en, *NIST*, Jul. 2008, Last Modified: 2021-10-12T11:10-04:00. [Online]. Available: https://www.nist.gov/publications/handbook-frequency-stability-analysis.

[53] L.-S. Ma, P. Jungner, J. Ye and J. L. Hall, 'Delivering the same optical frequency at two places: Accurate cancellation of phase noise introduced by an optical fiber or other time-varying path', EN, *Optics Letters*, vol. 19, no. 21, pp. 1777–1779, Nov. 1994, ISSN: 1539-4794. DOI: 10.1364/OL.19.001777.

[54] J. Ye *et al.*, 'Delivery of high-stability optical and microwave frequency standards over an optical fiber network', *Journal of the Optical Society of America B-optical Physics*, vol. 20, no. 7, pp. 1459–1467, Jul. 2003.



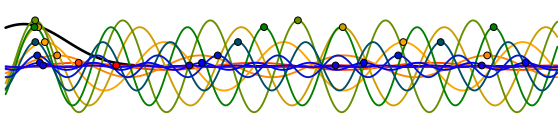

[55] S. M. Foreman, A. D. Ludlow, M. H. G. de Miranda, J. E. Stalnaker, S. A. Diddams and J. Ye, 'Coherent optical phase transfer over a 32-km fiber with 1 s instability at 10(-17)', *Physical Review Letters*, vol. 99, pp. 153 601–, 2007.

[56] S. Droste *et al.*, 'Optical-frequency transfer over a single-span 1840 km fiber link', *Physical Review Letters*, vol. 111, no. 11, p. 110 801, Sep. 2013. DOI: 10.1103/PhysRevLett.111.110801.

[57] Bengtsson, Alexander, *Experimental Implementation of a Fiber Noise Cancellation System for Slow Light Laser Locking*, eng, Master's thesis, 2017.

[58] M. Afzelius and C. Simon, 'Impedance-matched cavity quantum memory', *Physical Review A*, vol. 82, no. 2, p. 022 310, Aug. 2010.

[59] MyCryoFirm, *On-site test protocol*, 19th Oct. 2020.

[60] D. Schroeder, J. Deschamps, A. Dasgupta, U. Matti and J. Ries, 'Cost-efficient open source laser engine for microscopy', English, *Biomedical Optics Express*, vol. 11, no. 2, pp. 609–623, Feb. 2020, ISSN: 2156-7085. DOI: 10.1364/BOE.380815.

[61] M. Pomponio, A. Hati and C. Nelson, 'FPGA-based low-latency digital servo for optical physics experiments', in *2020 Joint Conference of the IEEE International Frequency Control Symposium and International Symposium on Applications of Ferroelectrics (IFCS-ISAF)*, Jul. 2020, pp. 1–2. DOI: 10.1109/IFCS-ISAF41089.2020.9234889.

[62] Renders, Antonius Johannes, *Distortion and attenuation free gain-assisted Superluminal Propagtion in a Rare-Earth Doped Crystal*, Master's thesis, 2023.

# Scientific publications

## Author contributions

### Paper I: Slow light frequency reference cavities—proof of concept for reducing the frequency sensitivity due to length fluctuations

This paper was based primarily on two experimental runs. The first of these was underway when I joined the group, and I partook as an active observer.

For the second of these experimental runs I was involved in planning and preparations, performing preliminary calculations and simulations, as well as physically preparing the sample. The experimental work was conducted jointly by me and the first author, and I provided input and revision during the preparation of the manuscript.

### Paper II: Using slow light to enable laser frequency stabilization to a short, high-Q cavity

Manuscript submitted for publication.

This paper was primarily authored by me, based on several experiments prepared and performed by me and co-authors over the previous 4 years. I performed calculations and simulations for the requirements on the sample, locking electronics, and optics, developed some of the instrumentation and headed the analysis.



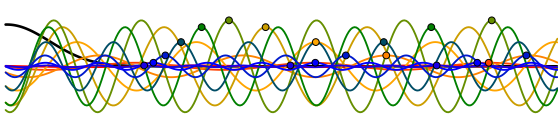

### Paper III: Highly tuneable in-situ cryogenic switch bank resonator for magnetic field generation at radio-frequencies

Manuscript in preparation.

I was involved in the design of the instrument under study, and took part in several preparatory and evaluative experiments. I provided comments and feedback to the analysis and the preparation of the manuscript.

### Paper IV: Resetting spectral hole features in Eu:YSO using a highly tunable radio-frequency resonance circuit

Manuscript in preparation.

The experiments for this article were an integrated part of the slow light experiment, and I was involved in planning, execution, and analysis. I provided comments and feedback to the analysis and the preparation of the manuscript.

### Paper V: Pushing the limits of negative group velocity

Manuscript submitted for publication.

The experiments for this paper were performed as part of the main author's master's thesis ([62]). As assistant thesis supervisor, I was involved from planning to analysis. Many of the techniques involved were developed by me as part of the slow light project. I provided comments and feedback during the preparation of the manuscript.

# Paper I

S. P. Horvath, C. Shi, D. Gustavsson, A. Walther, A. Kinos, S. Kröll and L. Rippe "Slow light frequency reference cavities—proof of concept for reducing the frequency sensitivity due to length fluctuations", *New Journal of Physics* (2022)

IOP Publishing New J. Phys. 24 (2022) 033034 https://doi.org/10.1088/1367-2630/ac5932

New Journal of Physics
The open access journal at the forefront of physics

Deutsche Physikalische Gesellschaft DPG
IOP Institute of Physics
Published in partnership with: Deutsche Physikalische Gesellschaft and the Institute of Physics

OPEN ACCESS

RECEIVED
26 November 2021

REVISED
20 February 2022

ACCEPTED FOR PUBLICATION
28 February 2022

PUBLISHED
23 March 2022



PAPER

# Slow light frequency reference cavities—proof of concept for reducing the frequency sensitivity due to length fluctuations

**Sebastian P Horvath[1], Chunyan Shi[2], David Gustavsson, Andreas Walther, Adam Kinos, Stefan Kröll and Lars Rippe***

Department of Physics, Lund University, PO Box 118, SE-22100 Lund, Sweden
* Author to whom any correspondence should be addressed.
[1] Current address: Department of Electrical Engineering, Princeton University, Princeton, NJ, United States of America.
[2] Current address: Zurich Instruments, Technoparkstrasse 1, Zürich, Switzerland.

**E-mail:** physics@rippe.se

**Keywords:** slow-light effect, rare-earth ion doped crystals, laser frequency stabilization

## Abstract

Length changes due to thermo-mechanical noise originating from, for example, Brownian motion are a key limiting factor of present day state-of-the-art laser frequency stabilization using Fabry–Pérot cavities. We present a laser-frequency stabilization concept using an optical cavity with a strong slow-light effect to reduce the impact of cavity length changes on the frequency stability. The resulting noise-reduction factor is proportional to the ratio between the light phase and group velocities in the highly dispersive cavity spacer. We experimentally demonstrate a proof-of-principle implementation of this laser-frequency stabilization technique using a rare-earth doped crystalline cavity spacer in conjunction with semi-permanent spectral tailoring to achieve precise control of the dispersive properties of the cavity. Compared to the same setup in the absence of the slow-light effect a reduction in frequency sensitivity of four orders of magnitude was achieved.

## 1. Introduction

Precision frequency stabilized lasers are a fundamental component of modern metrology. They serve as a local oscillator in optical atomic clocks [1], and are at the heart of interferometer based tests of fundamental physics, such as gravitational wave detection [2] and tests of relativity [3, 4]. State-of-the-art frequency stabilization is performed using Fabry–Pérot (FP) cavities in conjunction with the Pound–Drever–Hall (PDH) locking technique. In order to achieve good performance, thermo-mechanical isolation of the cavity, along with a careful material selection, is imperative. Typical cavities, with a length on the order of 10 cm, have a fractional stability of $10^{-15}$ [5–7].

Present day leading stabilities are achieved by utilizing long cavities ($\sim$ 50 cm), with a fractional stability of $8 \times 10^{-17}$ [8], or cryogenically cooling single-crystal silicon cavities, with a fractional stability of $4 \times 10^{-17}$ [9]. Such designs have been shown to operate at the frequency stability limit imposed by the thermo-mechanical noise in the mirror coatings [9, 10]. In addition to utilizing long cavities [8, 11], or operating single-crystal cavities at cryogenic temperatures [9, 12, 13], investigations to reduce the thermo-mechanical noise originating from the mirror coatings has focused on increasing the size of the optical mode [14], as well as utilizing single-crystal mirrors with low dielectric losses [15, 16].

While the fractional stability has been considerably improved over the last decade by refining cavity designs, the thermo-mechanical noise limit of FP cavities has prompted investigations into alternative stabilization techniques including cavity quantum-electrodynamic systems [17–19] and locking to spectral holes in rare-earth ion doped crystals [20–27].

The slow-light effect consists of a reduction of the group velocity of light in a medium due to a sharp gradient in the dispersion. This effect has been successfully utilized in conjunction with optical cavities to demonstrate a reduced sensitivity of the cavity resonance to length changes as well as a narrowing of the

IOP Publishing New J. Phys. 24 (2022) 033034 S P Horvath et al

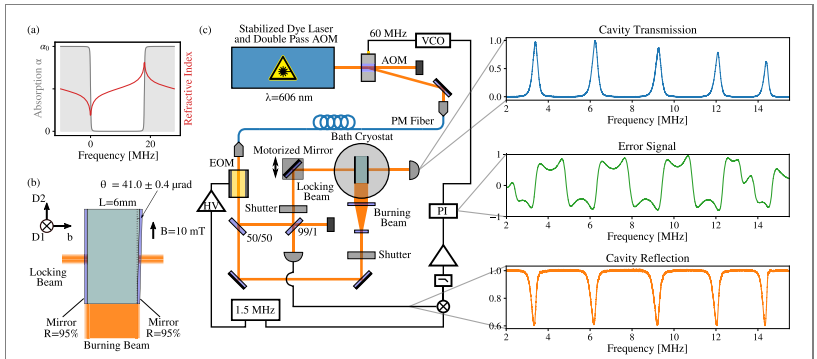


**Figure 1.** (a) Schematic of a spectral hole and the resulting rapidly varying dispersion across this frequency region. (b) Schematic of the crystal geometry, showing the burning beam perpendicular to the locking beam. (c) The experimental layout of the core laser-locking setup, with representative signals observed at key locations in the locking loop. The EOM modulation was disabled to record the cavity transmission and reflection signals. The steep gradient visible in the error signal at frequencies where there is no peak in the reflection signal originates from the large modulation used (1.5 MHz, which is almost half of the cavity mode spacing). For a detailed description of these signals in the context of PDH locking, see reference [31].

cavity linewidth [28–30]. In this work we demonstrate the locking of a laser to a slow-light cavity, harnessing both the reduced sensitivity to length changes as well as the cavity linewidth narrowing.

The cavity is constructed using a rare-earth ion doped crystal with mirror coatings directly deposited on the crystal surfaces. By spectral tailoring, a narrow semi-permanent frequency transmission window is burned into the inhomogeneously broadened rare-earth ion ensemble. The narrow transmission window leads to a gradient of the index of refraction across the spectral window, which reduces the speed of light in the cavity by up to four orders of magnitude (see figure 1(a)). Such an effect has been previously demonstrated to lead to a narrowing of the cavity-linewidth by a factor comparable to the reduction of the speed of light [30].

The slow-light effect increases the cavity round-trip time, which, heuristically, can be thought of as an increase of the effective cavity length from 6 mm to 60 m. Therefore, this technique enables designs with a very large effective length without the mechanical degradation associated with a physically longer cavity. More concretely, assuming an inhomogeneously broadened ensemble with an absorption $\alpha_0$ and a square spectral transmission window, as indicated in figure 1, the cavity free-spectral range (FSR) has the form

$$\nu_{\mathrm{FSR}} = \frac{v_{\mathrm{g}}}{2L} = \frac{1}{2L}\frac{\pi^2\Gamma}{\alpha_0} = \frac{c}{2L}\frac{1}{n + \nu\frac{\mathrm{d}n}{\mathrm{d}\nu}}. \tag{1}$$

Here, $v_{\mathrm{g}}$ is the group velocity of light, $L$ is the cavity length, $\Gamma$ is the transparency window width, $c$ is the speed of light, $n$ is the refractive index, and $\nu$ the frequency of the light; a derivation of this relation is provided in appendix B. Note that the above equation is only valid at the center of the transparency window; nevertheless, since the dispersive gradient is close to constant across a large portion of the transparency window, equation (1) is a good approximation for all cavity modes not adjacent to the edges.

The slow-light effect not only reduces the cavity FSR, but equally scales the cavity linewidth $\delta\nu_{\mathrm{cav}}$. Assuming a high-finesse cavity with only small mirror losses [32], one finds

$$\delta\nu_{\mathrm{cav}} = \frac{\nu_{\mathrm{FSR}}}{\mathcal{F}} = \frac{v_{\mathrm{g}}}{2L}\left(\frac{T_1 + T_2 + 2\alpha_{\mathrm{c}}L}{2\pi}\right). \tag{2}$$

Here, $\mathcal{F}$ is the cavity finesse, $\alpha_{\mathrm{c}}$ is the residual absorption at the center of the transparency window due to off-resonant excitation, while $T_1$ and $T_2$ are the transmission of the first and second mirror. From equations (1) and (2) it is apparent that the finesse $\mathcal{F}$ is independent of the slow-light effect.

In addition to a narrowing of the cavity modes, the slow-light effect also results in an insensitivity to cavity-length changes. By considering the relative frequency shift due to a cavity length change, one obtains

$$\frac{\mathrm{d}\nu}{\nu} = -\frac{\mathrm{d}L}{L}\frac{v_{\mathrm{g}}}{c}. \tag{3}$$

IOP Publishing New J. Phys. 24 (2022) 033034 S P Horvath et al

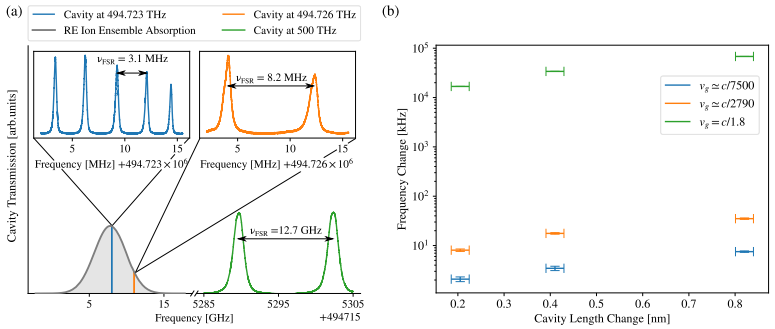


**Figure 2.** (a) Representative cavity modes observed at three distinct frequencies relative to the inhomogeneously broadened rare-earth ion absorption profile. Colors designate the cavity frequency: blue is at maximum absorption, orange is detuned from the maximum absorption by 3 GHz, and green is far away from the absorption peak, detuned by $\simeq$ 5.3 THz, which is sufficient to ensure that the slow-light effect is negligible. The inhomogeneous line, shown in gray, has an FWHM of $\simeq$ 5 GHz, determined by an absorption measurement in a portion of the crystal that was not mirror coated. The frequencies of the two insets relative to the inhomogeneous profile are indicated using the blue and orange vertical bars. (b) The frequency sensitivity to cavity length changes at the previously enumerated cavity frequencies (see figure 1 for the experimental configuration). The blue and orange measurements were performed with the laser locked to the slow-light cavity, while the green measurements were performed by directly measuring the shift of the cavity modes due to the induced length changes. See text for further details. The indicated group velocities were determined from the change of the cavity FSR. The frequency sensitivity can be seen to scale with $v_g$; any deviation from an exact correspondence is attributed to a deviation from an optimally square spectral transparency window.

The same scaling with respect to $v_g$ is true for the frequency noise amplitude $\sqrt{S_\nu}$ resulting from a corresponding displacement noise amplitude. As a consequence, all optical length-change noise sources, including from the mirror coatings, are reduced by a factor corresponding to the group velocity divided by the speed of light.

## 2. Experimental results

The proof-of-principle implementation utilized a $Pr^{3+}$:$Y_2SiO_5$ crystal as a spacer material for an FP cavity with mirror coatings applied directly to two, almost parallel, flat crystal surfaces. While a better ultimate stability could be achieved by utilizing a material with a narrower optical homogeneous linewidth and slower hyperfine relaxation rate, the present demonstration of this locking technique was implemented in $Pr^{3+}$:$Y_2SiO_5$ due to the well established spectral-tailoring routines available for this material [33]. An optical transmission window was burned at 494.723 THz, on resonance with the $^3H_4 \rightarrow {}^1D_2$ transition of $Pr^{3+}$ ions. The geometry utilized for spectral hole burning with respect to the crystal orientation and the mirror coatings is shown in figure 1(b).

Figure 1(a) schematically shows the spectral transmission window and the corresponding change in refractive index. The gradient of the dispersion leads to, in accordance with equations (1) and (2), a reduction in both the cavity mode spacing and the linewidth $\delta\nu_{cav}$. The group velocity of light propagating through the transparency window scales inversely with the absorption, $\alpha_0$, outside the transparency window; therefore, the cavity mode linewidth is strongly dependent on the frequency of the spectral hole with respect to the $Pr^{3+}$ inhomogeneous line. This is illustrated in figure 2(a), which shows the transmission cavity modes for three scenarios with different values for $\alpha_0$. Specifically, a spectral transmission window with a width of 18 MHz was burned at the center of the $Pr^{3+}$ ensemble, as well as detuned from the center by 3 GHz. This yielded a full width at half maximum (FWHM) cavity mode linewidth of 275 $\pm$ 2 kHz and 745 $\pm$ 14 kHz, respectively. In contrast, the cavity linewidth obtained when the laser was detuned by $\simeq$ 5.3 THz, where we expect any absorption from $Pr^{3+}$ ions to be negligible, was 1317 $\pm$ 2 MHz.

In order to test the reduction in frequency sensitivity to cavity length changes, and consequently corroborate equation (3), a small relative angle between the mirror coated sides of the $Pr^{3+}$:$Y_2SiO_5$ crystal was exploited. This angle is schematically shown in figure 1(b), and amounted to a relative slope of 41.0 $\pm$ 0.4 $\mu$rad. The cavity input beam was equipped with a motorized mirror mount, such that, when the input beam was translated along the slope, the cavity length was changed by a calibrated amount. Consequently, by translating the input beam while monitoring the resulting cavity frequency shift for the

IOP Publishing New J. Phys. 24 (2022) 033034 S P Horvath et al

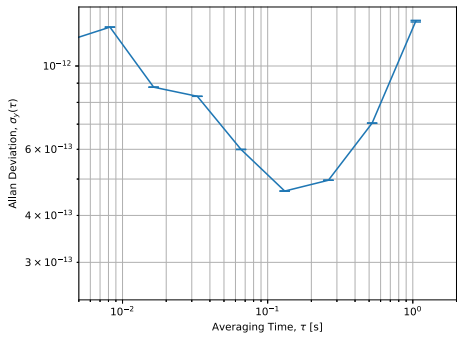


**Figure 3.** Overlapped Allan deviation with linear drift subtracted [34]. The noise floor was found to be $\sigma_y(\tau) = 4.6 \times 10^{-13}$ at an averaging time of 130 ms.

three distinct slow-light regimes described above (see figure 2(a)), it was possible to probe the impact of the slow-light effect on the frequency shift as a function of length change. More specifically, in order to determine the cavity mode frequency shift when the laser was on resonance with the $Pr^{3+}$:$Y_2SiO_5$ inhomogeneous profile, as well as when it was detuned by 3 GHz, the PDH technique was employed [31]. A pre-stabilized laser was passed through an acousto-optic modulator (AOM) followed by a PDH lock to the slow-light cavity, as shown in figure 1(c); a detailed experimental description is provided in appendix A. The PDH feedback signal was applied to the AOM to create a closed loop. Monitoring the feedback signal thus provided a high-resolution measurement of the stability and drift attainable by the slow-light cavity. To ensure the locking beam propagated within a spectral hole throughout the translation, a spatial region of the crystal surrounding the locking beam was spectrally tailored using a large burning beam perpendicular to the locking beam.

This measurement was repeated for three different translation step sizes. For each step size, the experiment was cycled 10 times, and the resulting frequency shift averaged. By performing this measurement both at the center of the inhomogeneous $Pr^{3+}$ ensemble, as well as detuned by 3 GHz, the dependence of the induced frequency change could be determined with respect to the slow-light effect. These measurements are shown in figure 2(b) for, respectively, the group velocities of $v_g \simeq c/7500$ and $v_g \simeq c/2790$. The frequency shift for each step size was also determined in the absence of the slow-light effect by detuning the laser by $\simeq 5.3$ THz. However, due to the large increase in the cavity FSR, bandwidth limitations precluded the use of the PDH method outlined above. The frequency change was instead determined by directly measuring the cavity modes in transmission before and after each translation step (see appendix F for further details). These measurements are also included in figure 2(b), denoted by the speed of light in $Y_2SiO_5$ of $v_g = c/1.8$. We note that this last measurement was also used to calibrate the angle of the crystal.

This measurement shows that the frequency shift due to length changes scales proportionally with the group velocity, and achieves a reduction in length-change sensitivity of almost four orders of magnitude at the center of the $Pr^{3+}$ ensemble. From this measurement, the minimal drift rate of our locking setup was found to be $0.55 \pm 0.06$ kHz $s^{-1}$. The principal limiting factors for these experiments, as will be discussed in detail below, originated from two distinct sources of atomic drift. Furthermore, the locking loop included a single-mode fiber which did not include any Doppler noise cancellation. Figure 3 shows the overlapped Allan deviation after linear drift subtraction [34], with a noise floor of $\sigma_y(\tau) = 4.6 \times 10^{-13}$ at an averaging time of 130 ms. One possible explanation for this limit could be the polarization-maintaining fiber that is part of the locking loop (see figure 1) which for a 25 m fiber has been shown to lead to frequency broadening up to ∼1.2 kHz [35].

To further analyze the drift, the laser was locked to different cavity modes across the transmission window. This revealed two unique sources for the frequency drift: off-resonant excitation, and hyperfine cross-relaxation. Specifically, the circulating light in the cavity will off-resonantly excite ions at the high and low frequency edges of the spectral transmission window, which then have a non-negligible probability of relaxing to a different hyperfine level. Ions excited from the high-energy edge in figure 4(a) predominantly reside in the $|\pm 5/2g\rangle$ state. When excited they can decay to the $|\pm 1/2g\rangle$ or $|\pm 3/2g\rangle$ states. This transfer can, effectively, be considered as a shift of the spectral transmission window. As a consequence, the

IOP Publishing New J. Phys. 24 (2022) 033034 S P Horvath et al

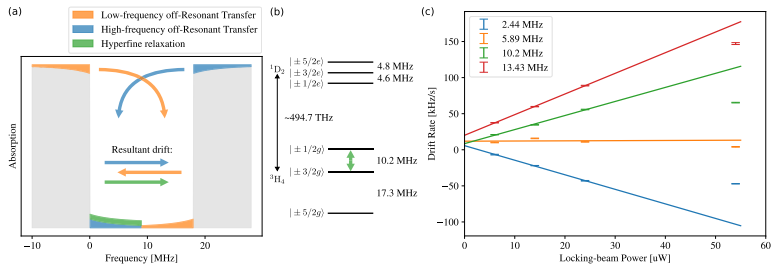


**Figure 4.** (a) Changes in absorption in the spectral transmission window during locking and the resulting drift. Blue and orange shaded regions indicate off-resonant excitation and subsequent relaxation into the transmission window. The green shaded region is the result of direct hyperfine level-cross relaxation and occurs primarily at the low frequency side of the transmission window. (b) The energy level diagram of the $Pr^{3+}$:$Y_2SiO_5$ ground and excited state; the green arrow indicates the most likely hyperfine cross-relaxation pathway. (c) The locked laser drift rate, relative to the stabilized reference laser, when locked at different frequencies with respect to the center of the spectral transmission window. The non-linear effect for the higher locking intensity data is attributed to a re-burning of the spectral transmission window by the locking beam.

dispersion curve within the spectral transmission window translates to higher frequencies, which also shifts the cavity modes toward higher frequencies. This process is counteracted by the off-resonant excitation of ions at the low energy edge of the transmission window in figure 4(a). Here, ions occupy the $|\pm 1/2g\rangle$ state (see figure 4(b)), but may, when they are excited, fall down in either the $|\pm 3/2g\rangle$ or $|\pm 5/2g\rangle$ states, effectively leading to a negative shift of the cavity modes. These two cases of positive and negative frequency drift are indicated by the blue and orange shaded regions in figure 4(a).

The second source of drift stems from the hyperfine relaxation between the $|\pm 1/2g\rangle$ state and the $|\pm 3/2g\rangle$ state. Relaxation from $|\pm 1/2g\rangle$ to $|\pm 3/2g\rangle$ results in absorption at low frequencies of the spectral transmission window; consequently, the cavity modes drift to higher frequencies. This is indicated by the shaded green region in figure 4(a). Figure 4(c) shows the drift with respect to different locking beam intensities. The hyperfine relaxation rate is independent of the locking beam intensity, and therefore leads to a constant positive offset in the drift rate.

The data summarized in figure 4(c) establishes that, in general, the drift due to off-resonant excitation depends on the locking beam intensity and the frequency position of the cavity mode relative to the transparency window. At high locking intensities, the drift becomes non-linear due to a re-burning of the spectral transmission window by the locking beam. The only point where there is no clear power dependence is for the 5.89 MHz locking point. Here the constant drift is solely due to hyperfine cross-relaxation, which demonstrates that the drift due to the low and high frequency off-resonant excitation can be canceled. The drift may be mitigated by carefully positioning the cavity mode at the center of the transparency window and choosing a material with negligible hyperfine cross-relaxation during practical locking timescales. This can be realized by utilizing $Eu^{3+}$:$Y_2SiO_5$, for which persistent spectral holes have been observed for up to 50 days after creation [36]. The relative position of the cavity mode within the transparency window can be fine tuned by moving the window within the inhomogeneous profile.

While this demonstrates that it is possible to mitigate the observed drift with a carefully selected locking point and material selection, off resonant excitation will nevertheless slowly degrade the spectral structure and therefore impair the attainable slow-light effect after extended locking periods. The magnitude of this effect is determined by the optical power circulating in the cavity, and therefore requires a careful selection of locking parameters. This is discussed in detail below, where we perform an estimate of the attainable stability for an optimized slow-light cavity. Finally, we note that even when locked to a cavity mode that cancels drift due to off-resonant excitation, any absolute drift in the resonance frequency of the ions is nevertheless a source of noise for a locked laser. In particular, ambient pressure and temperature changes have been determined to impact spectral-hole locking techniques [37], and are likely also key limiting sources of drift for the presented locking technique. However, to our knowledge, this ultimate atomic limit has yet to be achieved by any of the rare-earth ion based laser frequency stabilization techniques presently under investigation [24, 27].

IOP Publishing New J. Phys. 24 (2022) 033034 S P Horvath et al

## 3. Discussion

We now discuss several factors which impact the performance of a slow-light cavity. In order to describe these factors, it is necessary develop several prerequisites which are interesting in their own right. The integrated off-resonant absorption at the center of a spectral transmission window can be approximately expressed as

$$\alpha_c \simeq \frac{2}{\pi}\frac{\Gamma_h}{\Gamma}\alpha_0. \tag{4}$$

Here, $\alpha_0$ is the absorption outside the transmission window, $\Gamma_h$ is the homogeneous linewidth of the ions, and $\Gamma$ is the transmission window width [38]. Substituting equation (4) into equation (2), and using the expression for $v_g$ in terms of $\alpha_0$ and $\Gamma$ given by equation (1), it is straightforward to show that the cavity linewidth takes the form

$$\delta\nu_{cav} \simeq \Gamma_h + \frac{\pi\Gamma(T_1+T_2)}{4\alpha_0 L}. \tag{5}$$

Considering, for simplicity, the case of an impedance matched cavity, that is, imposing the requirement that $T_1 = 2\alpha_c L$, and an output mirror transmission approaching zero, the above equation reduces to

$$\delta\nu_{cav} \simeq 2\Gamma_h. \tag{6}$$

Interestingly, in this scenario the linewidth is, to first order, independent of the cavity length, absorption coefficient, and the transmission window width (provided the cavity mirrors are adjusted to maintain impedance matching); the linewidth is entirely determined by the homogeneous linewidth of the active resonant absorber ions.

Relating the cavity mode linewidth to the Allan deviation, one obtains

$$\sigma_y(\tau) = \frac{1}{\sqrt{2\tau}}\frac{1}{4}\sqrt{\frac{h\nu}{P_c}}\delta\nu_{cav}, \tag{7}$$

where $P_c$ is the shot-noise limited locking power, $\tau$ the locking time, $\nu$ the locking frequency, and $h$ corresponds to Planck's constant (see appendix C for a derivation). Consequently, this equation can be used to determine the requisite optical power for a given Allan deviation. Substitution of equation (6) further establishes that the material homogeneous linewidth directly fixes the necessary circulating optical power, and, as discussed above, the impact of off-resonant excitation. Considering for concreteness $Eu^{3+}$:$Y_2SiO_5$, the homogeneous linewidth is 200 Hz [39] compared to 2.5 kHz for $Pr^{3+}$:$Y_2SiO_5$ [40]. From equation (6) it can be seen that this would allow for a cavity mode width of 1 kHz, even when including a reasonable margin for experimental imperfections. Substituting this into equation (7), and setting a target Allan variance of $1\times10^{-17}$ for a 1 s measurement time, one obtains $\approx 0.4$ nW for the shot noise limited locking power. In appendix E we evaluate the rate of off-resonant excitation resulting from a given circulating locking power and the impact on the attainable locking time. For a power of $\approx 0.4$ nW this yields a lower bound of more than 2 h. While there may be additional unforeseen limits that impact the ultimately attainable frequency stability, a determination of this limit requires an experimental investigation of the demonstrated locking technique using a narrow homogeneous linewidth material such as $Eu^{3+}$:$Y_2SiO_5$.

A corollary of equation (6) is that for an impedance matched cavity the narrowest achievable cavity linewidth is not affected by the slow-light effect. Intuitively this can be understood as follows: by narrowing the transparency window width $\Gamma$ the group velocity can be reduced, and in accordance with equation (2), the cavity linewidth narrows. However, this leads to an increase in the off-resonant absorption $\alpha_c$ at the center of the transparency window, which, in order to maintain impedance matching, requires an increase of the input mirror transmission $T_1$. While this might suggest that the narrowest transparency window achievable for a given material $\Gamma_h$ is optimal in order to maximize the reduction in length change sensitivity, such an optimization impairs the longest attainable locking period. In particular, the off-resonant excitation width extending into the ions adjacent in frequency to the spectral transparency window scales with the width $\Gamma$. Specifically, 50% of the absorption at the center of the spectral window comes from the atoms in the intervals $[-\Gamma, -\Gamma/2]$ and $[\Gamma/2, \Gamma]$ (see appendix D for further details). Thus, the width $\Gamma$ determines the number of ions interrogated by the circulating light of the cavity, and consequently, the number of ions over which any deterioration of the spectral structure is averaged. Broadening the transparency window width increases the time that the spectral structure can be maintained, and, consequently, the amount of time that the slow-light cavity can be locked.

At its core, this trade-off between the optical power used to interrogate the atomic ensemble, spread over the finite spectral width of the ensemble, is true for all rare-earth ion based laser stabilization techniques. For spectral-hole locking, the equivalent averaging takes place when one performs interleaved locking to a

large number of individual spectral holes [22]; however, the total number of interrogated ions for implementations realized to date is considerably fewer than for the technique presented here.

An additional potential noise source for the presented locking technique that is not an issue for conventional FP cavities are changes of the refractive index of the cavity spacer material due to environmental variations in temperature and pressure. Noise of this type is also reduced by the slow-light effect according to

$$\frac{\mathrm{d}\nu}{\nu} = -\frac{\mathrm{d}n}{n}\frac{v_\mathrm{g}}{c}, \tag{8}$$

with $n$ the refractive index of the spacer. A detailed analysis of this is beyond the scope of the present paper, and the order of magnitude where this will become significant in a material such as $Eu^{3+}$:$Y_2SiO_5$ is yet to be determined. Ultimately, like with any locking setup, there will be a wide range of environmental factors that impair the stability, such as temperature, pressure, and vibration. The impact of some of these will be reduced by the slow-light effect similar to what has been demonstrated here for cavity length changes, although this will not hold true universally for all noise sources. A detailed noise analysis of this locking scheme will be reported in a subsequent work.

## 4. Conclusion

We have presented a laser frequency stabilization technique that utilizes the slow-light effect within an FP cavity to reduce the sensitivity of the resonance frequencies to cavity length changes. Implementing such a locking system using a single-crystal $Pr^{3+}$:$Y_2SiO_5$ cavity spacer achieved a reduction in length change sensitivity by four orders of magnitude. The concept validation of this system achieved a drift rate of $0.55 \pm 0.06$ kHz $s^{-1}$ with a noise floor of $\sigma_y(\tau) = 4.6 \times 10^{-13}$ for a 6 mm long cavity. We have theoretically demonstrated that a different material with narrower homogeneous linewidth and lower hyperfine cross-relaxation should significantly improve these values, and the case of $Eu^{3+}$:$Y_2SiO_5$, which entails more complex spectral tailoring, is presently under active investigation.

## Acknowledgments

The authors would like to thank Ulf Söderlund and Leif Johansson for their help with dicing the $Pr^{3+}$:$Y_2SiO_5$ crystal. This research was supported by the Swedish Research Council (Nos. 2016-05121, 2015-03989, 2016-04375, and 2019-04949), the Knut and Alice Wallenberg Foundation (KAW 2016.0081), the Wallenberg Center for Quantum Technology (WACQT) funded by The Knut and Alice Wallenberg Foundation (KAW 2017.0449), the Royal Physiographic Society in Lund, and the European Union FETFLAG program, Grant No. 820391 (SQUARE) (2017.0449).

## Data availability statement

The data that support the findings of this study are available upon reasonable request from the authors.

## Appendix A. Experimental details

The laser used was a Coherent 699-21 ring-dye laser, with a custom intra-cavity EOM, stabilized to an external ULE cavity. The linewidth is estimated to be on the order of a few tens of Hz, with a drift rate below 1 Hz $s^{-1}$ [41]. Prior to injection of the light into the locking loop, arbitrary pulse shaping in amplitude, frequency, and phase, was performed with a double-pass AOM. Locking was performed using the PDH technique, with a modulation frequency of 1.5 MHz. To verify that a tight lock was achieved, the pre-stabilized laser was stepped through a series of frequency changes while the feedback loop was monitored. The sample was cooled to 2.1 K in an Oxford Instruments bath cryostat. The $Y_2SiO_5$ crystal has yttrium atoms replaced with praseodymium at a 500 ppm level; the sample is a cylinder of diameter 10 mm and a height of 6 mm (purchased from Scientific Materials). One side of the cylinder has been cut and polished to allow for the perpendicular burn geometry indicated in figure 1(c). The polarization of both the burn and probe light was rotated to be parallel to the $D_2$ optical extinction axis of $Y_2SiO_5$, which has an absorption depth of $47 \pm 5$ $cm^{-1}$ [42]. The width of the spectral transmission window used throughout was 18 MHz.

All measurements, with the exception of the drift rate with respect to locking point, were performed with a magnetic field of 10 mT along the crystal $D_2$ axis, which enhanced the lifetime of the ground-state

IOP Publishing New J. Phys. 24 (2022) 033034 S P Horvath et al

hyperfine levels. Moreover the drift rate data was taken in a configuration without the perpendicular burn-beam geometry; consequently burning was performed through the mirror coating. While this impaired the absolute drift performance, it still demonstrated the trends of the drift vs intensity when locking to different cavity modes.

In order to perform the beam-translation experiment, and to achieve optimal burning, the perpendicular burn geometry was utilized. The burn beam was shaped with cylindrical lenses and blocked with a mechanical shutter during locking. To avoid standing waves during burning, a second shutter blocked the locking beam during the burn operation. Additionally, for the measurements of the smallest drift rate, as well as the noise floor, the burning beam was dithered with a piezo driven mirror mount with a frequency of 10 Hz, and a lens tissue paper inserted into the beam path before the cryostat window. By making the burning beam more diffuse, this ensured optimal burning of the entire length of the crystal (including close to the mirror coated sides), and mitigated residual drift from unburned spatial regions of the crystal because of (partial) standing waves arising from reflections of the parallel crystal surfaces. The error signal was amplified and 30 kHz low-pass filtered prior to locking with a Vescent D2-125.

## Appendix B. Group-velocity in spectral transparency window

To derive the group velocity for a pulse of light traveling through a rectangular spectral transmission window we follow the method suggested by Chanelière [43, 44]. We note that, for a weakly-absorbing host with refractive index $n_0$, doped by an absorbing species, the imaginary component of the first order susceptibility reads [45]

$$\chi''(\omega) = -\frac{n_0 G(\omega)}{k_0}. \tag{B1}$$

Here, $G(\omega)$ is spectral absorption lineshape, $k_0 = \omega_0/c$, $\omega_0$ is the central angular frequency of the inhomogeneous absorption profile, which is assumed to be coincident with the center of the spectral transparency window, and $c$ is the vacuum speed of light. By application of the Kramers–Kroniger relation, the real part of the first order susceptibility can be evaluated from equation (B1) using

$$\chi'(\omega) = \frac{1}{\pi}\,\mathrm{P.V.}\int_{-\infty}^{\infty}\frac{\chi''(\omega')}{\omega-\omega'}\mathrm{d}\omega', \tag{B2}$$

where P.V. denotes the Cauchy principal value. For a square spectral transmission window of width $\Gamma$ (in units of frequency), which is much narrower than the inhomogeneous absorption profile, the transparency window can be approximated by

$$G'(\omega) = \alpha_0(1-\Pi(\omega)). \tag{B3}$$

Here, $\alpha_0$ is the peak absorption outside the transparency window and $\Pi(\omega)$ is the rectangular function defined by

$$\Pi(\omega) = \begin{cases} 0, & |\omega-\omega_0| > \pi\Gamma \\ 1/2, & |\omega-\omega_0| = \pi\Gamma. \\ 1, & |\omega-\omega_0| < \pi\Gamma \end{cases} \tag{B4}$$

When directly evaluated, the integral equation (B2) is manifestly divergent. This divergence could be alleviated by convolving $G'(\omega)$ with an inhomogeneous absorption lineshape such as a Gaussian; however, the resulting integral is difficult to evaluate analytically. To circumvent this, we note that the integral equation (B2) for a flat distribution can be shown to be zero (that is, for a perfectly flat absorption profile, the dispersion is zero). Consequently,

$$\int_{-\infty}^{\infty} G'(\omega)\mathrm{d}\omega = \int_{-\infty}^{\infty} -G(\omega)\mathrm{d}\omega, \tag{B5}$$

where $G(\omega) = \alpha_0\Pi(\omega)$.

Substituting the appropriate terms into equation (B2), one obtains,

$$\begin{aligned}\chi' &= \frac{1}{\pi}\frac{\alpha_0 n_0}{k_0}\,\mathrm{P.V.}\int_{-\infty}^{\infty}\frac{\Pi(\omega')}{\omega-\omega'}\,\mathrm{d}\omega' \\ &= \frac{1}{\pi}\frac{\alpha_0 n_0}{k_0}\,\ln\left(\frac{\omega_0-\pi\Gamma-\omega}{\omega_0+\pi\Gamma-\omega}\right),\end{aligned} \tag{B6}$$

IOP Publishing New J. Phys. 24 (2022) 033034 S P Horvath et al

where the integration was evaluated using the Hilbert transform for a rectangular function [46]. To determine the group velocity at the center of the spectral transparency window, we observe that

$$v_g = \frac{c}{n + \omega \frac{dn}{d\omega}}, \tag{B7}$$

where

$$n = n_0 + \frac{\chi'}{2n_0}. \tag{B8}$$

Series expanding $v_g$ around the central frequency $\omega_0$ yields, to first order,

$$v_g = \frac{\pi^2 \Gamma}{\alpha_0}, \tag{B9}$$

where we have also made use of the assumption that $n \ll \omega \frac{dn}{d\omega}$. Substituting this result for the group velocity into standard FP cavity equations yields (1).

## Appendix C. Shot-noise limited power estimate

The shot-noise limited power for a slow-light cavity is identical to that for a conventional PDH locked cavity. Following Black [31], the spectral density of shot noise has the form

$$S_e = \sqrt{2\frac{hc}{\lambda}(2P_s)}, \tag{C1}$$

and the corresponding frequency noise reads

$$S_f = \frac{S_e}{|D|}, \tag{C2}$$

where

$$D = -\frac{8\sqrt{P_c P_s}}{\delta\nu_{cav}}. \tag{C3}$$

Here $P_c$ and $P_s$ correspond to the carrier and side-band powers, $\nu_{cav}$ is the cavity linewidth, and the remaining variables have their usual meanings. This yields the apparent frequency noise with respect to locking power and the cavity linewidth

$$S_f = \frac{1}{4}\sqrt{\frac{h\nu}{P_c}}\delta\nu_{cav}. \tag{C4}$$

For white frequency noise (shot noise) the one-sided noise spectral density $S_y(t)$ has the form

$$S_y(t) = h_0, \tag{C5}$$

where $h_0$ is the noise amplitude and can be related to the Allan deviation by [47]

$$\sigma_y^2(\tau) = \frac{h_0}{2\tau}, \tag{C6}$$

with $\tau$ the measurement time. Combining the above expressions one obtains the Allan deviation in terms of the locking power

$$\sigma_y(\tau) = \frac{1}{\sqrt{2\tau}}\frac{1}{4}\sqrt{\frac{h\nu}{P_c}}\delta\nu_{cav}. \tag{C7}$$

Considering a locking time of $\tau = 1$ s, $\nu = 500$ THz, $\delta\nu_{cav} = 1$ kHz and a fractional stability of $\frac{\sigma_y}{\nu} = 1 \times 10^{-17}$, the required locking power corresponds to $P_c = 4.1 \times 10^{-10}$ W. As will be demonstrated in appendix E, this yields a locking time of more than 2 h. This time may be indefinitely extended by utilizing two slow-light cavities with an interleaved locking and preparation scheme, as has been demonstrated for spectral-hole locking [24].

## Appendix D. Off-resonant excitation width

In the section 3 it was noted that when a pulse propagates through a spectral transparency window the surrounding ions off-resonantly absorb photons over a frequency range that scales with the transparency

window width $\Gamma$. To arrive at this statement, we begin with a transparency window centered at the origin and, for simplicity, only consider blue detuned frequencies. Further, we note that the off-resonant absorption cross-section fulfills the following proportionality

$$\sigma(\Delta) \propto \frac{1}{1+(2\Delta/\Gamma_{\rm h})^2}, \tag{D1}$$

where $\Delta$ is the optical detuning [48]. We consider the number of photons absorbed by the ions located within an interval of width $\Gamma/2$, half the width of the transparency window, and located immediately adjacent in frequency to the transparency window. Dividing this number by the total number of photons absorbed by all ions positively detuned from the transparency window, one obtains the fraction of absorbed photons

$$\frac{\int_{\Gamma/2}^{\Gamma}\frac{{\rm d}\Delta}{1+(2\Delta/\Gamma_{\rm h})^2}}{\int_{\Gamma/2}^{\infty}\frac{{\rm d}\Delta}{1+(2\Delta/\Gamma_{\rm h})^2}} = \frac{\left[\frac{\Gamma_{\rm h}}{2}\tan^{-1}\left(\frac{2\Delta}{\Gamma_{\rm h}}\right)\right]_{\Gamma/2}^{\Gamma}}{\left[\frac{\Gamma_{\rm h}}{2}\tan^{-1}\left(\frac{2\Delta}{\Gamma_{\rm h}}\right)\right]_{\Gamma/2}^{\infty}} \simeq 0.5, \tag{D2}$$

where the last equality assumes that $\Gamma/\Gamma_{\rm h} \gg 1$. An analogous calculation holds for the red detuned ions. Consequently, it follows that 50% of the off-resonant absorption at the center of the spectral transparency window comes from the atoms in the intervals $[-\Gamma, -\Gamma/2]$ and $[\Gamma/2, \Gamma]$.

## Appendix E. Locking time estimate

In order to estimate the maximum locking time the spectral transparency window deterioration rate due to off-resonant absorption is required. For an impedance matched cavity, all of the photons in the carrier can be assumed to be absorbed. For a locking power of $P_{\rm c} = 4.1 \times 10^{-10}$ W the photon flux is

$$N = \frac{P_{\rm c}}{h\nu} \approx 1.3 \times 10^{9}\ {\rm s}^{-1}. \tag{E1}$$

Considering only the ions that are located within a frequency width $\Gamma$ on either side of the transparency window, this corresponds to half of the total number of photons absorbed (shown in appendix D). Defining this as $N_{{\rm abs},\Gamma} = N/2 = 6.5 \times 10^{8}\ {\rm s}^{-1}$, the locking time can then be estimated as

$$T = \frac{N_{\rm ions}}{N_{{\rm abs},\Gamma}}, \tag{E2}$$

where $N_{\rm ions}$ is the total number of ions in the interaction volume that can be excited before the spectral transparency window shape deteriorates to a level that makes locking unfeasible. For an inhomogeneous linewidth of $\Gamma_{\rm inhom} = 22$ GHz, the dopant ion density has the form

$$\rho_{\rm ions} = \frac{\rho_{\rm host}\delta}{\Gamma_{\rm inhom}} \approx 4 \times 10^{15}\ ({\rm m}^{-3}\ {\rm Hz}^{-1}). \tag{E3}$$

Here, $\rho_{\rm host} = 9.15 \times 10^{27}\ {\rm m}^{-3}$ is the density of yttrium atoms located at site 1 for which the dopant can substitute in $Y_2SiO_5$ (assuming equal site 1 and site 2 occupation) [49], and $\delta = 1\%$ corresponds to the dopant concentration. As photons scatter off ions that are adjacent in frequency to the transparency window, there is a probability that the ions will be pumped to a different state which would broaden the cavity linewidth and therefore require an increase in the locking power in order to maintain the same Allan deviation. Somewhat arbitrarily setting the threshold where this starts to affect the locking at 10%, one obtains

$$N_{\rm ions} = 0.1\rho_{\rm ions}\Gamma V = 5 \times 10^{12}, \tag{E4}$$

where the interaction volume $V$ was taken as $0.25 \times 10^{-6}\ {\rm m}^3$. This leads to a total locking time of 128 min. Note that we have neglected the probability that ions that are excited decay back to the same state from which they were excited. For the branching ratios of the relevant transition in $Eu^3$:$Y_2SiO_5$ there is a significant probability this can occur; however, including this effect would only improve the locking time. Consequently, it is perfectly reasonable to ignore this effect in order to obtain a lower bound on the attainable locking time.

## Appendix F. Data analysis details

In this section we discuss details of the data analysis performed to produce key figures in the main text. In particular, figure 5 shows the frequency feedback signal recorded as the length of the locking cavity was

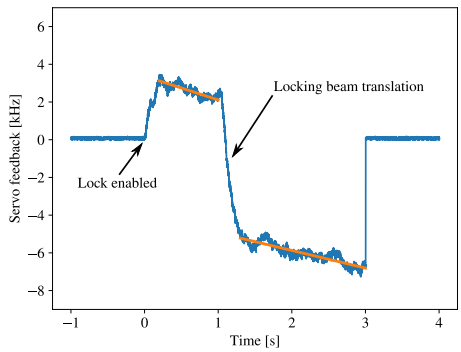


**Figure 5.** The servo feedback recorded while the locking beam was translated horizontally by 2 $\mu$m. The lock was enabled at $t = 0$ s; the large initial feedback signal is attributed to an offset of the initial locking point, as well as a small amount of unburned ions near the mirror coatings leading to a local perturbation of the dispersion. This latter effect was largely mitigated by diffusing and dithering the perpendicular burning beam, as described in the methods section. The locking beam translation occurs 2 $\mu$m at $t = 1$ s.

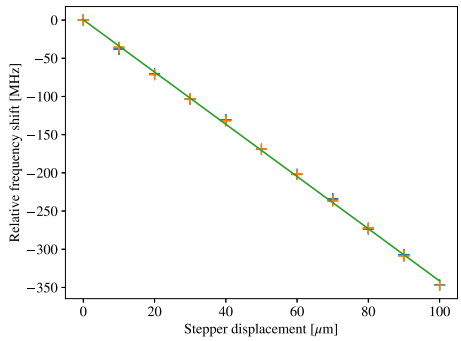


**Figure 6.** The frequency shift with respect to the locking beam displacement when detuned by $\simeq 5.3$ THz from the $Pr^{3+}$ ensemble. The frequency shifts were obtained from the resonance frequencies of the cavity observed in transmission for each stepper motor displacement.

altered by translating the beam along the wedged surface of the locking crystal. The trace corresponds to the PI servo output monitored via a high-impedance buffer circuit.

The plot shows a steep initial ramp, which is attributed to residual ions near the mirror coatings due to a standing wave pattern set up by the perpendicular burning beam. This effect was minimized by dithering the perpendicular burning beam, but some residual ions remained. For a practical implementation of this locking scheme, a material with a slower spin-lattice relaxation rate would resolve this issue. A linear function was fitted to the feedback both before and after the step; this allowed for any residual drift to be subtracted. The time required to complete a given step size was determined by inspection of representative servo-feedback data. The frequency change error bars in figure 2 were determined by evaluating the standard error of 10 independent measurements. However, there could be a systematic error in the step timing interval selection, which would be missed by this error analysis. The error bars for the cavity length change also assumed that errors were randomly distributed; if there was a systematic error in the stepper motor, this would not be accounted for in our uncertainty analysis. We note that effects of backlash for the motor driven mirror were mitigated using a servo readout.

The above outlined procedure was employed for analyzing the beam translation experiments for the group velocities of $v_g = c/7500$ and $v_g = c/2790$. In the scenario where there was no slow-light effect, the frequency shift data was obtained by translating the beam over a range of steps and performing a linear fit

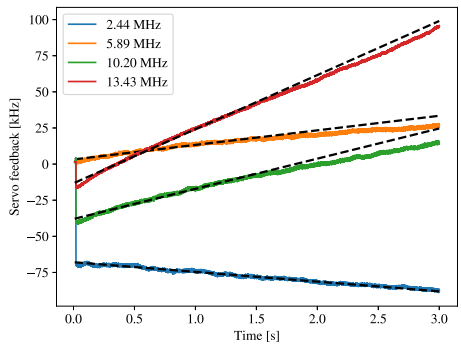


**Figure 7.** Representative locking feedback data when the laser was locked to different cavity modes across the spectral transparency window. The different slopes originate from the varying rates of off-resonant excitation combined with the fast hyperfine cross-relaxation between the $|\pm 1/2g\rangle$ and $|\pm 3/2g\rangle$ states. Comparable data was obtained for a range of optical locking power intensities.

to the cavity mode peaks (determined from a Lorentzian fit). This data is summarized in figure 6. The uncertainties in the frequency shift were obtained from the covariance matrix of the first order polynomial fit shown in figure 6.

Figure 7 shows the drift data from which the 6 $\mu$W data points of figure 4 were obtained. These are representative of the drift data obtained for other locking beam powers. The indicated frequencies correspond to the cavity mode center frequencies to which the laser was locked. A linear fit was performed using the frequency interval between 0.1–1.5 s; this restricted fitting interval was selected since, as discussed above, for larger locking beam powers off-resonant excitation lead to a non-linear drift at longer locking times. The error bars shown in figure 4 were determined from the square roots of the corresponding covariance matrices.

## ORCID iDs

Sebastian P Horvath https://orcid.org/0000-0002-8804-6366
Adam Kinos https://orcid.org/0000-0002-1472-0100

## References

[1] Ludlow A D, Boyd M M, Ye J, Peik E and Schmidt P O 2015 *Rev. Mod. Phys.* **87** 637
[2] LIGO Scientific Collaboration and Virgo Collaboration 2016 *Phys. Rev. Lett.* **116** 061102
[3] Chou C W, Hume D B, Rosenband T and Wineland D J 2010 *Science* **329** 1630
[4] Eisele C, Nevsky A Y and Schiller S 2009 *Phys. Rev. Lett.* **103** 090401
[5] Ludlow A D, Huang X, Notcutt M, Zanon-Willette T, Foreman S M, Boyd M M, Blatt S and Ye J 2007 *Opt. Lett.* **32** 641
[6] Webster S A, Oxborrow M, Pugla S, Millo J and Gill P 2008 *Phys. Rev.* A **77** 033847
[7] Chen Q-F, Nevsky A, Cardace M, Schiller S, Legero T, Häfner S, Uhde A and Sterr U 2014 *Rev. Sci. Instrum.* **85** 113107
[8] Häfner S, Falke S, Grebing C, Vogt S, Legero T, Merimaa M, Lisdat C and Sterr U 2015 *Opt. Lett.* **40** 2112
[9] Matei D G *et al* 2017 *Phys. Rev. Lett.* **118** 263202
[10] Numata K, Kemery A and Camp J 2004 *Phys. Rev. Lett.* **93** 250602
[11] Jiang Y Y, Ludlow A D, Lemke N D, Fox R W, Sherman J A, Ma L-S and Oates C W 2011 *Nat. Photon.* **5** 158
[12] Seel S, Storz R, Ruoso G, Mlynek J and Schiller S 1997 *Phys. Rev. Lett.* **78** 4741
[13] Kessler T, Hagemann C, Grebing C, Legero T, Sterr U, Riehle F, Martin M J, Chen L and Ye J 2012 *Nat. Photon.* **6** 687
[14] Amairi S, Legero T, Kessler T, Sterr U, Wübbena J B, Mandel O and Schmidt P O 2013 *Appl. Phys.* B **113** 233
[15] Cole G D, Zhang W, Martin M J, Ye J and Aspelmeyer M 2013 *Nat. Photon.* **7** 644
[16] Brückner F, Friedrich D, Clausnitzer T, Britzger M, Burmeister O, Danzmann K, Kley E-B, Tünnermann A and Schnabel R 2010 *Phys. Rev. Lett.* **104** 163903
[17] Bishof M, Zhang X, Martin M J and Ye J 2013 *Phys. Rev. Lett.* **111** 093604
[18] Christensen B T R, Henriksen M R, Schäffer S A, Westergaard P G, Tieri D, Ye J, Holland M J and Thomsen J W 2015 *Phys. Rev.* A **92** 053820
[19] Norcia M A and Thompson J K 2016 *Phys. Rev.* X **6** 011025
[20] Sellin P B, Strickland N M, Carlsten J L and Cone R L 1999 *Opt. Lett.* **24** 1038
[21] Julsgaard B, Walther A, Kröll S and Rippe L 2007 *Opt. Express* **15** 11444
[22] Thorpe M J, Rippe L, Fortier T M, Kirchner M S and Rosenband T 2011 *Nat. Photon.* **5** 688

[23] Chen Q-F, Troshyn A, Ernsting I, Kayser S, Vasilyev S, Nevsky A and Schiller S 2011 *Phys. Rev. Lett.* **107** 223202
[24] Leibrandt D R, Thorpe M J, Chou C-W, Fortier T M, Diddams S A and Rosenband T 2013 *Phys. Rev. Lett.* **111** 237402
[25] Cook S, Rosenband T and Leibrandt D R 2015 *Phys. Rev. Lett.* **114** 253902
[26] Gobron O, Jung K, Galland N, Predehl K, Le Targat R, Ferrier A, Goldner P, Seidelin S and Le Coq Y 2017 *Opt. Express* **25** 15539
[27] Galland N *et al* 2020 *Opt. Lett.* **45** 1930
[28] Pati G S, Salit M, Salit K and Shahriar M S 2008 *Opt. Commun.* **281** 4931
[29] Yablon J, Zhou Z, Condon N, Hileman D, Tseng S and Shahriar S 2017 *Opt. Express* **25** 30327
[30] Sabooni M, Li Q, Rippe L, Mohan R K and Kröll S 2013 *Phys. Rev. Lett.* **111** 183602
[31] Black E D 2000 *Am. J. Phys.* **69** 79
[32] Siegman A E 1986 *Lasers* (Mill Valley, CA: University Science Books)
[33] Nilsson M, Rippe L, Kröll S, Klieber R and Suter D 2004 *Phys. Rev.* B **70** 214116
[34] Riley W and Howe D 2008 Handbook of frequency stability analysis *Special Publication (NIST SP)* Gaithersburg, MDNational Institute of Standards and Technology https://tsapps.nist.gov/publication/get_pdf.cfm?pub_id=50505
[35] Ma L-S, Jungner P, Ye J and Hall J L 1994 *Opt. Lett.* **19** 1777
[36] Oswald R, Hansen M G, Wiens E, Nevsky A Y and Schiller S 2018 *Phys. Rev.* A **98** 062516
[37] Thorpe M J, Leibrandt D R and Rosenband T 2013 *New J. Phys.* **15** 033006
[38] Nilsson M 2005 Coherent interactions in rare-earth-ion-doped crystals for applications in quantum information science *Thesis/Doccomp* Lund University https://lup.lub.lu.se/record/544192
[39] Equall R W, Sun Y, Cone R L and Macfarlane R M 1994 *Phys. Rev. Lett.* **72** 2179
[40] Equall R W, Cone R L and Macfarlane R M 1995 *Phys. Rev.* B **52** 3963
[41] Alnis J, Matveev A, Kolachevsky N, Udem T and Hänsch T W 2008 *Phys. Rev.* A **77** 053809
[42] Sun Y C 2006 *Spectroscopic Properties of Rare Earths in Optical Materials* ed G Liu and B Jacquier (Berlin: Springer) pp 379–429
[43] Chanelière T 2021 private communication
[44] Lauro R, Chanelière T and Le Gouët J L 2009 *Phys. Rev.* A **79** 063844
[45] Saleh B E and Teich M C 2007 *Fundamentals of Photonics* (New York: Wiley)
[46] King F W 2009 *Hilbert Transforms* vol 1 (Cambridge: Cambridge University Press)
[47] Stein S R 1985 *Precision Frequency Control* vol 2 (New York: Academic) p 191
[48] Allen L and Eberly J H 1987 *Optical Resonance and Two-Level Atoms* (New York: Wiley)
[49] Könz F, Sun Y, Thiel C W, Cone R L, Equall R W, Hutcheson R L and Macfarlane R M 2003 *Phys. Rev.* B **68** 085109

# Paper II

D. Gustavsson, M. Lindén, K. Shortiss, S. Kröll, A. Walther, A. Kinos and L. Rippe
"Using slow light to enable laser frequency stabilization to a short, high-Q cavity",
*Manuscript submitted for publication* (2024)

# Using slow light to enable laser frequency stabilization to a short, high-Q cavity

DAVID GUSTAVSSON,[1,*] MARCUS LINDÉN,[1,2] KEVIN SHORTISS,[1] STEFAN KRÖLL,[1] ANDREAS WALTHER,[1] ADAM KINOS,[1] AND LARS RIPPE[1]

[1] *Lund University, Faculty of Engineering, Department of Physics, Box 188, 221 00 Lund, Sweden*
[2] *Measurement Science and Technology, RISE Research Institutes of Sweden*
[*] *david.e.gustavsson@gmail.com*

**Abstract: State-of-the-art laser frequency stabilization is limited by miniscule length changes caused by thermal noise. In this work, a cavity-length-insensitive frequency stabilization scheme is implemented using strong dispersion in a** $21\,\mathrm{mm}$ **long cavity with a europium-ion-doped spacer of yttrium orthosilicate. A number of limiting factors for slow light laser stabilization are evaluated, including the inhomogeneous and homogeneous linewidth of the ions, the deterioration of spectral windows, and the linewidth of the cavity modes. Using strong dispersion, the cavity modes were narrowed by a factor** $1.6 \cdot 10^5$**, leading to a cavity linewidth of** $3.0\,\mathrm{kHz}$ **and a** $Q$ **factor of** $1.7 \cdot 10^{11}$**. Frequency stabilization was demonstrated using a cavity mode in a spectral transparency region near the center of the inhomogeneous profile, showing an overlapping Allan deviation below** $6 \cdot 10^{-14}$ **and a linear drift rate of** $3.66\,\mathrm{Hz\,s^{-1}}$**. Considering improvements that could be implemented, this makes the europium-based slow light laser frequency reference a promising candidate for ultra-precise tabletop frequency stabilization.**

## 1. Introduction

Modern high precision measurement relies on accurate and stable clocks and frequency references. Developments in these devices have allowed advances in experiments such as gravity wave detection [1–3] and tests of relativity [4–7]. The best clocks to date are optical clocks [8–10], where the frequency generating element is a laser, locked long-term to atomic resonance frequencies. For short-term frequency stability, the laser is locked to a reference cavity, such that the relative length stability of the cavity is translated into a relative frequency stability for the laser.

State-of-the-art reference cavities are typically on the order of tens of centimeters long and mechanically and thermally stabilized to the level where the limiting factor is Brownian motion in the atoms forming the mirrors [11, 12]. A number of avenues are being pursued to mitigate this Brownian length uncertainty, including cryogenic cooling, crystalline mirror coatings, increased locking beam widths, and longer cavities.

The uncertainty in position of atoms in Brownian motion scales with the square root of the temperature [13], meaning that reducing from room temperature (300 K) to a liquid helium cryostat (on the order of 3 K) gives one order of magnitude reduction [14, 15]. Further cooling is possible, but comes with new technical challenges.

Conventional stabilization cavities use amorphous multi-layer thin-film mirrors, deposited by ion beam sputtering. While these have good optical properties, they can be improved on with respect to Brownian noise. Specifically, epitaxially grown monocrystalline layers of semiconductor materials have shown between one and two orders of magnitude reduction in Brownian length uncertainty [16, 17].

Since the Brownian noise is independent across the mirror, it can be averaged down by increasing the locking beam area, and scales with the reciprocal of the beam radius at the mirror [11]. Efforts into increasing the beam area involve operating cavities near instability,

in near-planar or near-concentric configurations [18]. This leads to a trade-off between beam area and sensitivity to mechanical noise and misalignment, which makes an order of magnitude increase from the 1.5 mm diameter beams studied in Ref. [18] improbable.

The relative frequency uncertainty depends on the relative length uncertainty, and so scales as the reciprocal of the cavity length. Ultra-stable cavities up to 50 cm long have been demonstrated [12], but an order of magnitude improvement in this respect, appears unlikely in the foreseeable future as it requires mechanically and thermally stabilizing a 5 m long cavity.

All of these techniques are approaching their current technical limits, and can each realistically provide about one or two orders of magnitude reduction from the current state-of-the-art. In Ref. [19], we presented another avenue to decrease the Brownian length uncertainty using the slow light effect. By spectral tailoring, narrow frequency regions where the material is transparent (transmission windows) can be generated in the inhomogeneously broadened absorption profile of a cryogenically cooled rare-earth crystal, resulting in strong dispersion. When the crystal is included in a cavity, this dispersion has the effect of increasing the cavity round-trip time, effectively making the cavity orders of magnitude longer without the associated increase in difficulty of mechanical stabilization.

This method is notably compatible with most of the alternative approaches: It is by necessity performed at cryogenic temperatures, can utilize flat mirror cavities which allows large locking beam radii, and does not in principle preclude crystalline mirror coating. For this reason slow light frequency stabilization offers several additional orders of magnitude reduction in length sensitivity. It does, however, introduce new sources of frequency uncertainty from the degradation over time of the spectral structures in the spacer material.

In this work, we describe and evaluate a flat-mirror slow light cavity made from europium doped yttrium orthosilicate where the choice of material, the design of the cavity and the methods used are all optimized to ultimately enable ultra-stabilization while minimizing the previously identified sources of degradation.

## 2. Background and theory

As the group velocity $v_g$ decreases due to increasing dispersion, variation in mode frequency $\nu$ due to the variation in cavity length $L$ scales as [19]

$$\frac{\mathrm{d}\nu}{\nu} = -\frac{\mathrm{d}L}{L}\frac{v_g}{c_0} = -\frac{\mathrm{d}L}{L}\frac{n_0}{n_0 + \nu\frac{\mathrm{d}n}{\mathrm{d}\nu}}\,, \tag{1}$$

with refractive index $n$ varying approximately linearly with frequency around the host refractive index $n_0$. $c_0$ is the speed of light in vacuum. Evidently, strong dispersion $\mathrm{d}n/\mathrm{d}\nu$, such as that generated in a narrow spectral window, greatly reduces the cavity's sensitivity to length variations.

To use this effect, mirror coatings are deposited on two opposite faces of a rare-earth-ion-doped crystal in which a spectral window is generated using optical pumping. The resulting dispersion narrows the cavity modes by orders of magnitude, and the reflection of a frequency modulated locking beam is used to generate a Pound-Drever-Hall (PDH) error signal. A feedback loop is established using this signal to lock the laser frequency to one of the cavity's resonance frequencies.

Because of the aforementioned reduction in sensitivity to length changes, the primary cause of drift in the resonance frequency of such a reference cavity will be spectral degradation of the transmission window through off-resonant excitation by the locking beam. The ions are homogeneously broadened, and the ions near the edges of the window, whose homogeneous absorption profile reaches into the window, will be off-resonantly excited. As these ions absorb the locking beam, they get optically pumped away and deform the window. This part of the drift therefore depends on the locking beam intensity and the distance in frequency of the mode from the edges of the window, relative to the homogeneous linewidth of the ions.

In this work, we use a crystal of europium-doped yttrium orthosilicate (Eu:YSO, $Eu^{3+}$:$Y_2SiO_5$). Eu:YSO displays a good combination of parameters for slow light stabilization, with spectral structures remaining in excess of 49 days at 1.15 K [20], and homogeneous linewidths as narrow as hundreds of Hz [21]. The long hyperfine lifetimes mean the spontaneous window drift, which has previously been observed in $Pr^{3+}$:$Y_2SiO_5$ [19], is negligible, and the narrow homogeneous linewidth means the window can be made narrow while still displaying a low off-resonant excitation.

Furthermore, we reduce off-resonant excitation by using a flat-mirror cavity, which allows us to use a large locking beam area and therefore low intensity. A flat mirror cavity has degenerate transversal modes, and the resonance frequency would typically be very sensitive to fluctuations in locking beam angle, but just as in the case of length changes this sensitivity is reduced by the strong dispersion, as derived in appendix C, and flat mirrors can therefore be used in the slow light stabilization scheme. A large beam radius reduces the locking intensity and thereby the off-resonant excitation, and carries the additional benefit of averaging down the Brownian length uncertainty.

In order to further minimize drift caused by off-resonant excitation, we present a method to shift the cavity modes relative to the center frequency of the spectral transmission window by iteratively burning windows at different frequencies relative to the inhomogeneous profile. This is done with the goal of placing a mode right at the window center frequency. Locking to such a centered mode causes symmetric degradation at both edges of the window, eliminating first-order drift. As an additional benefit, the total rate of degradation is minimized by minimizing the total off-resonant absorption. As derived in appendix B, moving the center frequency of the window $\nu_{\mathrm{win}}$ will shift the mode frequency $\nu_{\mathrm{mode}}$ relative to the window by a factor which is reduced about as much as the group velocity,

$$\frac{\mathrm{d}\nu_{\mathrm{mode}}}{\mathrm{d}\nu_{\mathrm{win}}} = -\frac{n_0}{n_g} + \frac{\pi\Gamma_{\mathrm{win}}}{2\Gamma_{\mathrm{ih}}} \tag{2}$$

with group refractive index $n_g$, host refractive index $n_0$, window width $\Gamma_{\mathrm{win}}$ and inhomogeneous linewidth $\Gamma_{\mathrm{ih}}$.

To get a strong locking signal, the contrast between resonance and non-resonance needs to be maximized, which requires impedance matching. This means the transmission of the front mirror should equal the effective losses of the cavity, including transmission of the back mirror and round-trip losses through the cavity. If the front and back mirror reflectivity are $R_1$ and $R_2$ respectively, and the material has an absorption coefficient $\alpha L$ and a round-trip length $L_{\mathrm{RT}}$ such that the round-trip intracavity transmission is $\exp(-\alpha L_{\mathrm{RT}})R_1R_2$, the on-resonance reflectivity of the cavity in total is

$$R_{\mathrm{cav}} = R_1\left|1 - \frac{1-R_1}{\sqrt{\frac{R_1}{R_2}}\exp(\alpha L_{\mathrm{RT}}) - R_1}\right|^2. \tag{3}$$

Impedance matching means $\alpha L_{\mathrm{RT}} = \ln(R_2/R_1) \Rightarrow R_{\mathrm{cav}} = 0$. In a spectral transmission window, there will always be some off-resonant absorption from the ions near the edges of the window, and the narrower the window, the larger the absorption is in its center. In this way, the window width, $\Gamma_{\mathrm{win}}$, can be tuned to adjust the absorption in the center of the window, $\alpha_{\mathrm{c}}$, and seek impedance matching. The center absorption $\alpha_{\mathrm{c}}$ for a square window of width $\Gamma_{\mathrm{win}}$ in a material with homogeneous linewidth $\Gamma_h$ in a region where the absorption outside the window is $\alpha$ was shown in Ref. [19] to be

$$\alpha_{\mathrm{c}} \approx \frac{2}{\pi}\frac{\Gamma_h}{\Gamma_{\mathrm{win}}}\alpha. \tag{4}$$

As long as the total cavity losses are below impedance matching for some large $\Gamma_{\mathrm{win}}$, such matching can be achieved by reducing $\Gamma_{\mathrm{win}}$ until the desired $\alpha_{\mathrm{c}}$ is achieved.

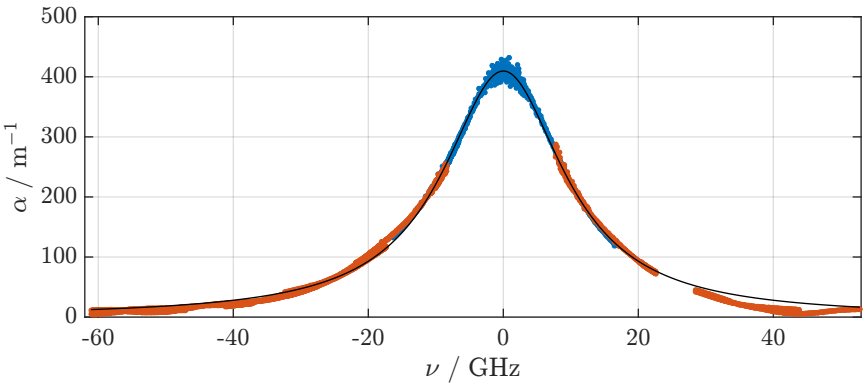


Fig. 1. Inhomogeneous profile of the $^7F_0 \rightarrow {}^5D_0$ transition in 1 at% $Eu^{3+}$:$Y_2SiO_5$, with $\nu_0 = 516.85\,\mathrm{THz}$ subtracted. Red and blue are measured with two different gain settings of the detector. The black line is a Lorentzian profile fit with full-width half-maximum linewidth $\Gamma_i = 22\,\mathrm{GHz}$ and peak height $\alpha_0 = 410\,\mathrm{m}^{-1}$.

## 3. Experiments

### 3.1. Characterization

Good slow light frequency stabilization requires large dispersion, which means that a narrow spectral transmission window with sharp edges must be created within a region of large absorption. Furthermore, the transmission window must be stable in time to enable frequency locking for an extended period. The $^7F_0$ transition in europium doped to 1 at% into YSO has a narrow homogeneous linewidth, and was measured in this crystal, using two-pulse photon echos, to be 440 Hz corresponding to a coherence time, $T_2$, of 725 µs. This narrow linewidth makes it possible to create windows with sharp edges. Furthermore, the material has previously been shown to have extremely long hyperfine lifetimes, and no evident decay from hyperfine cross-relaxation was observed over our experiment durations. The free spectral range of our cavity (length $L = 21\,\mathrm{mm}$ and host refractive index $n_0 = 1.8$) is $\nu_{\mathrm{FSR}} = c_0/(2n_0L) = 4\,\mathrm{GHz}$, and the inhomogeneous linewidth needs to be wide relative to this to ensure that there is a choice of window frequency within a region of large absorption. We therefore used a high europium doping of 1 %, which gave a full-width half-maximum inhomogeneous linewidth of 22 GHz, in line with the value reported in Ref. [22]. The inhomogeneous profile was measured in transmission using two detectors with different gain settings to capture the full dynamic range, and a Lorentzian profile was fitted as shown in fig. 1. To compensate a calibration mismatch, evident from the region where the two data sets overlap, the low-gain data has been scaled down by 8 %.

Through spectral tailoring, narrow transmission windows were burned into the absorption profile using optical pumping. Repeated sechscan pulses (a linearly chirped square pulse bookended by two halves of a secant hyperbolicus pulse, introduced as HSH in Ref. [23]) were used, in order to achieve sharp transmission window edges. To avoid standing wave patterns and perform spectral tailoring evenly throughout the length of the crystal, a diffuse and wide burning beam was injected orthogonally to the probing axis. A fiber-coupled sideburner was designed for this purpose, illustrated in fig. 2 (top left), and described further in appendix A. By optimizing the optical pumping sequence, we were able to create windows as narrow as 30 kHz, see fig. 3. The absorption profile as a function of frequency was obtained by sending in long square pulses at different frequencies, which only probed a narrow frequency range. To cover the large dynamic

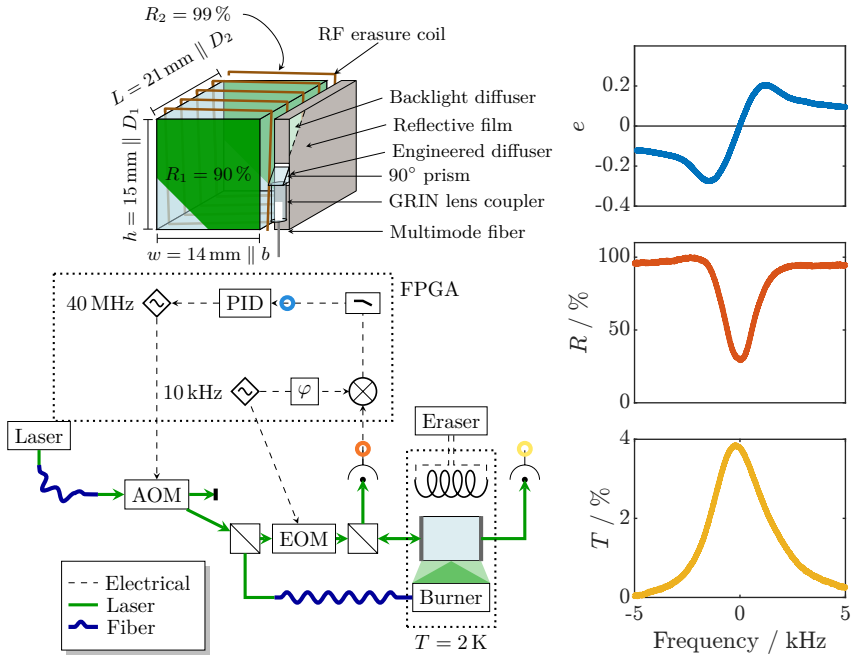


Fig. 2. Top left: The crystal used in experiments, with dimensions and crystallographic axes marked. Rough geometry of the RF erasure coil, as well as the components of the side burner module. Bottom left: Schematic of the setup for stabilization experiments. Signal collection points are marked with colored circles, matching the respective trace on the right. The relative geometry of the components inside the cryostat is more accurate in the top left graphic. Right: PDH error signal ($e$), cavity reflection ($R_{\mathrm{cav}}$) and transmission ($T_{\mathrm{cav}}$), averaged over several frequency-chirped readouts. The transmission linewidth is $\Delta\nu = 3\,\mathrm{kHz}$.

range of the signal, two detectors with different gain settings were used. The dispersion was measured by sending a Gaussian pulse through the center of the window (fig. 4), resulting in a pulse delay of 39 µs corresponding to a group velocity of $540\,\mathrm{m\,s^{-1}}$ and a group refractive index of $5.6 \cdot 10^5$. These measurements were performed through an uncoated part of the crystal.

A cavity was constructed by depositing reflective coatings on the front and back face of the crystal, with 90 % and 99 % reflectivity respectively. For locking experiments, the setup illustrated in fig. 2 was used. PDH locking was established using a digital laser servo described in Ref. [24]. The shape of the measured reflection and transmission signals, as well as the PDH locking signal, when probed with a linearly chirped laser is shown in fig. 2 (right). The full-width half-maximum mode width was measured in transmission to $\Delta\nu = 3\,\mathrm{kHz}$, $1.61 \cdot 10^5$ times narrower than the non-dispersive cavity linewidth. The experimental quality factor for this cavity is $Q = \nu_0/\Delta\nu = 1.7 \cdot 10^{11}$, which is extremely high for a cavity like this one. For comparison, the $Q$ factor without dispersion is $1.06 \cdot 10^6$. As derived in Ref. [19], the minimum linewidth for an impedance matched slow light cavity is $\Delta\nu_{\mathrm{min}} = 2\Gamma_h = 880\,\mathrm{Hz}$, which leads to a maximum theoretical $Q$ value of $5.9 \cdot 10^{11}$ for this particular cavity.

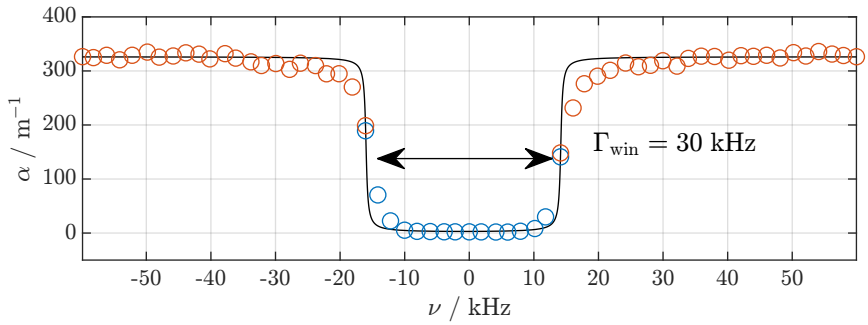


Fig. 3. A narrow spectral transmission window of width $\Gamma_{\text{win}}$ = 30 kHz. Absorption measured by transmission of long, spectrally narrow pulses using two detectors with different photodetector gain settings (blue: low gain, red: high gain). In black is the theoretical absorption profile of a square-population window, a sum of arctangent curves, derived in Ref. [19]. The discrepancy between the data and the theoretical model is explained by a slight over-burning of ions in the edges of the window.

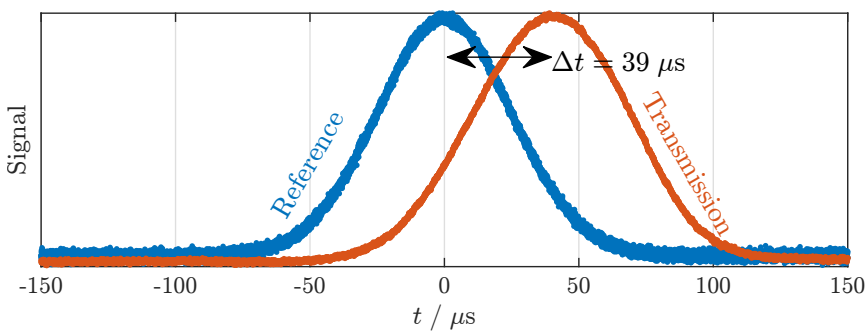


Fig. 4. A Gaussian pulse propagated through the crystal in the middle of a 30 kHz wide spectral window near the center of the inhomogeneous profile (blue: reference, red: transmitted signal), showing the time delay for light propagating in the transmission window, $\Delta t$ = 39 µs. The signals have been separately normalized, the vertical scale is arbitrary.

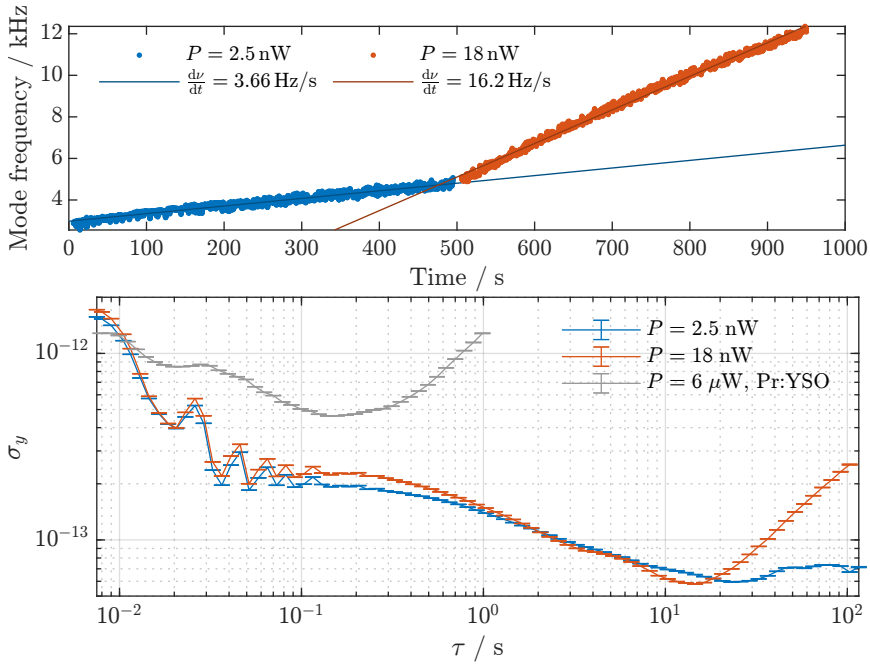


Fig. 5. Top: Long term drift of two 500 s locks in a 40 kHz wide window, where the locking power is increased after the first 500 s. The mode frequency is retrieved from the servo feedback signal. Bottom: Overlapping Allan deviation with linear drift subtracted, for two locks with different power in the europium doped crystal, compared to a praseodymium doped crystal (calculated from data reported in Ref. [19]). The measured noise floor is $\sigma_y = 6 \cdot 10^{-14}$.

### 3.2. *Stabilization*

Pound-Drever-Hall stabilization was established to a mode inside a 40 kHz wide window over 500 s intervals. In order to measure the power induced drift from off-resonant excitation, a low power (approximately 2.5 nW) lock was followed by one at 7 times higher power. One such lock is shown in fig. 5 (Top), where the drift rate at low power was measured to be $3.66\,\mathrm{Hz\,s^{-1}}$ when locking to a mode 2 kHz above the center frequency. As discussed in Ref. [19], this drift is likely from asymmetric off-resonant excitation of ions near the window edges, which causes the mode to move relative to the center of the window. Figure 5 (Bottom) shows the overlapping Allan deviation of these locks, with linear drift subtracted, as suggested in Ref. [25], compared to the lock to a praseodymium doped YSO crystal reported in Ref. [19]. The laser noise floor is $\sigma_y = 6 \cdot 10^{-14}$, at averaging times above 10 s, below which it is likely limited by fiber noise. This is an order of magnitude improvement over the praseodymium value, using 300 times less locking power.

In order to lock to a mode near the center frequency of the transmission window, windows were created at several frequencies across the inhomogeneous absorption profile and the corresponding mode frequency measured (fig. 6). Between each measurement, the structures were reset using RF erasure, evaluated separately in Ref. [26]. A least squares fit was performed of eq. (17) (appendix B), with the mode offset $r$ and the peak absorption $\alpha_0$ as fitting parameters, to the

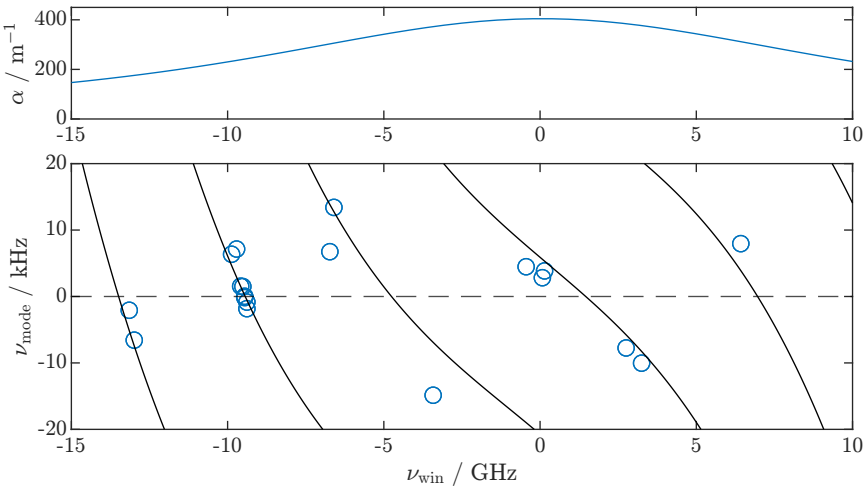


Fig. 6. Bottom: Mode frequency relative to window center frequency $\nu_{\mathrm{mode}}$ vs window frequency relative to absorption peak frequency $\nu_{\mathrm{win}}$ in 40 kHz wide spectral windows. Best fit of the theoretical model derived in appendix B is marked with lines. The horizontal dashed line corresponds to the center of the window, where the drift is theoretically zero to first order. Top: Lorentzian fit of the inhomogeneous profile in fig. 1, as a visual guide.

measured mode frequencies. The best fit lines are marked in black in fig. 6. The fit predicted a peak absorption of 353 $\mathrm{m}^{-1}$, somewhat lower than the 410 $\mathrm{m}^{-1}$ measured in transmission (fig. 1). This discrepancy could potentially be explained by imperfect spectral tailoring. The overall behavior is approximately as predicted, so iteratively moving the window in steps of $\Delta\nu_{\mathrm{win}}$ allows one to get a mode within $\left(n_0/n_g\right)\Delta\nu_{\mathrm{win}}$ of the center of the window. It is not unrealistic, in future work, to move the window frequency in steps of $\Delta\nu_{\mathrm{win}} < 1$ kHz, giving $\Delta\nu_{\mathrm{mode}} < 10$ mHz. As we have previously shown that the power-induced drift rate scales roughly linearly with mode distance from the center of the window [19], this improvement should reduce the power-induced drift rate – the dominant drift in this work – by over five orders of magnitude, compared to fig. 5.

To verify impedance matching in the cavity, a 40 kHz wide window was burned near the center of the inhomogeneous profile, and then widened in steps without intermediate erasure, measuring the reflection and transmission of the cavity mode. Equation (4) relates the window width to an expected centre-of-window absorption $\alpha_{\mathrm{c}}$, which decreases with increasing window width. Figure 7 shows the measured on-resonance cavity reflectivity against $\alpha_{\mathrm{c}}$. Equation (3) was adapted into a fitting model with fitting parameters $R_{\mathrm{nc}}$ and $\alpha_{\mathrm{rem}}$,

$$R_{\mathrm{cav}} = R_{\mathrm{nc}} + (1 - R_{\mathrm{nc}})R_1 \left| 1 - \frac{1 - R_1}{\sqrt{\frac{R_1}{R_2}\exp\left(\left(\alpha_{\mathrm{c}} + \alpha_{\mathrm{rem}}\right) L_{\mathrm{RT}}\right)} - R_1} \right|^2 \tag{5}$$

where $R_{\mathrm{nc}}$ represents a non-coupling portion of the intensity that is immediately reflected due to transversal mode mismatch, and $\alpha_{\mathrm{rem}}$ represents remaining intracavity losses after compensating for off-resonant absorption $\alpha_{\mathrm{c}}$. This model was fit to the data using least-squares fitting, giving $R_{\mathrm{nc}} = 37\,\%$ and $\alpha_{\mathrm{rem}} L_{\mathrm{RT}} = 0.0038$. If $\alpha_{\mathrm{rem}} L_{\mathrm{RT}}$ is entirely due to residual, unburned population, this population is $\alpha_{\mathrm{rem}}/\alpha_0 = 0.03$. The fact that the cavity reflectivity increases with window

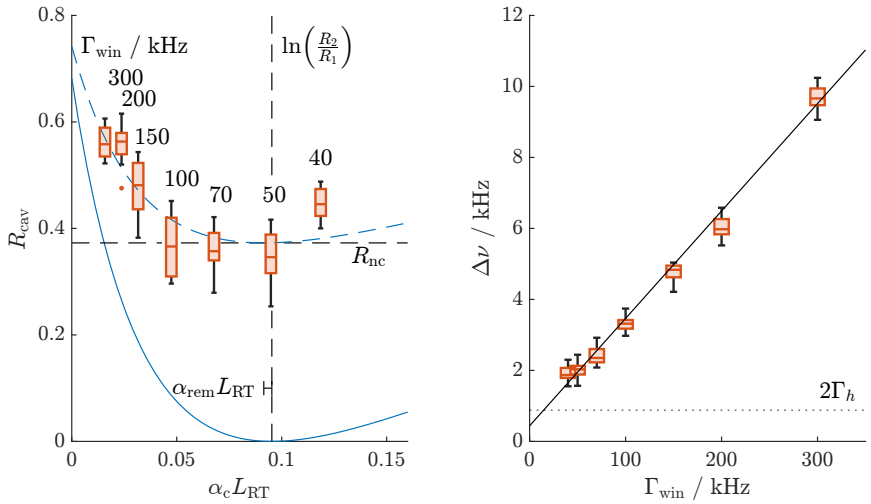


Fig. 7. Left: Reflectivity at resonance for sequentially widening windows, labeled with the respective window width. The horizontal position of each box is the theoretically predicted off-resonant absorption for a perfectly burned window of that width. Any residual absorption from remaining population or scattering losses will correspond to a horizontal shift. In dashed blue is a least-squares fit of the data with two fit parameters: a non-coupling portion $R_{\mathrm{nc}} = 37\,\%$ shifting the fit upwards and a remaining round-trip loss of $\alpha_{\mathrm{rem}}L_{\mathrm{RT}} = 0.0038$ shifting it vertically. Right: Cavity mode linewidth vs window width for the same modes, and a straight-line fit with a slope of 0.03. The dotted line represents the theoretical minimum linewidth $2\Gamma_h$, derived in Ref. [19].

width for the widest windows confirms that intra-cavity losses are low enough for impedance matching to occur in windows around 50 kHz wide. The mode width, shown in fig. 7 (Right), increases roughly linearly with window width, as derived in Ref. [19]:

$$\Delta\nu \approx \Gamma_h + \frac{\pi\,(2 - R_1 - R_2)}{4\alpha_0 L}\Gamma_{\mathrm{win}}\,. \tag{6}$$

The measured slope is 0.03, indicating that the finesse is 3 times lower than predicted in theory. The linear relationship between window width and mode width is nevertheless satisfactory.

## 4. Conclusion

We have designed and tested a highly doped Eu:YSO cavity and demonstrated that it is a promising candidate for ultra-stable slow light frequency stabilization. The homogeneous linewidth is narrow enough that sharp spectral windows down to 30 kHz wide could be burned without excessive off-resonant absorption, and the resulting slow light effect on the order of $5 \cdot 10^5$ enabled extremely narrow cavity modes, with a $Q$ value exceeding $10^{11}$. We showed that the spectral structures were stable down to the Hz s$^{-1}$ level while locking to a mode 2 kHz from the center of the window. Frequency stabilization was established for minutes at a time, with a measured noise floor of $\sigma_y = 6 \cdot 10^{-14}$. Determining the true achievable frequency stability of this reference will require more careful control of experimental conditions.

We have presented a technique by which the mode frequency can be tuned to the – to first order – drift-free position in the middle of the window, where power induced drift is no longer

limiting. This is made possible by the wide inhomogeneous linewidth of the material. We have also demonstrated that, by choosing the window width appropriately, the losses in the cavity can be satisfactorily controlled to achieve impedance matching.

The slow light effect in Eu:YSO potentially represents over five orders of magnitude reduction in sensitivity to length fluctuations, and does not conflict with other measures such as cryogenic cooling, crystalline mirrors, and increased locking beam radii. Combining these measures has the potential to greatly reduce Brownian noise, the current limiting factor to optical frequency stability.

## 5. Acknowledgements

The authors would like to thank Marco Pomponio at NIST, who developed the digital servo and signal generator used, and provided much useful information and timely software updates.

This research was supported by the Swedish Research Council (Grants No. 2016 - 05121, No. 2019 - 04949, and No. 2021 - 03755), the Knut and Alice Wallenberg Foundation (Grant No. 2016.0081), the Wallenberg Center for Quantum Technology funded by the Knut and Alice Wallenberg Foundation (Grant No. 2017.0449), the European Union EMPIR program (NEXTLASERS), the European Union FETFLAG program (SQUARE), and the Fund of the Walter Gyllenberg Foundation.

## References

1. B. P. Abbott, R. Abbott, R. Adhikari, *et al.*, "LIGO: the laser interferometer gravitational-wave observatory," Reports on Prog. Phys. **72**, 076901 (2009).
2. LIGO Scientific Collaboration, Virgo Collaboration, B. P. Abbott, *et al.*, "Observation of gravitational waves from a binary black hole merger," Phys. Rev. Lett. **116**, 061102 (2016).
3. Y. Li, Z. Luo, H. Liu, *et al.*, "Laser interferometer for space gravitational waves detection and earth gravity mapping," Microgravity Sci. Technol. **30**, 817–829 (2018).
4. C. Eisele, A. Y. Nevsky, and S. Schiller, "Laboratory test of the isotropy of light propagation at the $10^{-17}$ level," Phys. Rev. Lett. **103**, 090401 (2009).
5. C. W. Chou, D. B. Hume, T. Rosenband, and D. J. Wineland, "Optical clocks and relativity," Science **329**, 1630–1633 (2010).
6. P. Delva, J. Lodewyck, S. Bilicki, *et al.*, "Test of special relativity using a fiber network of optical clocks," Phys. Rev. Lett. **118**, 221102 (2017).
7. X.-Y. Lu, J.-S. Huang, C.-B. Liu, *et al.*, "Modeling clock comparison experiments to test special relativity," UNIVERSE **9**, 189 (2023).
8. Y. Y. Jiang, A. D. Ludlow, N. D. Lemke, *et al.*, "Making optical atomic clocks more stable with $10^{-16}$-level laser stabilization," Nat. Photonics **5**, 158–161 (2011).
9. T. L. Nicholson, S. L. Campbell, R. B. Hutson, *et al.*, "Systematic evaluation of an atomic clock at $2 \times 10^{-18}$ total uncertainty," Nat. Commun. **6**, 6896 (2015).
10. A. D. Ludlow, M. M. Boyd, J. Ye, *et al.*, "Optical atomic clocks," Rev. Of Mod. Phys. **87**, 637–701 (2015).
11. K. Numata, A. Kemery, and J. Camp, "Thermal-noise limit in the frequency stabilization of lasers with rigid cavities," Phys. Rev. Lett. **93**, 250602 (2004).
12. S. Häfner, S. Falke, C. Grebing, *et al.*, "$8 \times 10^{-17}$ fractional laser frequency instability with a long room-temperature cavity," Opt. Lett. **40**, 2112–2115 (2015).
13. A. Einstein, "Über die von der molekularkinetischen theorie der wärme geforderte bewegung von in ruhenden flüssigkeiten suspendierten teilchen," Ann. der Physik **322**, 549–560 (1905).
14. E. Wiens, Q.-F. Chen, I. Ernsting, *et al.*, "Silicon single-crystal cryogenic optical resonator," Opt. Lett. **39**, 3242–3245 (2014).
15. W.-W. Wang, Z.-A. Chen, H. Zhang, *et al.*, "Design and realization of a 3-K cryostat for a 10-cm ultrastable silicon cavity," Front. Phys. **11**, 1176783 (2023).
16. G. D. Cole, W. Zhang, M. J. Martin, *et al.*, "Tenfold reduction of brownian noise in high-reflectivity optical coatings," Nat. Photonics **7**, 644–650 (2013).
17. D. Kedar, J. Yu, E. Oelker, *et al.*, "Frequency stability of cryogenic silicon cavities with semiconductor crystalline coatings," Optica **10**, 464–470 (2023).
18. S. Amairi, T. Legero, T. Kessler, *et al.*, "Reducing the effect of thermal noise in optical cavities," Appl. Phys. B **113**, 233–242 (2013).
19. S. Horvath, C. Shi, D. Gustavsson, *et al.*, "Slow light frequency reference cavities—proof of concept for reducing the frequency sensitivity due to length fluctuations," New J. Phys. **24**, 033034 (2022).

20. R. Oswald, M. G. Hansen, E. Wiens, *et al.*, "Characteristics of long-lived persistent spectral holes in $Eu^{3+}$:$Y_2SiO_5$ at 1.2 K," Phys. Rev. A **98**, 062516 (2018).
21. R. W. Equall, Y. Sun, R. L. Cone, and R. M. Macfarlane, "Ultraslow optical dephasing in $Eu^{3+}$:$Y_2SiO_5$," Phys. Rev. Lett. **72**, 2179–2182 (1994).
22. F. Könz, Y. Sun, C. W. Thiel, *et al.*, "Temperature and concentration dependence of optical dephasing, spectral-hole lifetime, and anisotropic absorption in $Eu^{3+}$ : $Y_2SiO_5$," Phys. Rev. B **68**, 085109 (2003).
23. M. Tian, T. Chang, K. D. Merkel, and W. R. Babbitt, "Reconfiguration of spectral absorption features using a frequency-chirped laser pulse," Appl. Opt. **50**, 6548–6554 (2011).
24. M. Pomponio, A. Hati, and C. Nelson, "FPGA-based low-latency digital servo for optical physics experiments," in *2020 Joint Conference of the IEEE (IFCS-ISAF),* (2020), p. 1–2.
25. W. Riley and D. A. Howe, "Handbook of frequency stability analysis," NIST (2008). Last Modified: 2021-10-12T11:10-04:00.
26. M. Lindén, D. Gustavsson, A. Walther, *et al.*, "Resetting spectral hole features in Eu:YSO using a highly tunable radio-frequency resonance circuit," (2024). Manuscript in preparation.
27. M. Lindén, D. Gustavsson, K. Shortiss, and L. Rippe, "Highly tuneable in-situ cryogenic switch bank resonator for magnetic field generation at radio-frequencies," (2024). Manuscript in preparation.
28. J. Alnis, A. Matveev, N. Kolachevsky, *et al.*, "Subhertz linewidth diode lasers by stabilization to vibrationally and thermally compensated ultralow-expansion glass fabry-perot cavities," Phys. Rev. A **77**, 053809 (2008).
29. L. S. Ma, P. Jungner, J. Ye, and J. L. Hall, "Delivering the same optical frequency at 2 places - accurate cancellation of phase noise introduced by an optical-fiber or other time-varying path," Opt. Lett. **19**, 1777–1779 (1994).
30. E. D. Black, "An introduction to Pound-Drever-Hall laser frequency stabilization," Am. J. Of Phys. **69**, 79–87 (2001).
31. M. Hopcroft, "allan_overlap," .
32. A. E. Siegman, *Lasers* (University science books, Mill Valley, California, 1986).

# Appendix

## A. Experimental details

The slow light stabilization scheme was realized in an yttrium orthosilicate (YSO, $Y_2SiO_5$) crystal manufactured by Scientific Materials. The crystal was doped to 1 at% with europium ions in natural abundance – approximately equal parts $^{151}Eu^{3+}$ and $^{153}Eu^{3+}$. The sample's dimensions are 14 mm × 15 mm × 21 mm (optical axes $D_1 \times b \times D_2$). The crystal was mechanically polished to minimize the wedge angle between the mirror faces (8 µrad), and then superpolished by Ion Beam Forming (1 $nm_{RMS}$ over a 1 mm diameter beam, 1.37 µrad wedge angle). In the polishing process, a spatial inhomogeneity in the refractive index was discovered which meant we could either make both mirror faces separately flat or the high-reflectivity face absolutely flat and the cavity optically flat in transmission. We selected the second option, and the reported flatness numbers are measured through the crystal. Finally, the front and back faces were coated to 90 % and 99 % reflectivity respectively using Ion Beam Sputtering. A corner was left uncoated for transmission-mode experiments.

For the locking experiments, the crystal was placed on a cradle, vibrationally isolated from the rest of the setup by a 3 mm thick sheet of open-cell polyimide foam. Adjacent to the crystal, but separated from it by a vacuum gap, were a tunable resonant RF antenna for hyperfine erasure, described in Ref. [27], and a sideburner assembly. The sideburner was designed to effectively perform optical pumping throughout the crystal from the side, avoiding standing wave effects. The design is shown in fig. 2 (top left). The burning light was fed into the cryostat via a multimode optical fiber. On the output, the light was collimated by a GRIN lens, reflected by a 90° prism, and onto an engineered diffuser which spread the light out into a vertical line. The light was then scattered through a diffusive piece of a commercially available LED backlight module, which was clad in a reflective film on all sides but the one facing the crystal. This way, the crystal was evenly illuminated by a wide, diffuse beam.

All experiments were performed using a Coherent 699-21 ring laser with rhodamine 6G dye. This laser was stabilized to an external ultra-low expansion glass (ULE) cavity and the linewidth is estimated to be on the order of a few tens of Hz. The ULE cavituy was temperature stabilized close to its zero temperature coefficient point, which gives a low drift rate [28]. The light was passed through a 20 m optical fiber, which on short time scales broadens it to approximately 1 kHz [29], before entering the experimental table. At the crystal, the locking beam had a diameter of approximately 1 mm.

The crystal was temperature stabilized to 1.6 K in a closed cycle cryostat from MyCryoFirm with a 4 K pulse-tube cooled stage and a secondary Joule-Thomson cooled stage with a gas cell for the sample. The crystal was thermally connected to the cell through an injection of 0.1 mbar helium gas.

In order to restore the spectral profile between experiments, the hyperfine ground states were scrambled using an RF erasure technique described and evaluated in Ref. [26]. An RF magnetic field was generated in a coil surrounding the crystal, at the resonance of a tunable resonance circuit, which was tuned to the $|\pm 1/2\rangle \rightarrow |\pm 3/2\rangle$ and $|\pm 3/2\rangle \rightarrow |\pm 5/2\rangle$ transitions in the ground state of each of the two isotopes – four transitions in total – performing repeated $\pi/2$ sweeps for each one in sequence, although for $|\pm 3/2\rangle \rightarrow |\pm 5/2\rangle$ in $^{153}Eu^{3+}$ a $\pi/2$ pulse area could not be achieved due to low oscillator strength and limitations in pulse length and power.

Frequency stabilization was achieved with PDH locking using a digital laser servo and signal generator implemented on a Field Programmable Gate Array (Koheron, alpha-250), marked FPGA in fig. 2 (bottom left). The software is described in Ref. [24]. The FPGA generated a 40 MHz signal to drive a frequency shifting acousto-optic modulator (Isomet, M1201-SF40). It also acted as a local oscillator supplying a 10 kHz signal to a fiber-coupled electro-optic modulator (Jenoptik, PM594), which generated side bands at a modulation of depth $\beta \approx 1.08$ in

line with the optimum derived in Ref. [30]. The reflected light off the crystal was detected by a photo diode (Hamamatsu, S5973-02) connected to a transimpedance amplifier (NF, SA-606F2) and fed back into the FPGA, where a digital phase detector and low pass filter converted the modulation into an error signal. This error signal was then fed to a digital PID servo controlling a Numerically Controlled Oscillator (NCO) connected to a DAC. This signal shifted the frequency out of the acousto-optic modulator accordingly.

The feedback signal was used to determine linear drift, as well as overlapping Allan deviation using the Matlab function `allan_overlap` [31]. To uncouple the power-induced drift from signal power effects, a neutral density filter was inserted before the reflection detector for the higher intensity experiments which compensated the increased power, meaning that only the drift rate, and not the noise, should be affected.

## B. The effect of window frequency on relative mode frequency

In this appendix we derive the mode frequency relative to the center of a spectral transmission window, as a function of that window's center frequency relative to the inhomogeneous absorption profile. The resonance condition for transmission through a cavity of length $L$ is

$$2L = q\lambda \tag{7}$$

with resonant wavelengths $\lambda$ and an integer $q$.

$\lambda = \frac{c_0}{n\nu}$ gives

$$q = \frac{2nL\nu}{c_0} \tag{8}$$

We define the frequency for the peak of the inhomogeneous profile $\nu_0$, a window center frequency $\nu_{\text{win}}$ as the offset from $\nu_0$ to the center of the window, and a mode frequency $\nu_{\text{mode}}$ which is the frequency of the mode relative to the center of the window. The absolute mode frequency is then $\nu = \nu_0 + \nu_{\text{win}} + \nu_{\text{mode}}$. Similarly, we write the refractive index $n$ as the sum of the host refractive index $n_0$, a contribution $\Delta n_{\text{ih}}(\nu_{\text{win}})$ from the inhomogeneous profile and a contribution $\Delta n_{\text{win}}(\nu_{\text{mode}}) = n'\nu_{\text{mode}}$ from the linear dispersion with coefficient $n'$ in the window. This allows us to rewrite eq. (8) as

$$\left(1 + \frac{\Delta n_{\text{ih}}}{n_0} + \frac{\Delta n_{\text{win}}}{n_0}\right)\left(1 + \frac{\nu_{\text{win}}}{\nu_0} + \frac{\nu_{\text{mode}}}{\nu_0}\right) = \frac{q}{\nu_0}\frac{c_0}{2n_0L} = \frac{q\nu_{\text{FSR}}}{\nu_0} \,. \tag{9}$$

Here $\nu_{\text{FSR}}$ is the free spectral range of the cavity without the presence of the atomic line. Recognizing that each of the non-unity terms in the left-hand side is much smaller than 1, their second-degree combinations can be neglected, which leaves

$$1 + \frac{\Delta n_{\text{ih}}}{n_0} + \frac{\Delta n_{\text{win}}}{n_0} + \frac{\nu_{\text{win}}}{\nu_0} + \frac{\nu_{\text{mode}}}{\nu_0} = \frac{q\nu_{\text{FSR}}}{\nu_0} \,. \tag{10}$$

We introduce an integer $\Delta q$ and a real number $r \in [-0.5,\, 0.5)$ such that

$$q\nu_{\text{FSR}} = \nu_0 + (\Delta q + r)\,\nu_{\text{FSR}} \,. \tag{11}$$

This amounts to counting the number of free spectral ranges from the cavity mode nearest to $\nu_0$, instead of the absolute mode number. Equation (10) simplifies to

$$\frac{\Delta n_{\text{ih}}}{n_0} + \frac{\Delta n_{\text{win}}}{n_0} + \frac{\nu_{\text{win}}}{\nu_0} + \frac{\nu_{\text{mode}}}{\nu_0} = (\Delta q + r)\,\frac{\nu_{\text{FSR}}}{\nu_0} \,. \tag{12}$$

$$\Delta n_{\text{ih}}\nu_0 + n_0\nu_{\text{win}} + \nu_{\text{mode}}\,(n_0 + n'\nu_0) = (\Delta q + r)n_0\nu_{\text{FSR}} \tag{13}$$

We separate out $\nu_{\text{mode}}$,

$$\nu_{\text{mode}} = \frac{(\Delta q + r) n_0 \nu_{\text{FSR}} - n_0 \nu_{\text{win}} - n_{\text{ih}}(\nu_{\text{win}}) \nu_0}{n_0 + n' \nu_0} \tag{14}$$

From Ref. [19], we have the group refractive index

$$n_g = n_0 + n' \nu_0 \approx \frac{c_0 \alpha}{\pi^2 \Gamma_{\text{win}}} \, . \tag{15}$$

Using the complex susceptibility of a Lorentzian absorption line (Ref. [32, Chapter 2.4]), the inhomogeneous profile's contributions are derived to

$$\begin{aligned} \alpha &= \frac{\alpha_0 \Gamma_{\text{ih}}^2}{4\left(\nu_{\text{win}}^2 + \frac{\Gamma_{\text{ih}}^2}{4}\right)} \\ n_{\text{ih}}(\nu_{\text{win}}) &= -\frac{\nu_{\text{win}} \Gamma_{\text{ih}} \alpha_0 c_0}{8\pi \nu_0 \left(\nu_{\text{win}}^2 + \frac{\Gamma_{\text{ih}}^2}{4}\right)} \end{aligned} \tag{16}$$

Combining eqs. (14) to (16) gives

$$\nu_{\text{mode}} = (\Delta q + r) \frac{n_0}{n_g} \nu_{\text{FSR}} - \frac{n_0}{n_g} \nu_{\text{win}} + \frac{\pi \Gamma_{\text{win}}}{2 \Gamma_{\text{ih}}} \nu_{\text{win}} \tag{17}$$

The three terms in eq. (17) predict three effects on the mode frequency as the window is moved. The first is an effective free spectral range scaled down by the slow light factor $n_0/n_g$ (note that $(\Delta q + r)$ takes values with integer spacing). The second effect is that as $\nu_{\text{win}}$ changes, the change in $\nu_{\text{mode}}$ is that change scaled down by the same slow light factor. The final term predicts a distortion due to the presence of the inhomogeneous line itself. This effect does not depend on the peak absorption $\alpha_0$, but the slope addition scales with the ratio between the window width and the inhomogeneous linewidth. In our experiment, this makes the last term about 10 % as large as the second.

### C. Angle sensitivity

Flat mirror cavities have degenerate transversal modes, so any fluctuations in angle of incidence are translated into shifts in mode frequency. In this appendix we derive an expression for this dependence which includes dispersion in the cavity, showing that strong dispersion heavily reduces the sensitivity.

The phase accumulated for a light wave of frequency $\nu$ traveling a distance $z$ through a crystal with refractive index $n$ is

$$\Delta\phi(z) = \frac{2\pi}{c_0} n \nu z \, . \tag{18}$$

From Snell's law and simple trigonometry, the single-pass path length through a crystal of length $L$ with refractive index $n$ for a beam with incidence angle $\theta$ from vacuum is

$$z = L \sqrt{1 - \frac{1}{n^2} \sin^2 \theta} \, , \tag{19}$$

so the single-pass phase is

$$\Delta\phi = \frac{2\pi}{c_0} n \nu L \sqrt{1 - \frac{1}{n^2} \sin^2 \theta} \, . \tag{20}$$

Staying resonant as the angle varies necessarily implies a constant $\Delta\phi$. This means we can equate the expression with one for normal incidence and unshifted frequency, where $n = n_0$, $\nu = \nu_0$ and $\theta = 0$:

$$n\nu\sqrt{1 - \frac{1}{n^2}\sin^2\theta} = n_0\nu_0 \ . \tag{21}$$

We introduce $\nu_{\text{mode}} = \nu - \nu_0$ and assume linear dispersion, $n = n_0 + n'\nu_{\text{mode}}$. Furthermore we assume a small incident angle to simplify $\sqrt{1-x} \approx 1 - x/2$

$$\left(1 + \frac{n'\nu_{\text{mode}}}{n_0}\right)\left(1 + \frac{\nu_{\text{mode}}}{\nu_0}\right)\left(1 - \frac{\sin^2\theta}{2(n_0 + n'\nu_{\text{mode}})^2}\right) = 1 \tag{22}$$

The non-unity terms in the parentheses are much smaller than 1, so higher order terms can be neglected, leaving

$$(n_0 + n'\nu_0)\,\frac{\nu_{\text{mode}}}{\nu_0} = n_0\frac{\sin^2\theta}{2n_0^2} \tag{23}$$

and finally

$$\frac{\nu_{\text{mode}}}{\nu_0} = \frac{n_0}{n_0 + \nu_0\frac{\mathrm{d}n}{\mathrm{d}\nu}}\frac{\sin^2\theta}{2n_0^2} \ . \tag{24}$$

Just like with length changes, the angle sensitivity scales with the group refractive index $n_g = n_0 + \nu\frac{\mathrm{d}n}{\mathrm{d}\nu}$.

# Paper III

M. Lindén, D. Gustavsson, K. Shortiss and L. Rippe
"Highly tuneable in-situ cryogenic switch bank resonator for magnetic field generation at radio-frequencies", *Manuscript in preparation* (2024)

# Highly tuneable in-situ cryogenic switch bank resonator for magnetic field generation at radio-frequencies

M. Lindén,[1,2] D. Gustavsson,[1] K. Shortiss,[1] and L. Rippe[1,a)]
[1)] *Department of Physics, Lund University, Lund, Sweden*
[2)] *Measurement Science and Technology, RISE Research Institutes of Sweden, Borås, Sweden*

(Dated: 31 July 2024)

This study introduces an adaptive cryogenic design for magnetic field generation at radio-frequencies by integrating in-situ tuning of matching and resonance frequency using capacitor switch banks. The resonator design allows for semi-continuous tuning and a very wide tuning range of 25–140 MHz (560 %) while operating at 1.5 K. The loaded Q-factor is maintained at 50 with an magnetic field generating efficiency ranging from 50–80 $\mu T/\sqrt{mW}$ up to 70 MHz, after which a degradation in performance is observed. We provide a circuit analysis of estimating the matching and resonance frequency which is then applied to generate a data bank of usable switch combinations that includes information on matching conditions, resonance frequency, and magnetic fields available.

## I. INTRODUCTION

Low loss RF resonators operating at cryogenic temperatures can be advantageous within various applications including medical imaging using MRI and NMR spectroscopy where higher signal to noise ratios can be obtained using superconducting probes, and in ion traps which require about 100 V to sufficiently trap ions[1].

Recently rare earth ions doped into a crystal lattice have been identified as a potential platform for quantum computing, quantum memories, and quantum repeaters due to the very long coherence and storage times that can be realized in these materials.[2–4] The designs used to drive transitions in rare earth materials have used non resonant coils without tuning for Raman heterodyne detection,[5] and single frequency resonant circuits[6]. Non-resonant coils are highly inefficient when used in the radio-frequency range and without adequate capability of tuning applications are limited to one or two frequencies. Tunable resonators for cryogenic applications have been difficult to realise as they need to be efficient, handle high RF powers, and allow for wide frequency tuning.

When designing resonators for cryogenic applications below 4 K, size and cooling power constraints makes LC resonators a natural choice as they are compact and power efficient. To reduce cryostat heating further, matching can be performed in close proximity to the resonance circuit. This avoids making the long cables running in to the cryostat part of the resonance circuit, which will result in Joule heating due to high voltage across the cables. Low RF power can therefore run through lengthy cables in to the cryostat, after which the voltage is be amplified by the resonance circuit.

As the electrical properties of circuit components change during cooling from room temperature to cryogenic temperatures this affects the matching conditions which can be difficult to predict. This leads to situations where you are required to temperature cycle the cryostat to optimize the parameters, or run under sub-optimal conditions. It is therefore important to be able to tune the matching frequency.

Passive tuning designs using trimmer capacitors[1] or inductive coupling[7,8] where the capacitance and inductance can be set before cooling down, and ex situ trimmer matching capacitors[9] can be unpractical and power inefficient due to reasons mentioned above. In-situ tuning for matching has been demonstrated with commercially available direct bandgap varactors.[10,11] This approach offers continuous tuning by changing the width of the depletion region by applying a DC voltage. Larger tuning ranges typically means higher nonlinear response which can induce harmonics in the resonator as the AC-component in the RF field across the varactor change the capacitance.[10] This limits the maximum power that can be used.

To achieve large tuning ranges, resonator tuning can be performed. Without means for adjusting circuit matching, care has to be taken in the design step to consider circuit response in the desired frequency range at low temperatures. Such designs have been realized for high Q filters using mechanical superconducting MEMS switches in microstrip gap[12] and switch bank[13] configuration, reaching a respective tuning range of 20 % and 12 %. Due to the high Q achievable, these resonators are particularly suitable for sensing applications. However, these switches are unfortunately not yet commercially available.

In this study we present a cryogenic RF resonator design that utilize in-situ tuning for both matching and resonator frequency at 1.5 K, by employing capacitor banks using commercially available high-power MEMS switches. The ability to handle very high voltages (>100 volts) make the switches suitable for frequency tuning in resonance circuits where the voltage gain can be high. The capacitor bank allows for semi-continuous and a very wide tuning range ($f/f_0$) of $\geq$ 560 % while maintaining a Q-value of 50 up to a frequency of 70 MHz. The magnetic field generation efficiency in this range was 50–80 $\mu T/\sqrt{mW}$. The following sections will describe the resonator design and performance characteristics in more detail.

[a)] Author to whom correspondence should be addressed.
e-mail: lars.rippe@fysik.lth.se

## II. CIRCUIT DESIGN

The circuit design can be divided in to two parts; the matching capacitance $C_m$ (responsible for matching source and load impedance), and the *RLC* resonator (which allows for a high current amplitude on resonance). Here $L$ is the inductance, $C$ the capacitance, and $R$ the effective resistance which accounts for any dissipation in the resonator. The circuit schematic and connection interface is shown in Fig 1. For a bare *RLC* resonator without the matching capacitance, the resonance frequency is given by

$$\omega_0 = 1/\sqrt{L_{\text{coil}}C_r} \tag{1}$$

Here the inductance $L$ is assumed to be dominated by the coil inductance $L_{\text{coil}}$ whereas $C_r$ is given by the switch bank capacitance. On resonance the load impedance is purely real (resistive) due to the reactance of $L_{\text{coil}}$ and $C_r$ being equal in magnitude but opposite in phase. The resistance $R$ is in general low ($< 1\,\Omega$) when the coil is made out of high conductivity materials like copper. Since the impedance of the transmission line is usually chosen to be $50\,\Omega$ there will be an impedance mismatch which can lead to signal reflections at the interfaces, resulting in only a small part of the power being transferred to the resonance circuit. In order to reduce reflections it is necessary to add a matching network to the circuit.

A common matching configuration is the "L" matching network which consists of two reactive components where one is placed in series and the other in parallel. This configuration shifts the resonance until matching can be performed with the parallel component at $\omega_0$. However, it is also possible to operate the resonator at a frequency different from the original resonance frequency where matching can be performed with one parallel reactance.[1] Using just one reactance in parallel ($C_m$), was the choice in this design. An added benefit is that changing the matching capacitance allows for fine tuning of the resonance frequency, if a reduction in magnetic field amplitude is acceptable.

To generate high magnetic fields it is necessary that the current $I$ in the circuit is large. The magnetic field from a coil is given as $B \propto NI$ where $N$ is the number of turns of the coil with the proportionality factor being coil geometry dependent. On resonance, the maximum circuit current amplitude is given by

$$I_{\text{max}} = \frac{V_{\text{coil}}}{X_{\text{coil}}} = \frac{V_{\text{coil}}}{\omega_0 L_{\text{coil}}} \tag{2}$$

with $V_{\text{coil}}$ being the voltage across the coil and $X_{\text{coil}}$ the reactance of it. The voltage step-up across the coil is given by the Q-factor as $V_{\text{coil}} = QV_{\text{in}}$ where $V_{\text{in}}$ is the circuit input voltage. The Q-factor is, however, also dependent on the reactance:

$$Q = \omega_0 L_{\text{coil}}/R \tag{3}$$

so that the resulting maximum current will be determined by

$$I_{\text{max}} = V_{\text{in}}/R \tag{4}$$

The conclusion is therefore to minimize $R$ in the resonator. Of note is that maximizing the Q-factor does not necessarily lead to a high current in the circuit as high Q-factors can results from the product of $\omega_0 L_{\text{coil}}$. To reduce the equivalent series resistance we can consider some of the main contributors; the coil, switches, and PCB copper traces.

Coil resistance can be minimized by choosing superconducting or oxygen free copper (OFC) coil as the resistance of these materials is either zero or very low during cryogenic operation. As the switches (and PCB traces) are not superconducting it was reasoned that it would not be a significant improvement using a superconducting coil over oxygen free copper (OFC) with a high Residual Resistance Ratio (RRR). The coil was therefore made with OFC (Luvata, OFE-OK®) (RRR = 400) and then soldered on to the PCB board. A specific coil geometry ($a = 17\,\text{mm}$, $b = 16\,\text{mm}$, $l = 20\,\text{mm}$, diameter $d = 1\,\text{mm}$) was used in this case as it was restricted to dimensions of an ion doped crystal used for our application. The number of turns was set to $N = 5$ given these restraints. For the highest frequency considered in this study (140 MHz), the AC resistance for such a coil was estimated to be approximatley $16\,\text{m}\Omega$ with $R_{\text{coil}}$ given as

$$R_{\text{coil}} = \frac{\rho l_{\text{tot}}}{A_{\text{eff}}} \tag{5}$$

$$A_{\text{eff}} = \delta \pi d \tag{6}$$

$$\delta = \sqrt{\frac{2\rho}{\omega\mu}} \tag{7}$$

where $\rho$ is the conductivity (at 1.5 K), $l_{\text{tot}}$ the physical wire length, $A_{\text{eff}}$ the effective cross sectional area for current, and $\delta$ the skin depth. The proximity effect resistance contribution was assumed to be small as the packing factor $Nd/l$ was below 50 %.[14]

Another important aspect of the circuit was tunability. As this circuit was intended to be used to drive the hyperfine transitions in Eu:YSO there was a requirement to be able to reach frequencies within a window of 34.5 MHz and 119.2 MHz. Parasitic capacitance in the circuit will determine what the maximum inductance can be given a requirement on the maximum operating frequency and the lowest capacitance available for $C_r$. The circuit was simulated in LTSpice using lumped models for the MEMS switches in order to choose suitable values for the capacitor bank. Simulations accounted for an estimated parasitic capacitance of 2.4 pF including contributions from electronic components, coil, coil proximity to the 1.5 K cylinder wall (grounded) and PCB trace proximity to ground in the resonance circuit. All the capacitors were of type C0G (NP0) due to the proven stable dielectric response at cryogenic temperatures[15]. The switch used for tuning was MM5130, commercially available from MenloMicro.

Parasitic capacitance was estimated from the coil, transmission line proximity to ground plane, and other components which could potentially reduce the resonance frequency. Due to the off capacitance of each pole in the switch being very low (15 fF) it was possible to fit several switches in parallel while avoiding larger reductions in resonance frequency. Both the matching, $C_m$, and resonator, $C_r$, capacitance consisted of a bank of capacitors connected in parallel with a total of 8 and 16 capacitors, respectively. This allowed for $2^{16}$ combi-

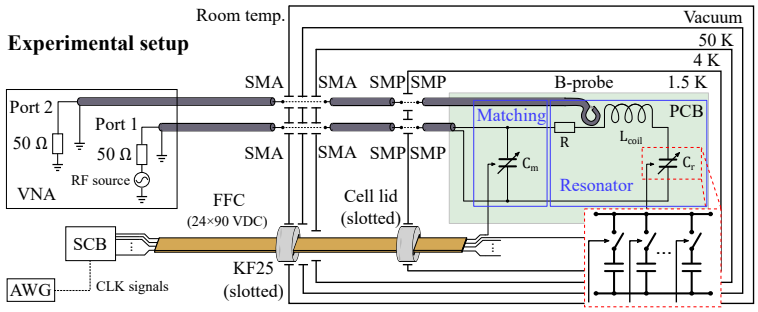


FIG. 1. Cryogenic resonator design. The schematic shows the instrument and cryostat interface connections to the PCB circuit that resides inside a 1.5 K cell. Power to the circuit is supplied via Port 1 on the VNA with the magnetic probe connected to Port 2. In situ matching of the circuit was performed by the matching capacitor, $C_m$. The resonator is described by the lumped components $R$ (equivalent series resistance), $L_{coil}$ and $C_r$. Both $C_m$ and $C_r$ is composed of parallel capacitors which are switched in using DC control lines. The DC lines are fed through the cryostat using a flexible flat cable (FFC).

nations for the resonance tuning and $2^8$ combinations for the matching. With the large number of combinations for matching and resonance frequency tuning, the tuning can be considered to be semi-continuous, as discussed in more detail in section III C.

Each capacitor was switched in using a single pole switch, actuated electrostatically by applying 87 V through a DC control line, thus requiring 24 lines in total. To provide a path to ground for any DC bias voltage buildup 10 MΩ resistors were added. The smallest capacitance values for the resonator was obtained by forming copper pads on the two layer PCB. The capacitance for a given pad size and parallel plate distance was simulated in COMSOL to account for electric field edge effects.

## III. EXPERIMENTAL RESULTS

### A. Circuit characteristics

In order to estimate the resonance frequency and required matching capacitance it was first necessary to retrieve a value for the inductance in the circuit. The inductance from the coil, $L_{coil}$ was assumed to be much larger than any stray inductance in the circuit so that $L \approx L_{coil}$ in eq. 1. To estimate $L_{coil}$ initially, $C_r$ was set to a large capacitance value (106 pF) so that any parasitic capacitance contribution could be considered low ($C_r \gg C_p$), with $C = C_r + C_p$. The validity of this assumption is discussed further below.

When measuring the resonance frequency it is important to note that $\omega_{m,opt}$ (resonance frequency at optimal matching) and $\omega_0$ (resonance for a bare RLC circuit) can differ. This can be used for fine-tuning of the resonator, as we will show in the next section. Although having no matching capacitance results in the smallest frequency difference, the value of $C_m$ was chosen to be approximately 30 % of the optimal matching capacitance in order to identify the magnetic field resonance peak more easily. The shift in frequency going from 30 % of optimal matching capacitance to optimal capacitance shifted the resonance 3.2 %, which should give a rough estimate of the error. In most cases $\omega_0$ can be approximated to $\omega_{m,opt}$, which is also what was done here for simplification. With $\omega_0/2\pi$ measured to 26.9 MHz, $L_{coil}$ was found to have an inductance of 0.33 µH.

After the circuit had been fabricated the parasitic capacitance is not expected to change. It is therefore possible to calibrate for this offset. In Fig. 2 the magnetic field resonance frequency at best match have been plotted for different switched in values of $C_r$. To determine $C_p$ a least squares fit was performed using equation eq. 1 and the measured value for $L_{coil}$. The parasitic capacitance was found to be 4.4 pF, slightly higher than the predicted 2.4 pF. Thus, when calculating $L_{coil}$ at $C_r = 106$ pF the resonance should only be shifted by about 4.2 %.

The matching capacitance was obtained directly by measuring $C_{m,opt}$ in the frequency range of interest and then performing a polynomial fit to it to make predictions in a wider frequency range. The model was updated iterativeley after more values of $C_{m,opt}$ were measured for better predictions.

An equivalent approach is to measure the Q-value from the magnetic field while matched, and retrieve $R$ using eq. 3. The matching capacitance $C_m$ can then be obtained through the parameter $\alpha$ and matching reactance $X_m$ by the following re-

lationships (as discussed by Gandolfi et. al.[1])

$$\alpha = R_s/R - 1 \quad (8)$$

$$X_m = \frac{R_s}{\sqrt{\alpha}} \quad (9)$$

$$C_m = \frac{1}{\omega_m X_m} \quad (10)$$

where $R_s$ is the characteristic impedance. For more information on estimating $C_m$, see section V B in supplementary.

### B. Switch bank tuning

Here we present our findings on matching and resonator tuning using a switch capacitor bank, by setting $C_m$ and $C_r$ respectively (Fig. 2). To test the tuning behaviour of the circuit $C_r$ was stepped in between 0.036 pF and 106 pF where each $C_r$ value had 20–30 different configurations of $C_m$, centered around $C_{m,opt}$.

In some cases it will not be possible to reach particular resonance frequencies using tuning with $C_r$ only. However, with knowledge of $C_{m,opt}$ for a given frequency, matching sweeps can be used to fine tune the resonator. For a fixed value of $C_r$, a set of matching capacitance's can be chosen centered around the optimal matching capacitance to shift the resonance frequency. Such a sweep is demonstrated in the inset of figure 2 in the case where $C_r = 62.32\,\text{pF}$. Indeed, tuning the circuit this way will affect the matching performance and reflections present (S11). Monitoring the magnetic field it is possible to set a constraint on allowed detuning from both imperfect matching and simply running the signal generator different from set resonance (see section III C for further discussion). The results show that tuning can be performed over a large frequency range (25 to 140 MHz) while also allowing for fine tuning and matching using the matching capacitor bank. By chaining and overlapping resonances it is possible to perform semi-continuous tuning even though the switches have discrete steps.

The switches were found to be reliable without sticking or failure in a helium environment inside the cell (0.1 mbar, 1.5–2.0 K) if the switch was set to open state after a switch sequence. Leaving the switch in a closed state would sometimes cause the switch to stick, although heating the cryostat to about 25 K released them. With a switch delay of about 3 ms there was enough time to avoid hot switching (having RF-power on while setting a switch). Without the delay $\tau = R_{bias}C_{bias} = 3\,\text{ms}$ set on the DC bias line, switching should in principle be possible in the µs range according to the manufacturer. However, in our experiments we observed an extra switch delay of approximately 50 ms when cold compared to room temperature. The cause of this delay was not investigated further but may have been caused by ice forming on the switch pole as the switch is hermetically sealed with an air mixture inside. With an initially high resistance from ice formation we would expect a slight delay before the heat dissipated from the RF-field cause the ice to melt (turning the switch on).

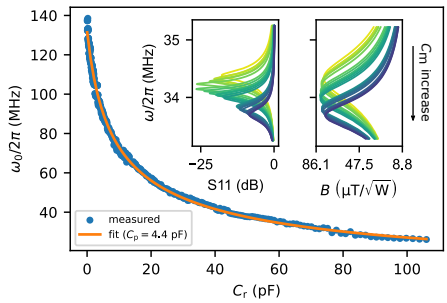


FIG. 2. Tuning functionality. Resonator tuning was performed by setting the resonator capacitance, $C_r$. The resonance frequency obtained follows that of a standard RLC-resonator when using best match values for $C_m$. Inset figure shows how the return loss and magnetic field resonance can be shifted using matching capacitors, for a given value of $C_r = 62.32\,\text{pF}$.

### C. B-field efficiency

In the previous section, we demonstrated how to predict the resonance frequency and matching conditions using switch banks. Once an approximate estimate of these parameters is obtained, it enables the mapping of switch combinations to create a database of usable configurations. Due to the mechanical switch being very stable the resonance frequency or matching condition does not change noticeably once cryogenic temperatures have been reached. The obvious benefit is that a set of configurations can be recorded with precise information at known frequencies, including the magnetic field, matching performance and Q-value for the resonance peak. For a given resonance peak one can set limits for frequency detuning $\Delta\omega$ where the magnetic field has been reduced by 3 dB in relation to the maximum field $B_{max}$. How large the detuning can be will then be determined by the Q-factor. Consequently, high Q peaks therefore require a higher density of resonances in order to overlap the detuning range of different resonance peaks with the opposite being true for low Q peaks. A trade-off thus exists between how continuous the tuning is and what maximum magnetic field can be achieved.

In Fig. 3 the maximum magnetic field at a given resonance frequency have been recorded with a 3 dB detuning constraint using a frequency resolution of 11.3 kHz. The underlying data consists of $N = 16.1 \times 10^3$ peaks with it's center frequency set to be separated evenly in the range of 25–140 MHz using eq. 1 and 9. As expected the highest magnetic field and Q-values were observed in the lower end of the frequency range due to a lower equivalent resistance. A correlation analysis was performed on the $B$, $C_m$, and $C_r$ residuals obtained after removing the approximate linear trend. The correlations showed that the magnetic field had a positive correlation with $C_m$ (0.46) and a negative correlation with $C_r$ (−0.41) in the frequency range

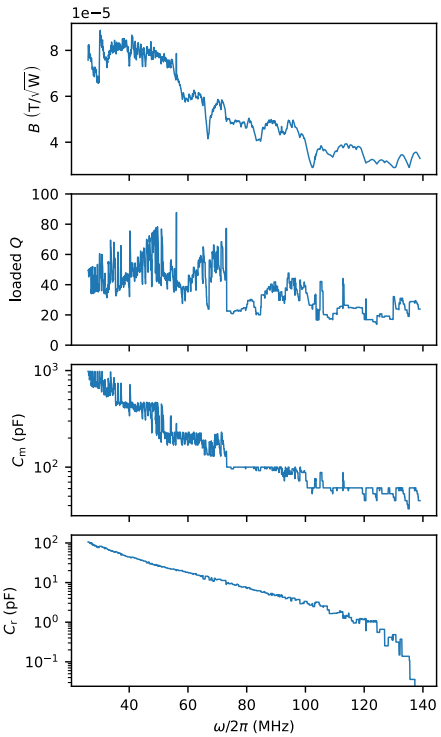


FIG. 3. Magnetic field generation efficiency across the frequency range 25–140 MHz. The magnetic field and Q-value was in general higher in the lower frequency range and lower for the highest frequencies. The magnetic field was found to be positively correlated with the Q-value (0.43) and the matching capacitance $C_m$ (0.46), and negatively correlated with the resonance capacitance $C_r$ (−0.41).

25–120 MHz, indicating that the resistance decreases with $C_m$ and increases with $C_r$. At a given frequency $\omega_m$ we see from eq. 8–10 that $R$ naturally has to decrease for increasing $C_m$. The reason for increasing resistance with $C_r$ is more difficult to pinpoint but may have been due to a longer resonance loop trace path length.

## IV. CONCLUSIONS

In this work we report on a cryogenic capacitor switch bank resonator design with in situ resonator and matching tuning. By implementing a large number of switch combinations it was possible to perform semi-continuous tuning across a tuning range spanning 25–140 MHz. By predicting matching and resonator tuning parameters we were able to generate a data bank of usable configurations including information on matching conditions, the resonance frequency, and resulting magnetic field. Setting a detuning constraint where the signal had been attenuated by 3 dB allowed for overlapping of resonance peaks, which is why the tuning can be considered semi-continuous. The loaded Q-value varied from about 30 at 140 MHz to 50 in the lower frequency span, close to 25 MHz.

Although this resonance circuit was designed with a specific frequency ranges in mind targeting the rare earth metal hyperfine transitions of europium, the circuit can be considered flexible as it should be simple to swap the capacitor values to change operating range.

[1]D. Gandolfi, M. Niedermayr, M. Kumph, M. Brownnutt, and R. Blatt, "Compact radio-frequency resonator for cryogenic ion traps," Review of Scientific Instruments **83** (2012), 10.1063/1.4737889.
[2]N. Ohlsson, R. Krishna Mohan, and S. Kröll, "Quantum computer hardware based on rare-earth-ion-doped inorganic crystals," Optics Communications **201**, 71–77 (2002).
[3]J. H. Wesenberg, K. Mølmer, L. Rippe, and S. Kröll, "Scalable designs for quantum computing with rare-earth-ion-doped crystals," Physical Review A - Atomic, Molecular, and Optical Physics **75**, 1–7 (2007).
[4]A. Walther, B. Julsgaard, L. Rippe, Y. Ying, S. Kröll, R. Fisher, and S. Glaser, "Extracting high fidelity quantum computer hardware from random systems," Physica Scripta T **T137** (2009), 10.1088/0031-8949/2009/T137/014009, arXiv:1001.1664.
[5]J. J. Longdell, A. L. Alexander, and M. J. Sellars, "Characterization of the hyperfine interaction in europium-doped yttrium orthosilicate and europium chloride hexahydrate," Physical Review B - Condensed Matter and Materials Physics **74**, 1–7 (2006).
[6]R. Lauro, T. Chanelière, and J. L. Le Gouët, "Adiabatic refocusing of nuclear spins in Tm3+:YAG," Physical Review B - Condensed Matter and Materials Physics **83**, 1–7 (2011).
[7]J. D. Siverns, L. R. Simkins, S. Weidt, and W. K. Hensinger, "On the application of radio frequency voltages to ion traps via helical resonators," arXiv:arXiv:1106.5013v3.
[8]M. V. Gulyaev, O. S. Pavlova, D. V. Volkov, E. G. Sadykhov, N. V. Anisimov, and Y. A. Pirogov, "Application of copper plates for frequency tuning of surface wired and wireless MRI coils," Journal of Magnetic Resonance **309** (2019), 10.1016/j.jmr.2019.106626.
[9]A. Holzäpfel, J. Etesse, K. T. Kaczmarek, A. Tiranov, N. Gisin, and M. Afzelius, "Optical storage for 0.53 s in a solid-state atomic frequency comb memory using dynamical decoupling," New Journal of Physics **22**, 0–13 (2020), arXiv:1910.08009.
[10]M. Schubert, L. Kilzer, T. Dubielzig, M. Schilling, C. Ospelkaus, and B. Hampel, "Active impedance matching of a cryogenic radio frequency resonator for ion traps," (2022), 10.1063/5.0097583.
[11]J. Koivuniemi and M. Krusius, "Parametric ampli " cation with a high- Q LC resonator," **288**, 2147–2148 (2000).
[12]R. R. Benoit and N. Scott Barker, "Superconducting Tunable Microstrip Gap Resonators Using Low Stress RF MEMS Fabrication Process," IEEE Journal of the Electron Devices Society **5**, 239–243 (2017).
[13]S. S. Attar, S. Setoodeh, R. R. Mansour, and D. Gupta, "Low-temperature superconducting DC-contact RF MEMS switch for cryogenic reconfigurable RF front-ends," IEEE Transactions on Microwave Theory and Techniques **62**, 1437–1447 (2014).
[14]A. W. Lotfi and F. C. Lee, "Proximity losses in short coils of circular cylindrical windings," PESC Record - IEEE Annual Power Electronics Specialists Conference , 1253–1260 (1992).
[15]M. J. Pan, "Performance of capacitors under DC bias at liquid nitrogen temperature," Cryogenics **45**, 463–467 (2005).
[16]*Integrated circuits – Measurement of electromagnetic emissions, 150KHz to 1GHz – Part 6: Measurement of conducted emissions – Magnetic probe method.*, 61967th ed. (IEC).

## V. SUPPLEMENTARY

### A. Experimental setup

In order to measure the performance of the circuit a VNA (V2/SAA2, NanoRFE) was connected as source with an output impedance of 50 Ω. The RF signal from Port 1 was carried through coaxial cables in to a SMA interface on the closed cycle cryostat (Optidry250, MyCryoFirm) directed in to the 1.5 K cell where the PCB circuit was situated. This transmission line used three different types of cables where the first one leading up to the cryostat was a standard 3 m SMA cable (TMS, LMR-100A-PVC), the second a 305 mm SMA-SMP cable (897621402, Molex) going from the 4K plate to the 1.5K which had an estimated heat transfer of 2.3 mW. The last cable (095-725-120-003, Amphenol) was a 76.2 mm hand formable SMP-SMP cable connecting the circuit to the 1.5 K cell. Port 2 of the VNA was used to measure the magnetic field generated from the coil and was connected using the same cable types as for Port 1, with the difference being that a single turn magnetic field probe was connected to the cell instead. The probe was placed 13 mm from the center of the coil. A Short, Open, Load, and Through (SOLT) standard calibration for the VNA was performed at the 1.5 K cell interface. The cables were thermalized on the shields going in to the inner cell.

The single loop magnetic RF probe was manufactured from a 50 Ω coaxial cable and made to have the same cross sectional square area as the coil. (see IEC[16]). Before placing the probe in the cryostat a relative calibration was done against another calibrated magnetic field probe (Tekbox, TBPS01 H10), in the frequency range of interest, to relate the transmission coefficient S21 to a magnetic field. The magnetic field was calculated as

$$B_{\text{field}} = \frac{B_0}{\sqrt{P_0}} 10^{(\log_{10}(|S21(\omega)|) - \Delta_{\text{adj}}(\omega)/20)} \tag{11}$$

with $B_0$ and $P_0$ referenced at 1 μT and 1 mW. $\Delta_{adj}(\omega)$ was the adjustment factor for the cryostat probe. With the magnetic probe located outside the coil the field will be reduced. To compensate for this effect the field was recalculated to the center point of the coil using eq. S16 (supplementary section V B).

A switch control board (SCB) interface was manufactured using a high voltage serial to parallel converter (HV3418PG-G, Microchip Technology) to generate the voltage required for switching (87 V) and to set the switch state of all switches. This SCB interface was located outside the cryostat at ambient temperature. The control interface received 6 MHz clock and serial data signals from an arbitrary wave form generator (AWG520, Tektronix) to load the output state. Setting an arbitrary switch state took 10.6 μs . As switching with this speed was not necessary in our application, 3 MΩ resistors were added to each control line for safety reasons, which added a switch delay of approximately 3 ms. A pre-programmed sequence list of switch states could be uploaded to the AWG which allow for time-synchronization between the switches and the RF source.

Control voltages were outputted on a polyimide FFC cable (15014-0637, Molex) and fed through a KF-flange. The KF-flange was machined with a 10 mm slot where the 9.5 mm FFC cable was placed and glued using cryogenic epoxy (Stycast 2850FT, E&C). The FFC cable was then thermalized on each shield before reaching the 1.5 K cell. The 1.5 K cell slot FFC feed-through was fabricated in the same manner. Heat transfer from the FFC cable was estimated to be 2.0 mW.

The FFC feedthough is a very compact way of getting many control lines into the cryostat (capacity of 37 DC lines in this case). No leaks were detected after cycling the cryostat three times.

### B. Circuit analysis

#### 1. Estimating matching capacitance

The best match configuration for the circuit was sampled at a few different points in the frequency range of interest. Initially, $C_{\text{m,opti}}$ predictions could be estimated by curve fitting these points (Fig. 4 a)). The matching capacitance was then stepped, centered around the predicted values, to measure actual $C_{\text{m,opti}}$. Once $C_{\text{m,opti}}$ had been measured it was stored in a data bank for later use due to the stable nature of mechanical switches.

Optimal matching capacitance can also be obtained through its relation to a given Q-value (eq. 3 and eq. 8–10). In the case where Q-values have been measured a similar procedure can therefore be used (shown in Fig. 4 b)). By solving for $R$, the parameter $\alpha$ can be used to calculate $C_{\text{m}}$ directly. The calculated values for $C_{\text{m}}$ are shown in Fig. 4 c) (orange trace) where they have been compared to measured values $C_{\text{m,opti}}$ (blue trace). The overlap between measured and calculated values was good for the upper frequency span with a slight deviation in the lower range.

#### 2. Magnetic field probe measurements

Measuring the magnetic field with a probe placed a distance from the edge of the coil can result in a substantial reduction of the field. To compensate for this effect we estimated what the field was inside the coil using the Biot-Savart Law. The magnetic field at a point due to a differential current element $Idl$ is given by:

$$dB = \frac{\mu_0 I}{4\pi} \frac{dl \times \boldsymbol{r}}{|\boldsymbol{r}|^3} \tag{12}$$

where $I$ is the current, $dl$ the differential length element, and $\boldsymbol{r}$ the vector from the current element to the point where the field is being measured. For a rectangular coil we can consider four element segments (-a/2, y), (a/2, y), (x, -b/2), and (x, b/2) which will have pairwise symmetry. To a point $(0,0,z)$ on the $z$-axis the position vector is given by $\boldsymbol{r} = (-x_{\text{seg}}, -y_{\text{seg}}, z)$ and the segment differential is $dl = (\pm dx, \pm dy, 0)$. For segments parallel to the $x$-axis (at $y = \pm b/2$) the magnetic field along

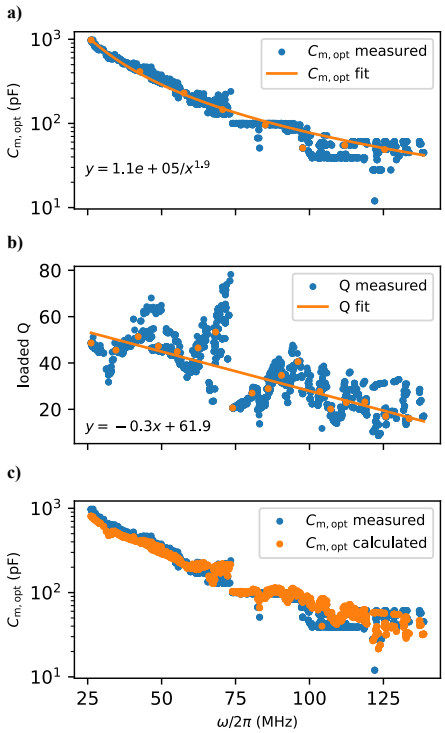


FIG. 4. Obtaining the matching capacitance $C_{m,opt}$ by either performing a fit on sampled $C_{m,opt}$ points (a) or through measured Q-values (b). Once Q-values have been measured in the frequency range of interest the matching capacitance can be calculated analytically (c).

the $z$-axis can be estimated as:

$$B_{z,x} = \frac{\mu_0 I b}{8\pi} \int_{-a/2}^{a/2} \frac{dx}{(x^2 + (b/2)^2 + z^2)^{3/2}} \tag{13}$$

and segments parallel to the $y$-axis (at $x = \pm a/2$) is then:

$$B_{z,y} = \frac{\mu_0 I a}{8\pi} \int_{-b/2}^{b/2} \frac{dy}{(y^2 + (a/2)^2 + z^2)^{3/2}} \tag{14}$$

Solving the integral and summing the contributions from all the segments we obtain:

$$B_z = \frac{\mu_0 I a b}{4\pi} \left( \frac{1}{A\sqrt{(b/2)^2 + A}} + \frac{1}{B\sqrt{(a/2)^2 + B}} \right) \tag{15}$$

where substitutions have been made for $A = (a/2)^2 + z^2$ and $B = (b/2)^2 + z^2$.

Considering a coil with $N$ turns, the loops will be located at different observation points $z - z_i$ so that the field becomes

$$B_z = \frac{\mu_0 I a b}{4\pi} \sum_{i=1}^{N} \left( \frac{1}{A\sqrt{(b/2)^2 + A}} + \frac{1}{B\sqrt{(a/2)^2 + B}} \right) \tag{16}$$

with $A = (a/2)^2 + (z - z_i)^2$ and $B = (b/2)^2 + (z - z_i)^2$.

# Paper IV

M. Lindén, D. Gustavsson, A. Walther, A. Kinos and L. Rippe
"Resetting spectral hole features in Eu:YSO using a highly tunable radio-frequency resonance circuit", *Manuscript in preparation* (2024)

# Resetting spectral hole features in Eu:YSO using a highly tunable radio-frequency resonance circuit

M. Lindén,[1,2] D. Gustavsson,[1] A. Walther,[1] A. Kinos,[1] and L. Rippe[1,a)]
[1)]*Department of Physics, Lund University, Lund, Sweden*
[2)]*Measurement Science and Technology, RISE Research Institutes of Sweden, Borås, Sweden*

(Dated: 31 July 2024)

We present a method for resetting spectral holes in europium doped crystals, which are known to have extremely long-lived hyperfine ground states at cryogenic temperatures. The holes are erased through magnetic coupling to radio frequency fields scanned across resonance of the hyperfine splitting of the levels. Using RF-pulses calibrated to a pulse area of $\pi/2$-pulses, efficient mixing between the levels was performed. The hole erasure efficency was $> 95\,\%$ using a RF input energy of approximately 0.47 J per pulse sequence sent. To set the frequency scan range of the pulses, the spin broadening was measured for each transition. The narrowest line width observed was 0.29 MHz for isotope 151 at nuclear moment transition $|\pm 1/2\rangle_g \leftrightarrow |\pm 3/2\rangle_g$ and the widest 1.4 MHz for isotope 153 at $|\pm 3/2\rangle_g \leftrightarrow |\pm 5/2\rangle_g$.

## I. INTRODUCTION

Rare earth (RE) doped materials with their unique electronic configurations and optical properties have garnered significant interest and attention in various fields including quantum information[1–4], medical imaging[5,6], and metrology[7]. Of particular interest is the Europium-doped $Y_2SiO_5$ (YSO) system which has been shown to have very slow longitudinal ($T_1$) and transverse ($T_2$) relaxation rates in the hyperfine ground states, which allows for prolonged storage of quantum information. The longitudinal rate can reach 49 days[8] with the transverse rate surpassing six hours through the use of external magnetic fields[9]. The long lifetimes have been utilized to develop quantum memories using atomic frequency combs with storage times up to 20 ms using dynamical decoupling sequences to compensate for spin dephasing[10], and on demand single photon delivery[11] for quantum repeater applications.

Europium ions have one of the narrowest homogeneous line widths reported in a solid, close to the fluorescence lifetime limit[12]. However, When located inside a crystal host, the RE ions become inhomogeneously broadened. This enables frequency frequency selectivity of the ions, which is exploited in hole-burning techniques by optically pumping ions to other ground state hyperfine levels to effectively create transparent windows[13]. As ions stored in the hyperfine levels are long-lived this results in sharp and persistent transmission windows.

Any application that requires a reset of the hyperfine population after spectral manipulation of the absorption profile where the ground states are long-lived (as is the case for slow light laser stabilization[14,15]) need an efficient method of erasing the states created, if the processes involved can not be reversed. To erase said structures one can imagine a few different approaches, including temperature cycling of the cryostat, using optical transitions, and RF-fields resonant with the hyperfine splittings. Temperature cycling the cryostat to erase spectral features (by reducing the hyperfine lifetime) is a cumbersome and lengthy process. Instead, scanning radio-frequency (RF) fields across the resonance lines of the hyperfine splittings any state created can be erased by resetting the population to its natural distribution (initial state). The use of RF fields, in contrast to optical erasure, can be done very efficiently due to the low photon energy required.

However, running RF fields where the splittings are large and occur in a wide frequency range becomes a technical challenge at cryogenic temperatures due to the tuning capability and circuit efficiency required. The is also evident in the case of $^{151/153}$Eu : YSO where the largest splitting is close to 119 MHz and four different splittings are present (for isotopes 151/153) in a wide frequency range of 34–119 MHz. Due to spin broadening of the transitions, the RF-field has to be scanned with a width wider than the spin broadening to target a majority of the ions. In addition, efficient erasure requires (as will be shown) the use of RF-pulses with a pulse area close to $\pi/2$. To avoid cryostat heating, the input power to the circuit is limited, making it difficult to produce such pulse areas.

Linearly frequency chirped pulses has been suggested[16] for a system under power-limited circumstances where it is not possible to provide enough power in a brief pulse to pump a significant fraction of a medium from the ground state to the excited state over a wide bandwidth. Harris[17] et al demonstrated such chirped excitation of optically dense inhomogeneously broadened media in Eu3:Y2SiO5 to produce equal superposition of the ground and excited states so that the resulting half-inversion pulses (analogous to a pulse area of $\pi/2$) could be produced over a large bandwidth.

In this work we present a method of erasing long lived states by applying RF fields resonant with the hyperfine transitions in Eu:YSO using a highly tunable circuit. The RLC resonance circuit, which is described in more detail in Lindén et. al[18], employs micro-mechanical switches to create a capacitance bank used for wide and semi-continuous tuning. Using RF magnetic fields scanned across the hyperfine splittings half-inversion states can be created. In order to set an appropriate scan range for each transition the spin broadening was measured for both isotopes and all hyperfine transitions at 1 at%

a)Author to whom correspondence should be addressed.
e-mail: lars.rippe@fysik.lth.se

doping concentration.

In principle, no heating losses should result from RF erasure as the ion distribution is mainly symmetric between the hyperfine levels. Thus, it is as likely for the ions to be absorbed as it is to undergo stimulated emission, making the medium transparent for the fields involved. There will still be joule heating due to imperfections in the RF-resonator, although this is a technical limitation rather than a fundamental one. We show that efficient erasure can be performed using $\pi/2$-calibrated pulse sequences with an input energy of 0.47 J.

## II. RF PULSE DESIGN

When a ground state has been optically pumped at some frequency $\nu$ to create a transmission window, ions are emptied from all the hyperfine levels. Consequently, to reset the state after pumping it is necessary to run RF pulses at all the hyperfine transitions.

In order to perform efficient mixing of ion populations, population swapping can be performed between the ground states. Assuming the energy splitting between the states is small, the Boltzmann distribution implies that the population distribution of ions in each level can be assumed to be approximately equal. In the case of a three level system, each level will have a population close to $1/3$. If the population is shifted through optical pumping, it is possible to reset it rapidly by applying $\pi/2$-pulses to the system, shuffling populations between levels.

The pulse sequence to erase the optical stuctures consists of four RF-pulses where each pulse targets one hyperfine transition sequentially, including ground states $|\pm 1/2g\rangle \leftrightarrow |\pm 3/2g\rangle$ and $|\pm 3/2g\rangle \leftrightarrow |\pm 5/2g\rangle$ for both isotopes. The suggested pulse scheme is shown in Fig 1. After optically pumping ions a transmission window is created, with a shifted ground state population. Applying RF $\pi/2$-pulses between all the hyperfine transitions, the population at the poles for any given transition is brought to the equator in the Bloch-sphere. Ions are left at the equator and set to decohere before the next pulse targeting the same hyperfine level starts. If the pulse is not a exactly a $\pi/2$-pulse, ions will be moved partly towards the equator where they can be projected on the z-axis after the decoherence time $t_c$ has passed. The length of the Bloch vector is then shorter than unity, pointing towards one of the poles. Due to the long relaxation time, the probability amplitudes will not change during the time between pulses $T$. The next set of pulses targeting the same transition shortens the Bloch vector until a fully mixed state is reached.

In the simple case where decay effects are ignored and half-inversion pulses are assumed to be perfect, resetting a three level system takes at most five sequences to set the natural population distribution within 0.5 % given some arbitrary initial state. Such a case has been simulated in Fig. 1 where the natural distribution is shifted through the process of optical pumping, resulting in a transmission window. To reset the state, five pulse sequences is sent to target all the ions in the inhomogeneous profile.

To ensure efficient population transfer with RF pulses it is necessary to know the line-width $\Gamma_s$ of the transition. No measured values have been reported yet for the spin broadening in $^{151}$Eu and $^{153}$Eu at a doping concentration of 1 % so to measure the broadening a narrow line-width ($\sim$ 10 Hz) dye-laser was used to perform optical pumping and peak burn-back of ions from a specific hyperfine transition in to the prepared transmission window. (see section III for a more detailed description). Once $\Gamma_s$ had been determined for each of the hyperfine transitions this was used to set the RF scan range $\Gamma_{RF}$ to approximately $3 \times \Gamma_s$. Assuming a Gaussian distribution for the spin broadening, three times the FWHM should encompass more than 99.5 % of the ions. As is shown in the next section, this assumption can be considered reasonable.

The RF pulses were designed through considerations of the pulse area required to make a $\pi/2$-pulse. To perform coherent half-inversion transfers it is possible to use chirped pulses.[17] A linear relationship exists between the applied chirp-pulse intensity and chirp rate. For a two level system the fundamental scaling parameter for chirped excitation is given as

$$\Phi = \frac{\Omega_0}{(\Gamma_{\mathrm{RF}}/\tau_{RF})} \tag{1}$$

where $\Omega_0 = \mu B_0/\hbar$ is the generalized Rabi frequency of the chirped pulse, $\Gamma_{RF}$ the frequency scan range, and $\tau_{RF}$ the chirp duration. The experimental chirp rate, $\Gamma_{RF}/\tau_{RF}$, is in units of $s^{-2}$ so that $\Phi^2$ becomes proportional to the ratio between applied chirp pulse intensity and chirp rate.

For large time–bandwidth of the chirp the Bloch vector representation for media inversion can be written[17]

$$r_3(\Phi) = 1 - 2\exp(\pi\Phi)^2 \tag{2}$$

and if solved for $\Phi$ we obtain the following:

$$\Phi(r_3) = \frac{1}{\pi}\sqrt{\ln\left(\frac{2}{1-r_3}\right)} \tag{3}$$

In this work we are interested in the linear chirp rate and magnetic field required to produce an average Bloch-vector rotation of $\pi/2$ (half-inversion with $r_3 = 0$). The final state will therefore be a superposition state of the ions in the crystal which, on average, will have an equal mixture of the ground and excited state. From eq. 3, half-inversion results in $\Phi(0) = 0.265$.

To discriminate half inversion states from other states, the RF pulses were first calibrated using an approach described in section III B. For a given input power to the magnetic field generating resonance circuit, the RF-pulses could be calibrated for half-inversion by adjusting the frequency scan range $\Gamma_{RF}$ and pulse duration $\tau_{RF}$.

In the following sections we will describe the spin broadening measurements results and erasure performance in more detail.

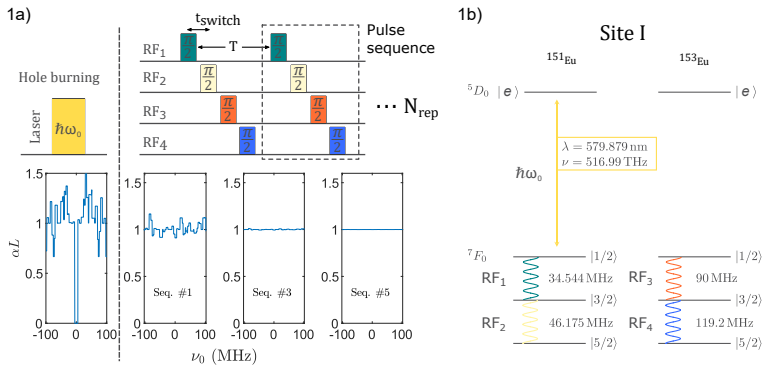


FIG. 1. The pulse scheme used for erasure. After creating a transmission window, a set of pulses targeting the four different hyperfine transitions in Eu:YSO will redistribute ions to the natural Boltzmann distribution if enough repetitions are made. Time between pulses targeting the same transition is $T$ and time to tune the resonance to a new transition is given by $t_{switch}$

## III. RESULTS

### A. Spin broadening

To measure the spin broadening a narrow line-width laser was used to burn a 5 MHz wide pit followed by subsequent sech-scan peak burn-backs at a frequency $\Delta f_{\mathrm{tw}}$ (relative to the pit center frequency) with a scanning width of $\Gamma_{\mathrm{peak}}$. Ions offset in frequency by the hyperfine splitting relative to the center frequency of the pit can be targeted optically and moved inside the pit. For instance, to observe broadening for the transition $^{151}\mathrm{Eu}_{|\pm1/2\rangle\leftrightarrow|\pm3/2\rangle}$ ions were optically excited at the burn-back frequency $\Delta f_{\mathrm{tw}} = 34.544\,\mathrm{MHz}$ using a scan width of $\Gamma_{\mathrm{peak}} = 50\,\mathrm{kHz}$. The level splitting for the hyperfine transitions have been measured by .. and was used here for the peak burn-back frequencies.

If the excited region of ions to the excited state is narrow so that the optical pulse $\Gamma_{\mathrm{peak}}$ is small compared to $\Gamma_{\mathrm{s}}$, then ions that are relaxed from $^5D_0$ distribute according to the broadening of the transition. Due to the transition probability being symmetric, i.e. $p(g_1 \rightarrow g_2) = p(g_2 \rightarrow g_1)$, burning back peaks at $\pm\Delta f_{\mathrm{tw}}$ will result in peaks with equal broadening.

In Fig. 2 the spin broadened peaks for the four transitions $^{151}\mathrm{Eu}_{|\pm1/2g\rangle\leftrightarrow|\pm3/2g\rangle}$, $^{151}\mathrm{Eu}_{|\pm3/2g\rangle\leftrightarrow|\pm5/2g\rangle}$, $^{153}\mathrm{Eu}_{|\pm1/2g\rangle\leftrightarrow|\pm3/2g\rangle}$, and $^{153}\mathrm{Eu}_{|\pm3/2g\rangle\leftrightarrow|\pm5/2g\rangle}$ are shown. The peak center frequencies had an offset of $\Delta f_{\mathrm{tw,dev}}$ compared to values referenced in literature, where the largest deviations was measured for the 153 isotope. A voigt fit was performed of the peaks to calculate the FWHM ($\Gamma_s$) and determine if the distribution was Gaussian or Lorrentzian. All peaks followed a Gaussian distribution for the optical depth $\alpha L$ given by $\alpha L = \ln(I/I_0)$, with $I$ as the transmitted intensity and $I_0$ as the reference intensity. The absorption peaks were adjusted to account for any residual absorption in the pit by subtracting the pit absorption spectra from the peak measurements.

All transition broadenings and optical burn-back parameters used to create the absorption peaks have been listed in Table I. The largest spin broadening $\Gamma_{\mathrm{s}}$ was observed for the $^{153}\mathrm{Eu}_{|\pm3/2g\rangle\leftrightarrow|\pm5/2g\rangle}$ transition, having a broadening of 1.4 MHz. This transition may be even broader however as indicated by the background absorption being high at the tails of the Gaussian. To increase the signal a wider scan ($\Gamma_{\mathrm{peak}} = 0.2\,\mathrm{MHz}$) was used for the peak burn-back.

In general, the transition got broader the larger the splitting between the levels were. This is likely an broadening effect stemming from an increased ion-ion/ion-lattice interaction. Once $\Gamma_{\mathrm{s}}$ had been obtained, RF pulses were calibrated to make approximate $\pi/2$ rotations using square pulse frequency scans for the transitions where this was possible.

### B. Pulse calibration

The pulse area of an RF-pulse can be distinguished from its absorption footprint. Depending on the pulse area the population transfer will be different, and this can be used to create a contrast in the absorption profile if the starting state is set appropriately. To create this initial state a 5 MHz transparent window was created. Absorption peaks could then be burnt back in to the window, using the same methodology as described in section III A. The peak width $\Gamma_{\mathrm{peak}}$ was set to 1 MHz in order to increase absorption and make the peak easier to identify. Important to note is that the peak width can be set to some arbitrary width as long as it fits inside the pit. The reason is that all ions across the optical inhomogeneity

TABLE I. Experimental optical parameters used to measure spin broadening $\Gamma_s$ and the calibrated RF-pulse settings. Peak burn-backs to the transmission window center frequency were performed by scanning a width $\Gamma_{peak}$ at an offset frequency of $\Delta f_{tw}$ corresponding to the hyperfine level splitting of the transition. The RF scan width $\Gamma_{RF}$ was set to be approximately $3 \times \Gamma_s$ while $\tau_{RF}$ was varied to obtain a $\pi/2$-pulse given an input power $P_{in}$ and magnetic field $B_0$. The scan rate $\Gamma_{RF}/\tau_{RF}$ resulted in a Rabi frequency $\Omega_0$ and measured magnetic dipole moment of $\mu$.

| | Optical | | | RF | | | | | | |
|---|---|---|---|---|---|---|---|---|---|---|
| Transition | $\Gamma_{peak}$ (MHz) | $\Delta f_{tw}$ (MHz) | $\Delta f_{tw,dev}$ (MHz) | $\Gamma_s$ (MHz) | $\Gamma_{RF}$ (MHz) | $\tau_{RF}$ | $\Omega_0$ (krad s$^{-1}$) | $P_{in}$ (mW) | $B_0$ (μT) | $\mu$ (J T$^{-1}$) |
| $^{151}Eu_{\|\pm1/2g\rangle\leftrightarrow\|\pm3/2g\rangle}$ | 0.05 | 34.544 | 0.01 | 0.29 | 0.81 | 1 | 214.7 | 57.6 | 6.7 | $3.4 \times 10^{-24}$ |
| $^{151}Eu_{\|\pm3/2g\rangle\leftrightarrow\|\pm5/2g\rangle}$ | 0.05 | 46.175 | 0.02 | 0.30 | 1.06 | 3 | 93.6 | 57.6 | 6.0 | $1.64 \times 10^{-24}$ |
| $^{153}Eu_{\|\pm1/2g\rangle\leftrightarrow\|\pm3/2g\rangle}$ | 0.05 | 90 | 0.21 | 0.55 | 1.59 | 15 | 28.1 | 50.5 | 3.4 | $8.7 \times 10^{-25}$ |
| $^{153}Eu_{\|\pm3/2g\rangle\leftrightarrow\|\pm5/2g\rangle}$ | 0.2 | 119.2 | 0.10 | 1.4 | 4.5 | 30 | - | 30.1 | 1.9 | - |

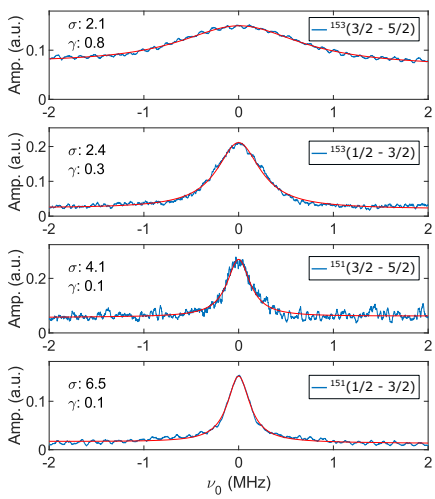


FIG. 2. Spin broadenings $\Gamma_s$ measured for hyperfine transitions in Eu:YSO. The peaks were moved in to a 5 MHz pit by burning at the frequencies $\Delta f_{tw}$, corresponding to the hyperfine splittings. A moving mean smoothing was applied before fitting a Voigt function to the peaks.

are affected equally by the RF-field, assuming the RF-pulse scan width across the transition is wide enough to target all the spin broadened ions.

By burning back a peak of ions optically at a frequency $\Delta f_{tw}$ in to the transmission window (centered at $f_{tw}$) this has the effect of filtering out other ion classes so that there is only one ion class absorbing. The peak burn-back also results in a new transmission window (with width $\Gamma_{peak}$) at $\Delta f_{tw}$.

Ignoring effects from ions outside the window, a RF $\pi$-rotation having its center frequency at $\Delta f_{tw}$ would effectively move the ions out of the transmission window back to the original frequency before being affected by the peak burn-back. For a pulse area below $\pi$, only a portion of ions will be moved, resulting in a peak with lower amplitude.

Due to the RF-pulse targeting all ions and not just those inside the transmission window, the net effect of a magnetic field $\pi$-pulse centered at $\Delta f_{tw}$ is that ions originating outside the window will partly fill the window. A second effect is that a silhouette is formed from the ion peak that is moved out of the window. This silhouette effect is due to there being no ions left at the location of the second transmission window (due to peak burn-back) that can be moved in to the first.

Four different pulse areas have been simulated in Fig. 3 b) for the transition $^{151}Eu_{|\pm1/2g\rangle\leftrightarrow|\pm3/2g\rangle}$, demonstrating the absorption profiles. The cases were simulated using a burn-back frequency $\Delta f_{tw} = 34.544$ MHz with an RF-pulse pulse area ranging from $\{0, \pi\}$ in steps of $\pi/4$. Evidently, this pattern can be used to distinguish what pulse area a RF-pulse has. For an exact $\pi/2$-pulse, it is expected that the background absorption contribution from ions entering the pit can not be discriminated from ions originating in the pit as they both approach the equator on the Bloch sphere. This results in a flat line across the pit.

Fig. 3 a) shows the experimental data for the transition $^{151}Eu_{|\pm1/2g\rangle\leftrightarrow|\pm3/2g\rangle}$ where the pulse area was varied through different pulse lengths $\tau_{RF}$, with the circuit input power (magnetic field amplitude $B_0$) and scan range $\Gamma_{RF}$ fixed. Between each shot the window was emptied and a new peak was burnt back. For a RF-pulse with 2.5 s duration the peak is clearly inverted, creating a silhouette of the originating peak indicating a pulse area close to $\pi$. On the contrary, a pulse with 0.5 s results in a pulse area which appears to be below $\pi/2$. For a 1 s pulse the pulse area is close to the desired area of $\pi/2$, with it possibly overshooting slightly. For the purpose of erasure a $\pi/2$-pulse will result in faster erasure but it is not crucial that an exact pulse area is achieved, as is discussed in section III C. All RF-pulse parameters used to perform $\pi/2$ rotations for the different transitions have been summarized in Table I.

### C. Erasure of spectral structures

To test erasure performance of the $\pi/2$-calibrated RF-pulses (with $\Gamma_{RF} \approx 3\Gamma_s$) a spectral transmission window with a width of 50 kHz was burnt. Erasure efficency of individ-

ual transitions was performed at first to see the gradual response after each RF-pulse. Then pulses were combined in to a pulse sequence targeting all transitions sequentially. The performance metric for erasure was $\alpha_e/\alpha_0$ where $\alpha_e$ was the mean absorption level inside the transmission window, and $\alpha_0$ the absorption outside it. The window was prepared in a lower absorption area so that the transmission contrast at $\alpha_0$ was approximately 10 % of the transmission window before erasure. This allowed for more accurate absorption measurements outside the pit due to there being less detector noise. All measurements were performed at the same transmission window center frequency, by emptying ions out of the window before targeting a different transition with RF.

For a given transition, five pulses were sent one at a time with a transmission measurement in between. The results are presented in Fig. 3 c). By applying several pulses the erasure level should approach some value where the two states have been appropriately mixed, which was around 58–59 %. The number of pulses required for convergence will depend on how closely the pulse area has been calibrated towards being a $\pi/2$-pulse.

From the results it can be seen that most transitions are mixed after just one to two pulses except for the $^{153}$Eu$|\pm 3/2g\rangle \leftrightarrow |\pm 5/2g\rangle$ transition which did not converge within five pulses. This was expected because it was not possible to obtain a pulse area close to $\pi/2$ in this case as the pulse duration was restricted to 30 s in combination with a lower input power of $P_{in} = 30.1$ mW to avoid excessive Joule heating of the cryostat from the resonance circuit. The linear scaling parameter $\Phi(r_3)$ was not known in this case and consequently $\Omega_0$, $B_0$, and $\mu$ could not be determined for this transition.

Transitions with larger splittings ($\Delta f_{tw}$) had a lower Rabi frequency $\Omega_0$ as longer pulses were required for half-inversion. This may have been due to lower magnetic field and magnetic dipole moment measured.

The combined pulse sequence (green trace) showed an erasure level of $> 95$ % after one pulse sequence increasing slightly for each sequence count, likely due to the $^{153}$Eu$|\pm 3/2g\rangle \leftrightarrow |\pm 5/2g\rangle$ level becoming more mixed. The energy required for one pulse sequence was 0.47 J. This energy should be resistive losses from imperfections in the circuit as a majority of the ions will be unaffected by the magnetic field.

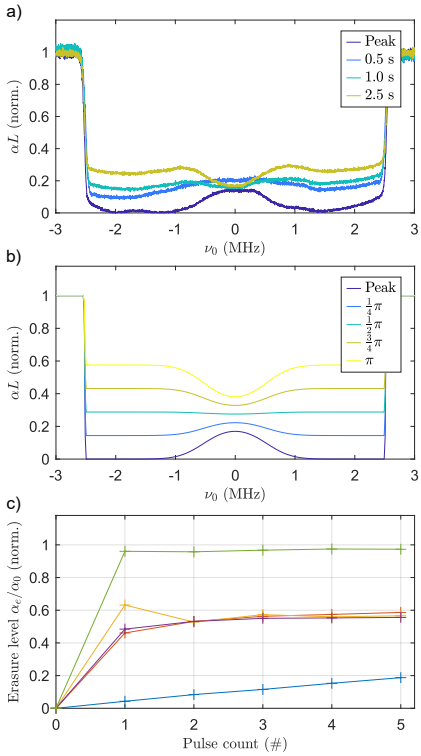


FIG. 3. RF Pulse calibration measurements for transition $^{151}$Eu $|\pm 1/2g\rangle \leftrightarrow |\pm 3/2g\rangle$ with measured absorption footprint in a) for different pulse durations $\tau_{RF}$, which was linked to a simulated pulse area in b). A superposition state (pulse area equal to $\pi/2$) is achieved if the absorption level is flat across the transmission window, as shown in the simulated case. In c), the erasure efficiency for each transition is shown where $\alpha_e$ is the mean absorption inside the transmission window and $\alpha_0$ is the absorption outside it. For each calibrated RF pulse the erasure level converges towards an erasure level close to 58–59 %. Most transitions (with the exception for $^{153}$Eu $|\pm 3/2g\rangle \leftrightarrow |\pm 5/2g\rangle$) are close to fully mixed within 1–2 pulses, indicating the pulse area is close to $\pi/2$. The green trace shows the combined pulse sequence including all pulses with an erasure level above 95 % after a single sequence.

## IV. CONCLUSIONS

In this work we have shown a method to erase long lived states to reset the spectral structure in Eu:YSO using RF half-inversion pulses. The RF pulse parameters were optimized by measuring the hyperfine spin broadening of the transitions, determining how wide the scan had to be. Once $\Gamma_{RF}$ was set, the pulses were calibrated to have a pulse area of $\pi/2$. To measure the pulse area absorption peaks with ions corresponding to a hyperfine splitting frequency offset were moved inside a transmission window. By sending RF pulses with different pulse durations and measuring the absorption footprint it was possible to distinguish what pulse area the pulse had. Finally, the calibrated pulses were used to perform erasure where a majority of the window could be erased within one pulse sequence. The broadest transition, $^{153}$Eu$_{|\pm 3/2g\rangle \leftrightarrow |\pm 5/2g\rangle}$, was identified as a potential culprit as the transition increases the time required to perform full erasure.

[1] N. Ohlsson, R. Krishna Mohan, and S. Kröll, "Quantum computer hardware based on rare-earth-ion-doped inorganic crystals," Optics Communi-

cations **201**, 71–77 (2002).
[2] J. H. Wesenberg, K. Mølmer, L. Rippe, and S. Kröll, "Scalable designs for quantum computing with rare-earth-ion-doped crystals," Physical Review A - Atomic, Molecular, and Optical Physics **75**, 1–7 (2007).
[3] A. Walther, B. Julsgaard, L. Rippe, Y. Ying, S. Kröll, R. Fisher, and S. Glaser, "Extracting high fidelity quantum computer hardware from random systems," Physica Scripta T **T137** (2009), 10.1088/0031-8949/2009/T137/014009, arXiv:1001.1664.
[4] A. Kinos, D. Hunger, R. Kolesov, K. Mølmer, H. de Riedmatten, P. Goldner, A. Tallaire, L. Morvan, P. Berger, S. Welinski, K. Karrai, L. Rippe, S. Kröll, and A. Walther, "Roadmap for Rare-earth Quantum Computing," , 1–47 (2021), arXiv:2103.15743.
[5] A. Walther, L. Rippe, L. V. Wang, S. Andersson-Engels, and S. Kröll, "Analysis of the potential for non-invasive imaging of oxygenation at heart depth, using ultrasound optical tomography (UOT) or photo-acoustic tomography (PAT)," Biomedical Optics Express **8**, 4523 (2017).
[6] A. Bengtsson, D. Hill, K. Shortiss, L. Rippe, and S. Kröll, "Comparison of contrast-to-noise ratios of different detection methods in ultrasound optical tomography," Biomedical Optics Express **13**, 4834 (2022).
[7] S. P. Horvath, C. Shi, D. Gustavsson, A. Walther, A. Kinos, S. Kröll, and L. Rippe, "Slow light frequency reference cavities - proof of concept for reducing the frequency sensitivity due to length fluctuations," New Journal of Physics **24** (2022), 10.1088/1367-2630/ac5932, arXiv:2104.03880.
[8] R. Oswald, M. G. Hansen, E. Wiens, A. Y. Nevsky, and S. Schiller, "Characteristics of long-lived persistent spectral holes in Eu3+: Y2SiO5 at 1.2 K," Physical Review A **98**, 1–8 (2018), arXiv:1811.08346.
[9] M. Zhong, M. P. Hedges, R. L. Ahlefeldt, J. G. Bartholomew, S. E. Beavan, S. M. Wittig, J. J. Longdell, and M. J. Sellars, "Optically addressable nuclear spins in a solid with a six-hour coherence time," Nature **517**, 177–180 (2015).
[10] A. Ortu, A. Holzäpfel, J. Etesse, and M. Afzelius, "Storage of photonic time-bin qubits for up to 20 ms in a rare-earth doped crystal," npj Quantum Information **8**, 1–7 (2022), arXiv:2109.06669.
[11] A. Seri, A. Lenhard, D. Rieländer, M. Gündogan, P. M. Ledingham, M. Mazzera, and H. de Riedmatten, "Quantum correlations between single telecom photons and a multimode on-demand solid-state quantum memory," Physical Review X **7**, 1–7 (2017), arXiv:1701.09004.
[12] F. Könz, Y. Sun, W. Thiel, L. Cone, W. Equall, L. Hutcheson, and M. Macfarlane, "Temperature and concentration dependence of optical dephasing, spectral-hole lifetime, and anisotropic absorption in Eu3+:Y2SiO5," Physical Review B - Condensed Matter and Materials Physics **68**, 1–9 (2003).
[13] G. J. Pryde, M. J. Sellars, and N. B. Manson, "Solid state coherent transient measurements using hard optical pulses," Physical Review Letters **84**, 1152–1155 (2000).
[14] S. P. Horvath, C. Shi, D. Gustavsson, A. Walther, A. Kinos, S. Kröll, and L. Rippe, "Slow light frequency reference cavities—proof of concept for reducing the frequency sensitivity due to length fluctuations," New Journal of Physics **24**, 033034 (2022), arXiv:2104.03880.
[15] D. Gustavsson, M. Lindén, A. Walther, A. Kinos, S. Kröll, and L. Rippe, *Laser frequency stabilization using the slow light effect in Eu:YSO* (Manuscript in preparation).
[16] J. R. Klauder, A. Price, S. Darlington, and W. J. Albersheim, "The theory and design of chirp radars," Bell System Technical Journal **39**, 745–808 (1960).
[17] T. L. Harris, G. W. Burr, J. A. Hoffnagle, M. Tian, W. R. Babbitt, and C. M. Jefferson, "Chirped excitation of optically-dense inhomogeneously broadened media using Eu3+:Y2SiO5," OSA Trends in Optics and Photonics Series **88**, 1531–1532 (2003).
[18] M. Lindén, D. Gustavsson, A. Walther, A. Kinos, S. Kröll, and L. Rippe, *Highly tuneable in-situ cryogenic switch bank resonator for magnetic field generation at radio-frequencies* (Manuscript in preparation).

## V. SUPPLEMENTARY

### A. Methods

These experiments were carried out in an europium doped $Y_2SiO_5$ crystal that was placed inside a cryostat (Optidry250, MyCryofirm) and cooled to 1.5 K. It was doped with 1 at% Eu in natural abundance, which contains isotopes $^{151}$Eu and $^{153}$Eu in approximately equal proportion.

The ground and excited state are both split in to three hyperfine levels, with no external magnetic field applied. The optical resonance frequency is shifted (inhomogeneously broadened), which in turn results in that nine different ion groups (three per ground state) per isotope will be optically resonant at the same time for any given frequency. Optical pumping thus cause ions to be emptied from all hyperfine levels. The consequence of this is that all hyperfine transitions have to be targeted by RF-pulses to effectivley reset the state.

With RF-pulses calibrated to have an approximate pulse area of $\pi/2$, the erasure efficiency was measured for each separate transition (see section III C) as well as for the full sequence. The RF scans were generated using a 60 MHz signal generator (125-14, Red Pitaya), frequency doubled using a and routed to a highly tunable RF resonance circuit, described in more detail elsewhere[18]. The coil had $N = 5$ turns, a rectangular area of $A = 16 \times 17\,\mathrm{mm}^2$ and length $L = 20\,\mathrm{mm}$. Pulse parameters for the different transitions have been listed in Table I.

Optical pumping and peak burn-backs (see III for details) was performed using a diffuse side burner mounted on the side of the crystal, described in Gustavsson et. al[15]. All experiments were performed at site 1 which has its absorption peak at a vacuum wavelength of $\lambda_0 = 579.879\,\mathrm{nm}$. Frequency offsets to this wavelength have been denoted $\nu$ where $\nu = c/\lambda_0 + f_{\mathrm{AOM}}$. In most cases we are only interested in frequency offsets $\Delta f_{\mathrm{tw}}$ relative to the transmission window center frequency $f_{\mathrm{tw}}$ so that $f_{\mathrm{AOM}} = f_{\mathrm{tw}} + \Delta f_{\mathrm{tw}}$.

Transmission measurements were done using a 1 mm diameter beam directed to a half-wave plate, polarizer, and lastly the crystal with the beam parallel to the $D_1$ axis. The measurements used a low noise amplifier (SA-602, NF) for detection in transmission and a reference detector (DLPCA-200, Femto) placed before the half-wave plate.

# Paper V

A. J. Renders, D. Gustavsson, M. Lindén, A. Walther, S. Kröll, A. Kinos and L. Rippe
"Pushing the limits of negative group velocity", *Manuscript submitted for publication* (2024)

# Pushing the limits of negative group velocity

A. J. Renders, D. Gustavsson, M. Lindén, A. Walther, S. Kröll, A. Kinos, and L. Rippe
*Department of Atomic Physics, Lund University.*

(Dated: June 26, 2024)

Distortion free negative group velocity pulse propagation is demonstrated in a rare-earth-ion-doped-crystal (RE) through the creation of a carefully designed spectral absorption structure in the inhomogeneous profile of Eu:YSO and subsequently inverting it. The properties of the RE system make it particularly well suited for this since it supports the creation of very sharp, arbitrarily tailored spectral features, which can be coherently inverted by a single pulse thanks to the long coherence time of the transition. All together these properties allow for a large time advancement of pulses without causing distortion. A pulse advancement of 13% with respect to the pulse full-width-half-maximum was achieved corresponding to a time-bandwidth product of 0.06. This to our knowledge is the largest time-bandwidth product achieved, with negligible shape distortion and attenuation. Our results show that the rare-earth platform is a powerful test bed for superluminal propagation in particular and for dispersion profile programming in general.

Manipulation of the group velocity, $v_g$, of pulses has been a subject of study for several decades. This manipulation is done by controlling the dispersion of the medium in which the pulse propagates. Controlling dispersion is vital in various applications, e.g. chirped pulse amplification [1] and in optical fibres [2]. Reducing $v_g$ has led to an interesting field of research with a number of applications such as laser stabilisation [3, 4] and medical imaging [5]. When working at the other end of the spectrum of $v_g$, in particular increasing $v_g$ beyond the vacuum light speed $c$, or when $v_g$ becomes negative, things become more abstract and less intuitive. One cannot violate causality, but negative group velocities can be achieved and can be described by the Kramers-Kronig relations [6]. A number of experiments, starting as early as the 1960s, have been conducted to show that one can go into a regime where $v_g > c$ and can even go negative i.e. the pulse peak exits the material earlier than it entered [7–13]. The methods used include using the dispersion in an absorbing medium near a transparency [12] and non-linear amplification [7]. However, all these early experiments showed either a great deal of distortion of the pulses that were advanced in time [7, 8] or the pulses were heavily attenuated [9–13]. This left room for different interpretations of the result and the physical meaning of what was seen. In the strong attenuation case, for example, it was argued that the pulse was not advanced, but rather selectively attenuated such that the pulse peak appears to be shifted forward, but is still completely contained within the original pulse envelope.

To address the concerns raised regarding the physical interpretation, an undistorted, advanced pulse needed to be produced. It was suggested by Steinberg et al. [14] that one could achieve undistorted pulse propagation through a transparent optical window between two gain regions. This was subsequently shown experimentally by Wang et al. [15], using a Raman pumped system in a caesium vapour cell in $\Lambda$ configuration. However, the initial publication showed the advanced pulse still had some distortion. This among other factors made Ringenmacher and Mead [16] question the interpretation. To them, the 3% shape error with only 62 ns, 1.6%, advancement on a pulse with $t_{\mathrm{FWHM}} = 3.7$ $\mu$s, and hence a time-bandwidth product of 0.007, seemed insufficient for a proper conclusion. Later Wang et al. published a second paper where they presented a pulse with similar advancement but without the previously observed distortion [17].

In this work, we demonstrate almost an order of magnitude improvement in terms of time-bandwidth product, and relative pulse advancement. A Gaussian probe pulse with time full width half maximum (FWHM), $t_{\mathrm{FWHM}} = 4.2$ $\mu$s, was used in these experiments. This pulse was advanced by 0.543 $\mu$s which corresponds to 13% of the $t_{\mathrm{FWHM}}$, see FIG 1, left inset. The relation of the FWHM of a Gaussian pulse in time and frequency is $t_{\mathrm{FWHM}} = 0.44/\nu_{\mathrm{FWHM}}$, hence $\nu_{\mathrm{FWHM}} = 105$ kHz. This gives a time-bandwidth product, $|\Delta t| \cdot \nu_{\mathrm{FWHM}}$, of 0.06, the corresponding group refractive index $n_g$ is hence -$6.6{\cdot}10^3$. The shape was well maintained, the $t_{\mathrm{FWHM}}$ stayed within 1.6% and the pulse power within 3.0% (upper bound estimation) of a reference pulse.

We realised these results through the creation of two sharp, closely spaced gain regions in the inhomogeneous profile of a Europium-doped YSO crystal. This leads to a region of strong and linear anomalous dispersion between the gain regions, see FIG 1, right inset. The rare-earth system allows for much sharper gain features than were created in the caesium vapour cell [15], and a group refractive index that is strongly negative. We are not aware of any previous result of a pulse time advancement with this large a time-bandwidth product, with as little distortion or attenuation.

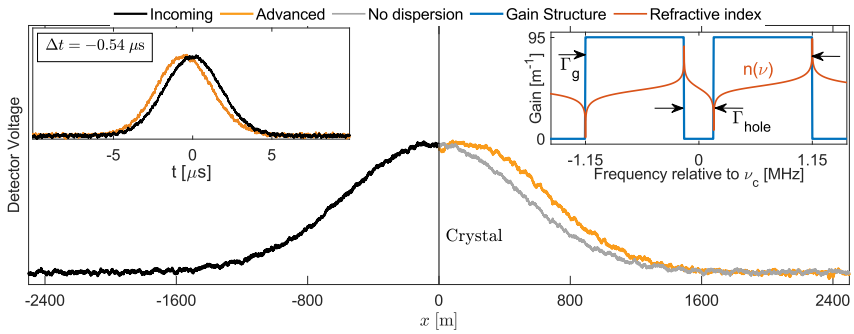


FIG. 1. The spatial propagation of the pulse as it approaches the crystal. For clarity, the incoming and no dispersion pulses are scaled to the same intensity as the probe that propagates through the crystal. Unnormalised data can be found in the supplement. The position of the crystal is indicated by the vertical line. Here it can be seen that the advanced pulse peak comes out of the material before the incoming pulse peak enters. In the left inset the pulses are shown in time, with the advancement $\Delta t$. The $t_{\mathrm{FWHM}}$ ratio between the $t_{\mathrm{FWHM}}$ for the advanced and reference pulse was 0.984. The pulse has a $t_{\mathrm{FWHM}}$ of 4.2 $\mu$s. The right inset shows the gain structure used in the experiment and its effect on the refractive index. The gain structure width, $\Gamma_g = 2.3$ MHz, and hole width, $\Gamma_{\mathrm{hole}} = 300$ kHz are indicated.

Light pulses travel at the group velocity $v_g$ [18]:

$$v_g(\nu) = \frac{c}{n(\nu) + \nu \frac{dn(\nu)}{d\nu}} \tag{1}$$

With the speed of light in vacuum $c$, the refractive index $n(\nu)$ and the optical frequency $\nu$ [19]. From this expression, one can see that the refractive index and the change of the refractive index with frequency, the dispersion, influence the group velocity. In close vicinity of resonances of an ion, i.e. close to regions with absorption or gain, very strong dispersion can be achieved, see FIG 1, right inset. This behaviour can be described using the susceptibility, the imaginary and real parts of which govern the absorption and refractive index response respectively. Using this, one can calculate the dispersion.

The real part of the susceptibility can be computed fairly simply from the ion distribution generating the gain, which has a width of $\Gamma_g$, and the hole width, $\Gamma_{\mathrm{hole}}$. The index of refraction as a function of frequency $n(\nu)$ was derived for this ion distribution. Since the region of interest is the transparent region around the centre frequency of the hole (where the fast light pulse propagates), a Taylor expansion is applied to get a linear approximation of $n(\nu)$:

$$n(\nu) = n_{\mathrm{host}} + \frac{\alpha c}{\pi^2 \nu_c} \left( \frac{1}{\Gamma_{\mathrm{hole}}} - \frac{1}{\Gamma_g} \right) (\nu - \nu_c) \tag{2}$$

With the background refractive index, $n_{\mathrm{host}}$, and the central optical frequency, $\nu_c$. Here contributions to the refractive index stemming form beyond the frequency range in the right inset in FIG (1) are ignored. It should be noted that in the case of an inverted population the absorption coefficient, $\alpha$, will change sign and become a gain coefficient. A full derivation can be found in the supplement. The group refractive index can then be found by inserting equation (2) into the equation for the group refractive index $n_g = n(\nu) + \nu \frac{dn(\nu)}{d\nu}|_{\nu=\nu_c}$ which is evaluated at the centre frequency. When the dispersion is large, $n_{\mathrm{host}}$ is negligible and the dispersion term completely dominates the denominator, hence the group velocity $v_g(\nu = \nu_c)$:

$$v_g = \frac{\pi^2}{\alpha} \left( \frac{1}{\Gamma_{\mathrm{hole}}} - \frac{1}{\Gamma_g} \right)^{-1} \tag{3}$$

The resulting time advancement compared to propagation in vacuum is:

$$\Delta t = \frac{\alpha L}{\pi^2} \left( \frac{1}{\Gamma_{\mathrm{hole}}} - \frac{1}{\Gamma_g} \right) \tag{4}$$

It is then evident that the stronger the gain and the narrower the spectral hole between the gain regions, the stronger the effect on the dispersion and thus the group velocity.

We will now briefly describe, first, how the gain structure is prepared, second, how amplified spontaneous emission in the created structures may limit the achievable dispersion and thereby also the time advancement of the pulse and, finally, aspects on pulse distortion. Additional details of these aspects are also provided in the supplementary material. The rare-earth ions are inhomogeneously broadened, such that different ions absorb

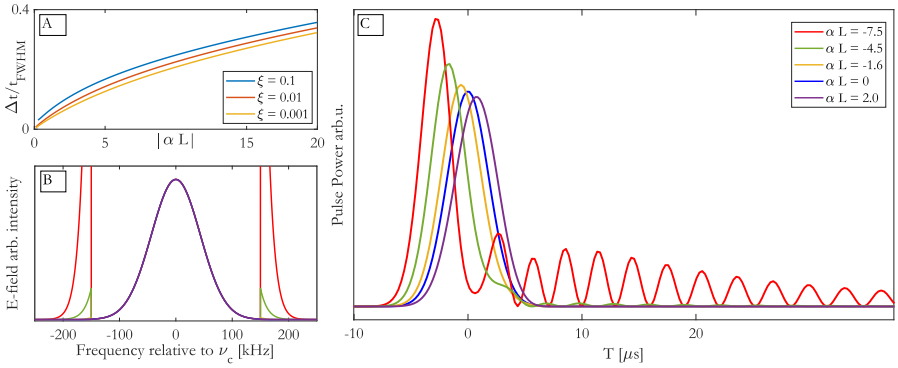


FIG. 2. (a) Relative pulse advancement as a function of $\alpha L$ at fixed $\Gamma_{\text{hole}}$ (=300 kHz) for different degrees of tolerance in the pulse power increase. (b) Increase in pulse area of the electric field caused by the gain structure for different values of $\alpha L$ corresponding to those in (c). (c) Maxwell-Lindblad simulation of the propagation pulse with $t_{\text{FWHM}} = 4.2$ $\mu$s and $\Gamma_{\text{hole}} = 300$ kHz at various $\alpha L$, which shows the distortion caused by the amplified frequency regions in (b). The experimental conditions in FIG 1 correspond to $\alpha L = -1.6$

at different frequencies. Further, the ions have three different and very long-lived (hours/days) doubly degenerate ground hyperfine levels at zero magnetic field. Thus, it is possible to use optical pumping to spectrally tailor the absorption profile until the structure seen in the right inset of FIG 1 is created, except that the peaks have not yet been inverted and are therefore absorption peaks. In principle, ions far detuned from the absorption peaks also contribute to the refractive index and has been neglected in Eq (2), but as shown in the supplementary, the effect of these can be neglected. The laser used has a linewidth of a few kHz and the homogeneous broadening of the ions in the crystal is on the order of kHz, hence the created spectral structure is fairly well represented by step functions, as seen in FIG 1. The absorption peaks consist of nine different ion classes, where each ion class refers to one of the nine transitions between the three ground states and three upper-states hyperfine levels. Since these transitions function as an effective two-level system for the inversion, they must be coherently excited using a single pulse. Furthermore, due to limited available laser power, the peaks must consist entirely of transitions with strong oscillator strength such that complete inversion can be achieved coherently well within the lifetime of the excited state. An optical transparency is first created by removing all ions in a frequency range, subsequently ions belonging to suitable ion classes are pumped back and collected by targeting specific frequency ranges. The excited state lifetime in the Eu-system is long, 2 ms. However, in a long strongly inverted medium, amplified spontaneous emission (ASE) will reduce the upper state lifetime. Spontaneous emission events at the beginning of the inverted region will be amplified as they travel along the inverted region and stimulate emission from the upper state. This effect scales exponentially with the magnitude of the gain. Hence there is a maximal allowable $\alpha L_{\text{max}}$, which can be estimated considering that the spontaneous emission that occurs at the very first slice of the crystal will have the dominant effect in reducing the lifetime. The details are given in the supplement and the result is,

$$\alpha L_{\text{max}} = \ln\left(\frac{\gamma_{\text{rad},21}}{W_{12}}\frac{z_{\text{R}}\lambda}{4n\pi L^2}\right) \tag{5}$$

Where $\gamma_{\text{rad},21}$ is the radiative decay on the $^5D_0 \rightarrow {}^7F_0$ transition used in the experiment, $z_{\text{R}}$, the Rayleigh length, $L$, the crystal length and $W_{12}$, the stimulated emission rate. In our case $z_{\text{R}} \approx L$ was required to ensure full inversion, and from simulations it followed that decreasing the lifetime by a factor of 2 was acceptable as this would leave enough time for first the inversion pulse and then the propagation pulse. This in essence gives a fundamental limit for the maximal gain and hence also the achievable dispersion in the material. In Eu:YSO, this limit is $\alpha L_{\text{max}} \approx 18$. In our experiments, we were, however, limited by the available Rabi frequency and thus could only invert gain structures with an $\alpha L_{\text{max}} \approx 2$. Thus, with an improved experimental setup it is possible to increase the time-bandwidth product even further.

Let us now, finally, turn to the topic of distortion. To have a distortion free pulse the bandwidth of a pulse, $\nu_{\text{FWHM}}$, must be smaller than the transmission window bandwidth, $\Gamma_{\text{hole}}$, and must remain below $\Gamma_{\text{hole}}$ by a factor that depends on the gain $\alpha L$. The reason for this

is that a pulse with a Gaussian envelope in time, will also have a Gaussian envelope in frequency. It will have frequency content in the wings which extends into the inverted region. This means that part of the Gaussian pulse, however small, will get selectively amplified, which may distort the pulse. However, the Gaussian envelops falls off fast enough that beyond a certain bandwidth, the gain structures causes practically no distortion, i.e., there is a level of tolerance when it comes to power leaking into the structure, before the pulse gets noticeably distorted, see FIG 2. This tolerance is connected to the magnitude of the gain of the structure, the frequency width of the optical window and the frequency width of the pulse. By multiplying the $\vec{E}$-field of the Gaussian in frequency space with the gain and comparing the area under the pulse to that of the unperturbed pulse, one can get a quick and intuitive picture whether the distortion will be significant. The error depends on the magnitude of the gain and the product of the $t_{\mathrm{FWHM}}$ and hole-width $\Gamma_{\mathrm{hole}}$:

$$\xi = (1 - e^{-\alpha L}) \left( \mathrm{erf} \left( \frac{\pi t_{\mathrm{FWHM}} \cdot \Gamma_{\mathrm{hole}}}{4\sqrt{\ln(2)}} \right) - 1 \right) \qquad (6)$$

$\xi$ is then used as a measure of how much the pulse is amplified or distorted, with the error function, erf() . Consequently there is a gain versus bandwidth trade-off, the largest time-bandwidth product is achieved at the highest $\alpha L$, but this structure will require higher Rabi frequency of the inversion pulse and reduce the tolerance for power in the structure. This tolerance can be seen in FIG 2 (a), where the increase in distortion due to the local amplification of the pulses', is plotted as a function of $\alpha L$ and the product of $\Gamma_h$ and $t_{\mathrm{FWHM}}$. In time, this results initially in amplification and at larger values a ringing trailing the pulse front, which we both refer to as distortion for simplicity.

To conclude, we first note that semi-permanent frequency-domain tailoring of absorption structures rare earth ion doped crystals have been extensively used in quantum computing [20], quantum memories [21–23], spectral filtering [24, 25]. More recently it has also been used for dispersion control to, e.g. enable dynamic speed of light control [26] or dynamic frequency shift control [27]. In this work it has been used for negative group velocity control, where a relative pulse advancement of $\frac{\Delta t}{t_{\mathrm{FWHM}}} = 13\%$ was obtained. This result surpasses previous negative group velocity work in terms of combined advancement and low pulse distortion. Further, simulations indicate that $\sim 30\%$ advancement should be achievable with this system and other approaches, e.g., a concatenated sequence of spectrally tailored crystals, may enable still more significant pulse advances. This work also supports the more general statement that rare earth doped crystals constitute excellent test beds for exploiting the possibilities of using strongly dispersive materials for light propagation applications.

[1] D. Strickland and G. Mourou, Optics Communications **55**, 447 (1985).
[2] L. Grüner-Nielsen, M. Wandel, P. Kristensen, C. Jørgensen, L. V. Jørgensen, B. Evold, B. Pálsdóttir, and D. Jakobsen, Journal of lightwave technology **23**, 3566 (2005).
[3] Y. Zhao, H.-W. Zhao, X.-Y. Zhang, B. Yuan, and S. Zhang, Optics & Laser Technology **41**, 517 (2009).
[4] S. Horvath, C. Shi, D. Gustavsson, A. Walther, A. Kinos, S. Kröll, and L. Rippe, New Journal of Physics **24**, 1 (2022).
[5] A.Bengtsson, D.Hill, M.Li, M.Di, M.Cinthio, T.Erlöv, S.Andersson-Engels, N.Reistad, A.Walter, L.Rippe, and S.Kröll, Biomedial Optics Express **10**, 5565 (2019).
[6] Z.Fang, H. Cai, G. chen, and R. Qu, Single frequency semiconductor lasers, in *Single Frequency Semiconductor Lasers*, Vol. 9, edited by A. Majumdar, A. Bjarklev, H. Caulfield, G. Marowsky, M. W. Sigrist, C. Someda, and M. Nakazawa (Springer, Singapore, 2017) pp. 168–169.
[7] N. Basov, R. Ambartsumyan, V. Zuev, P. Kryukov, and V. Letokhov, Soviet Physics JETP **23** (1966).
[8] S.Chu and S.Wong, Physical Review letters **48**, 738 (1982).
[9] B. Segard and B.Macke, Physics Letters **109A**, 213 (1985).
[10] R. Y. Chiao, Phys. Rev. A **48**, R34 (1993).
[11] A. M. Steinberg, P. G. Kwiat, and R. Y. Chiao, Phys. Rev. Lett. **71**, 708 (1993).
[12] R. P. Rajan, A. Redbane, and H. Riesen, Journal of the optical society of america B **32** (2015).
[13] Z.-Q. Zhou, C.-F. Li, and G.-C. Guo, Phys. Rev. A **87**, 045801 (2013).
[14] A. M. Steinberg and R. Y. Chiao, Physical Review A **49**, 2071 (1994).
[15] L.J.Wang, A.Kuzmich, and A.Dogariu, Nature **406**, 277 (2000).
[16] H. I. Ringenmacher and L. R. Mead, Comment on "Gain-Assisted Superluminal light Propagation" (2000).
[17] A. Dogariu, A. Kuzmich, and L. J. Wang, Phys. Rev. A **63**, 053806 (2001).
[18] B. Saleh and M. Teich, *Fundamentals of Photonics* (Wiley, 2019).
[19] A. E. Siegman, *Lasers*, 1st ed. (University Science Books, Mill Valley, CA, 1986).
[20] L. Rippe, M. Nilsson, S. Kröll, R. Klieber, and D. Suter, Phys. Rev. A **71**, 062328 (2005).
[21] M. Nilsson and S. Kröll, Optics Communications **247**, 393 (2005).
[22] M. Afzelius, C. Simon, H. de Riedmatten, and N. Gisin, Phys. Rev. A **79**, 052329 (2009).
[23] A. Safavi-Naeini, T. Alegre, and J. e. a. Chan, Nature **472**, 69 (2010).
[24] S. E. Beavan, E. A. Goldschmidt, and M. J. Sellars, J. Opt. Soc. Am. B **30**, 1173 (2013).
[25] A. Kinos, Q. Li, L. Rippe, and S. Kröll, Applied optics **55**, 10442 (2016).
[26] Q. Li, A. Kinos, A. Thuresson, L. Rippe, and S. Kröll, Phys. Rev. A **95**, 032104 (2017).
[27] Q. Li, Y. Bao, A. Thuresson, A. N. Nilsson, L. Rippe, and S. Kröll, Phys. Rev. A **93**, 043832 (2016).

[28] E. Z. Cruzeiro, J. Etesse, A. Tiranov, P.-A. Bourdel, F. Fröwis, P. Goldner, N. Gisin, and M. Afzelius, Phys. Rev. B **97**, 094416 (2018).
[29] J.-Y. Park and M. Garwood, Magn Reson Med. **61**, 175 (2009).
[30] F. Könz, Y. Sun, C. W. Thiel, R. L. Cone, R. W. Equall, R. L. Hutcheson, and R. M. Macfarlane, Phys. Rev. B **68**, 085109 (2003).
[31] F. R. Graf, A. Renn, G. Zumofen, and U. P. Wild, Phys. Rev. B **58**, 5462 (1998).
[32] B. Lauritzen, N. Timoney, N. Gisin, M. Afzelius, H. de Riedmatten, Y. Sun, R. M. Macfarlane, and R. L. Cone, Phys. Rev. B **85**, 115111 (2012).
[33] T. Kriváchy, K. T. Kaczmarek, M. Afzelius, J. Etesse, and G. Haack, Phys. Rev. A **107**, 013108 (2023).
[34] R. Yano, M. Mitsunaga, and N. Uesugi, Optics Letters **16** (1991).

## SUPPLEMENT

### Experimental setup

The experiments were conducted in a $Y_2SiO_5$ crystal with dimensions 14×15×21 mm doped to 1 at% natural abundance Europium containing both isotopes 151 and 153 in essentially equal proportion. The experiment was performed in the temperature range 2-4 K in a custom built closed cycle cryostat made by MyCryofirm.

The light pulses in this work were measured with a Hamamatsu S5973-02 photodiode and amplified by a femto - DHPCA-100 trans-impedance amplifier. Due to the low light power in the propagation pulses it was necessary to use high gain on the transimpedence amplifier. This limits the bandwidth of the detection to $f_{\mathrm{BW}} = 1.8$ MHz and rise time to, $t_{\mathrm{rise}=0.35/f_{\mathrm{BW}}} = 0.2\ \mu$s, which is significantly faster than the rise time of the pulse, which for a Gaussian is $t_{\mathrm{rise,\ Gaussian}} = 0.716\ t_{\mathrm{FWHM}} = 3.01$ MHz. From simulations we also know that this is sufficient bandwidth to detect any of the distortions could that arise from clipping the structure, should they occur (see FIG 2.c). The optical setup is schematically shown in FIG 3, the light path is as follows, the Gaussian pulse come out of the PM-fibre onto a beamsplitter that splits it into the reference path, where it is focused on an AOM that gates the propagation pulse (but blocks the inversion pulse) and then finally it is focused on the detector. The rest of the light goes through the crystal. It is first expanded, the polarisation is aligned with the appropriate crystal axis and filtered and then focused down into the crystal in the cryostat, which is at 2 K. After exiting the cryostat it is collimated and then gated by an AOM before it is focused on the detector through a polariser and a filter that removes the fluorescence of the crystal and otherwise scattered light (e.g. from reflections of optics and cryostat windows). Significant care was put into adjusting the AOM delay such that pulses arrived at the detectors at the same time when no structure was prepared.

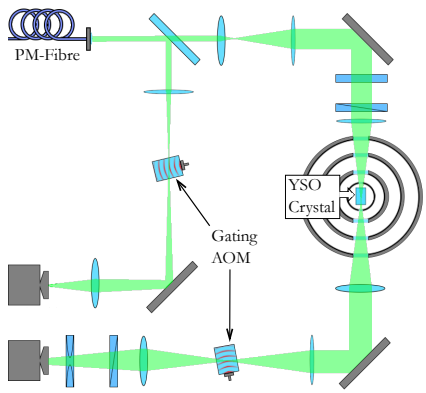


FIG. 3. Optical setup during the experiment.

### Preparation of structure

Experiments were performed on the $^7F_0 \rightarrow {}^5D_0$ transition. A six level simulator was used to keep track of the ions and determine the optimal frequencies for the optical pumping and for creating the absorption and transmission structures, such that the ions that make up the structure have their strong transition at these frequencies. Ion classes with a weak transition in these frequency ranges are not targeted for the burn back. A 29 MHz wide transmission widow was first created using optical pumping. Two absorbing structures each 1 MHz wide, centred at ± 650 kHz from the centre of the optical transmission window, leaving a 300 kHz transmission window at the centre frequency were created see FIG 4. The collected ions correspond to the transitions $|1/2g\rangle \rightarrow |5/2e\rangle$, $|3/2g\rangle \rightarrow |3/2e\rangle$ and $|5/2g\rangle \rightarrow |1/2e\rangle$, which have the strongest oscillator strengths and hence will be easier to invert [28]. If the ions with low oscillator strength would not be removed, these ions would absorb part of the energy from the inversion pulse, but would not reach inversion. This means that there would be an absorbing component in the structure causing the effective gain to be lower and as such the advancement would be reduced. The population inversion was then simulated using a Maxwell-Lindblad simulator, which used a simplified two level system where the oscillator strength were averaged corresponding to the fraction of the respective ions collected and using the estimated available laser power. The two gain regions are inverted using a "sechscan pulse", a frequency scan spliced in the middle of a sechhyp pulse [29]. A Gaussian pulse, $t_{\mathrm{FWHM}} = 4.2\ \mu$s,

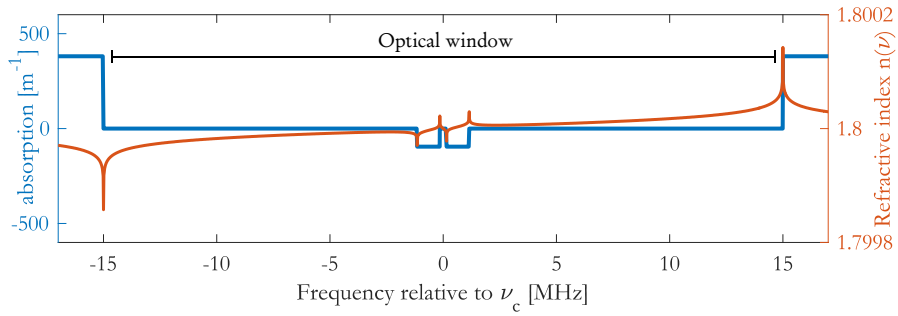


FIG. 4. Simulated Dispersion effect of the gain structure and optical window

was used as the propagation pulse. From the Maxwell-Lindblad simulations the parameters for the experiment were determined, as well as how the distortion would manifest itself, due to the pulse power in the gain structures exceeding the distortion free limit. This can be seen in FIG 2, where various magnitudes of $\alpha L$ are shown.

**Distortion**

To get a quick and intuitive idea of what will happen to the pulse for certain $t_{\mathrm{FWHM}}$ and $\Gamma_{\mathrm{hole}}$ with a given $\alpha L$ one can look at the pulse area in frequency space, after propagation through the gain structure. For this intuitive picture we do not consider the phase shift. This will give a clear representation of which frequency content is amplified and how large it is compared to the original envelope, see FIG 2. To derive a quantitative expression for the distortion, we start with the $E$-field of a Gaussian pulse in time,

$$E(t) = exp\left(-\frac{4\ln(2)t^2}{t_{\mathrm{FWHM}}^2}\right) \tag{7}$$

Which naturally remains Gaussian in frequency,

$$E(\nu) = \frac{t_{\mathrm{FWHM}}\sqrt{\pi}}{2\sqrt{ln(2)}} exp\left(-\frac{t_{\mathrm{FWHM}}^2\pi^2\nu^2}{4ln(2)}\right) \tag{8}$$

One can then write the expression for the gain structure as a function of frequency $\gamma(\nu)$. Since a Gaussian quickly drops off in amplitude, the effect of the gain structure will mostly come from the frequencies closest the pulse centre frequency, and the frequency content far in the wings will have little influence on the distortion. Thus the product of the amplification and the power in the wing of the pulse will be negligible already before the end of the proposed frequency width of the gain structure. This allows us to simplify the gain structure to be infinitely broad but with the transmission window around the centre frequency. Hence $\gamma(\nu)$:

$$\gamma(\nu) = exp\left(-\alpha L\left(\theta\left(-\frac{\Gamma_h}{2}+\nu\right)+\theta\left(-\frac{\Gamma_h}{2}-\nu\right)\right)\right) \tag{9}$$

Simply multiplying these and then integrating the product gives a measure of the energy in the pulse, then subtracting the original area leads to the amplified content:

$$\xi = \frac{\int_{-\infty}^{\infty} E(\nu)\gamma(\nu) - E(\nu)d\nu}{\int_{-\infty}^{\infty} E(\nu)d\nu} \tag{10}$$

Solving this lead to:

$$\xi = (1-e^{-\alpha L})\left(\mathrm{erf}\left(\frac{\pi t_{\mathrm{FWHM}}\cdot\Gamma_{\mathrm{hole}}}{4\sqrt{\ln(2)}}\right)-1\right)$$

**Derivation of $n(\nu)$**

The refractive index for the transmission window and the material combined is:

$$n(\nu) = n_{\mathrm{host}} + \frac{\chi_{\mathrm{real}}}{2n_{\mathrm{host}}} \tag{11}$$

[19, p. 377]

We start from the susceptibility:

$$\chi_h(\nu) = -\frac{2j\alpha_0 c n_{\mathrm{host}}}{\nu_{\mathrm{central}}\pi^2(\Gamma_h + 2j(\nu-\nu_0))} \tag{12}$$

Assume that the absorption profile looks flat from the perspective of the pit/structure and that there is no background absorption in the pit:

$$g(\nu) = \theta\left(-\frac{\Gamma_{\text{hole}}}{2} + \nu_0\right) + \theta\left(-\frac{\Gamma_{\text{hole}}}{2} - \nu_0\right) - \theta\left(-\Gamma_g - \nu_0\right) - \theta\left(-\Gamma_g + \nu_0\right) \quad (13)$$

Here $\theta(\nu)$ represents the Heaviside step-function. The real part of $\chi_h(\nu)$ describes the refractive index, the imaginary part the absorption. Then to get the $\Re(\chi_h(\nu))$ for the structure the integral of the susceptibility multiplied with the absorption profile must be computed:

$$\chi_{\text{real}} = \int_{\infty}^{\infty} g(\nu)\Re(\chi_h(\nu))d\nu_0 \quad (14)$$

Furthermore assume that the structure terminates at $\Gamma_g$ and that beyond this point the absorption is far enough away to not have a significant influence. One could consider these effects by simply adding similar terms with the appropriate boundary conditions, i.e. an optical window with width 29 MHz, but as can be seen from FIG 1, right inset, and FIG 4 it has little effect on the result. The simplified situation is described by:

$$\chi_{\text{real}} = \int_{-\Gamma_g}^{-\Gamma_{\text{hole}}/2} \Re(\chi_h(\nu))d\nu_0 + \int_{\Gamma_{\text{hole}}/2}^{\Gamma_g} \Re(\chi_h(\nu))d\nu_0 \quad (15)$$

Then computing this integral this gives:

$$\chi_{\text{real}} = -\frac{\alpha_0 c n_{\text{host}}}{2\pi^2\nu_{\text{central}}} \ln\left(\frac{4\Gamma_g^2 + 8\Gamma_g\nu + 4\nu^2 + \Gamma_h^2}{4\nu^2 + 4\Gamma_{\text{hole}}\nu + \Gamma_h^2 + \Gamma_{\text{hole}}^2}\right) + \ln\left(\frac{4\nu^2 - 4\Gamma_{\text{hole}}\nu + \Gamma_h^2 + \Gamma_{\text{hole}}^2}{4\Gamma_g^2 - 8\Gamma_g\nu + 4\nu^2 + \Gamma_h^2}\right) \quad (16)$$

The homogeneous linewidth $\Gamma_h$ (=250±50 Hz [30]), will be negligible compared to the other frequency widths so can be ignored giving:

$$\chi_{\text{real}} = -\frac{\alpha_0 c n_{\text{host}}}{2\pi^2\nu_{\text{central}}} \times \ln\left(\left(\frac{4\Gamma_g^2 + 8\Gamma_g\nu + 4\nu^2}{4\nu^2 + 4\Gamma_{\text{hole}}\nu + \Gamma_{\text{hole}}^2}\right)\left(\frac{4\nu^2 - 4\Gamma_{\text{hole}}\nu + \Gamma_{\text{hole}}^2}{4\Gamma_g^2 - 8\Gamma_g\nu + 4\nu^2}\right)\right) \quad (17)$$

using equation (11) and applying a Taylor expansion in $\nu$ around the centre of the optical window:

$$n(\nu) = n_{\text{host}} + \frac{\alpha_0 c}{\pi^2\nu_{\text{central}}}\left(\frac{1}{\Gamma_g} - \frac{2}{\Gamma_{\text{hole}}}\right)\nu \quad (18)$$

#### Un-normalised pulses and reference

In FIG 5 the pulse sequence from the experiment is shown. After the structure is prepared, we sent in an initial pulse without inversion, to probe the collected $\alpha L$ without disturbing the structure. Between probe pulses a 15 ms wait was added to allow proper relaxation. After which an inversion pulse is sent immediately followed by a probe pulse. Finally after another 15 ms wait, a third probe pulse is sent to assess the structure after absorption. This data is scaled according to best efforts to have equal power in both optical paths. As one can see from the vacuum pulse compared to the advanced pulse there is a slight amplification of the advanced pulse, and minor attenuation of the slowed down pulse. In the main part of the paper the reference pulses are normalised to the probe pulses to more clearly display the temporal shift.

#### Maximal gain

For these calculations we simplify the geometry, and assume the excited volume of the crystal to be roughly cylindrical. Then a spectral packet that originated at the very start of the crystal will reach the end with intensity:

$$I_{ij} \approx \frac{\gamma_{\text{rad,ij}} h\nu_{ij} r^2}{4\sigma_{ij} L^2} e^{-\alpha_{ij} L} \quad (19)$$

[19, p. 522], where the subscripts indicate the specific levels involved. With beam radius, $r$, cross section of transition $i \to j$, $\sigma_{ij}$ and crystal length, $L$. The total radiative decay rate from ${}^5D_0$ is $\gamma_{\text{rad,tot}} = \frac{1}{2\text{ms}} = 500$ Hz. The radiative decay for a specific transition is $\gamma_{\text{rad,ij}}$, $r$ the radius of the inverted cylinder, the absorption on a particular transition, $\alpha_{ij}$. Note that $\alpha_{ij} < 0$ when the population is inverted. Then using the relation of the stimulated transition rate and intensity one can find the relationship between the radiative decay rate and the transition rate. The stimulated emission rate $W_{ij}$ between a level $i$ and $j$ is given by:

$$W_{ij} = \frac{\sigma_{ij} I_{ij}}{h\nu} \quad (20)$$

combining these two equations leads to the ratio of the stimulated and radiative rates,

$$\frac{W_{ij}}{\gamma_{\text{rad},ij}} \approx \left(\frac{r}{2L}\right)^2 e^{-\alpha_{ij} L} \quad (21)$$

[19, p. 522]. The ${}^5D_0 \to {}^7F_0$, transition is used for this experiment, but there is also relaxation to the other ${}^7F_J$ levels, hence it is important to know what dominates the stimulated emission.

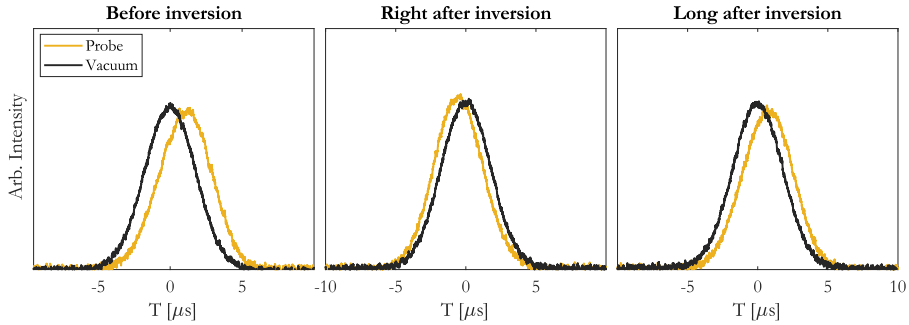


FIG. 5. Probe pulse sequence, where the vacuum-data is scaled according to best effort using simulations as if the intensities in both optical arms were the same. Here vacuum refers to the pulse that does not travel through the crystal but is picked off as shown in FIG 3

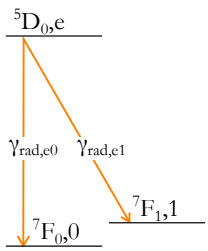


FIG. 6. Relevant levels for radiative decay. The $^5D_0$ is denoted by $e$, the $^7F_0$ by 0 and the $^7F_1$ by 1

From the radiative decay rate for this transition, the radiative decay rate for the $^5D_0 \rightarrow {}^7F_0$, $\gamma_{\text{rad, ceo}}$ transition can be calculated from its oscillator strength $F_{e0} = 1.3 \cdot 10^{-8}$ [31], as

$$\gamma_{\text{rad,e0}} = F_{e0} 3^* \gamma_{\text{rad, ceo}} \tag{22}$$

[19, p. 122], [30] $\gamma_{\text{rad,ceo}}$ is the radiative decay rate for the classical electron oscillator, [19, p. 122]

$$\gamma_{\text{rad,ceo}} = 2.47 \cdot 10^{-22} n \cdot \nu_{ij}^2 \tag{23}$$

with the refractive index $n = 1.8$, for $Y_2SiO_5$ [32]. The dimensionless polarisation overlap factor $3^*$ for site 1 in Eu:$^{3+}$Y$_2$SiO$_5$ with the light polarisation aligned with the D1 axis is given by:

$$3^* = \frac{3.9}{\sqrt{3.9^2 + .8^2}} * 3 = 2.94$$

The radiative decay rate can now be calculated, $\gamma_{\text{rad,e0}} = 4.23$ and the branching ratio for the $^5D_0 \rightarrow {}^7F_0$ transition is $\gamma_{\text{rad,e0}}/\gamma_{\text{rad,tot}} = 0.8\%$, which means that 99.2% from the $^5D_0$ relaxes through the $^7F_{J\in1,2,3,4,5,6}$ lines. The inverted structure on the $^5D_0 \rightarrow {}^7F_0$ transition is 2.3 MHz wide and since the $^5D_0 \rightarrow {}^7F_{j\in1,2,3,4,5,6}$ are much broader, the cross-section, $\sigma$ and the emission coefficient, $\alpha_{ij} = \Delta N_{ij}\sigma_{ij}$ for the stimulated emission will be scaled down with the ratio of the linewidth. The strongest emission from these transitions is on the $^5D_0 \rightarrow {}^7F_1$ see figure 3 in [30] It is also considerably narrower then the other transitions. Könz et al. report it to be much narrower than 6 GHz [30]. The cross-section for stimulated emission for the $^5D_0 \rightarrow {}^7F_1$, is $\sigma_{e0} = 1.2 \cdot 10^{-18}$ m$^2$ [33]. We will calculate what linewidth the $^5D_0 \rightarrow {}^7F_1$ would need to have in order to have the same cross-section as the $^5D_0 \rightarrow {}^7F_0$ transition. The cross-section $\sigma_{ij}$ is given by p288 in [19].

$$\sigma_{ij} = \frac{3^* \gamma_{\text{rad,ij}}}{\Delta\nu_{\text{Lorentzian}}} \left(\frac{\lambda_{ij}}{n}\right)^2 \tag{24}$$

If $\sigma_{e1}$ where to be equal to $\sigma_{e0}$ this would require a linewidth of,

$$\Delta\nu_{\text{Lorentzian}} = \frac{3^*}{\sigma_{e0}} \left(\frac{\lambda_{e1}}{n}\right)^2 \gamma_{\text{rad,e1}} \tag{25}$$

The radiative decay rate for the $^5D_0 \rightarrow {}^7F_1$ was estimated to be $\gamma_{\text{rad,el}} \approx 40$ from the relative line areas in figure 1b in [34], due to the limited resolution this was a rather crude estimate. The wavelength of the $^5D_0 \rightarrow {}^7F_1$ transition is $\lambda_{e1} = 586.882$ nm [30]. The required $^5D_0 \rightarrow {}^7F_1$ linewidth was then calculated from 24 using $3^* = 3$ as an upper bound which gives $\Delta\nu_{\text{Lorentzian}} = 10$ MHz Since it is very unlikely that the transition is this narrow one can assume that the stimulated ASE decay is completely dominated by the

${}^5D_0 \rightarrow {}^7F_0$. So we can simply take

$$\frac{W_{e0}}{\gamma_{\mathrm{rad,e0}}} \approx \left( \frac{\sqrt{\frac{z_\mathrm{R}\lambda_{e0}}{n\pi}}}{2L} \right)^2 \cdot e^{-\alpha_{e0}L} \tag{26}$$

Where $z_\mathrm{R}$ is the Raleigh range $\lambda_{e0}$ the wavelength, $W_{e0}$ the stimulated emission rate. Hence, given an acceptable reduction of the lifetime, given by the ratio $W_{e0}/\gamma_{\mathrm{rad,e0}}$, one can determine the maximum $\alpha L_{\max}$:

$$\alpha L_{\max} = \ln\left( \frac{\gamma_{\mathrm{rad,e0}}}{W_{e0}} \frac{z_\mathrm{R}\lambda}{4n\pi L^2} \right) \tag{27}$$

If we allow for a reduction of the upper lifetime to half, i.e. $\frac{w_{e0}}{\gamma_{\mathrm{rad,e0}}} = 1$ we get $\alpha L_{\max} \approx 18$ for our case. From either FIG 2 A or by plugging it in equations (4) and (6) given the error tolerance one can then see an advancement of $\approx 30\%$ can be obtained.